Stony Brook University

OFFICIAL COPY

The official electronic file of this thesis or dissertation is maintained by the University Libraries on behalf of The Graduate School at Stony Brook University.

© All Rights Reserved by Author.

Fabrication of Thermoelectric Devices Using Additive-Subtractive Manufacturing Techniques: Application to Waste-Heat Energy Harvesting

A Dissertation Presented

by

Mahder Tewolde

to

The Graduate School

in Partial Fulfillment of the

Requirements

for the Degree of

Doctor of Philosophy

in

Mechanical Engineering

Stony Brook University

December 2015

Stony Brook University

The Graduate School

Mahder Tewolde

We, the dissertation committee for the above candidate for the

Doctor of Philosophy degree, hereby recommend

acceptance of this dissertation.

Dr. Jon P. Longtin, Advisor
Professor, Mechanical Engineering

Dr. David Hwang, Chairperson of Defense
Assistant Professor, Mechanical Engineering

Dr. Sotirios Mamalis, Member
Assistant Professor, Mechanical Engineering

Dr. Sanjay Sampath, Outside Member
Professor, Materials Science and Engineering

This dissertation is accepted by the Graduate School

Charles Taber

Dean of the Graduate School

Abstract of the Dissertation

Fabrication of Thermoelectric Devices Using Additive-Subtractive Manufacturing Techniques: Application to Waste-Heat Energy Harvesting

by

Mahder Tewolde

Doctor of Philosophy

in

Mechanical Engineering

Stony Brook University

2015

Thermoelectric generators (TEGs) are solid-state devices that convert heat directly into electricity. They are well suited for waste-heat energy harvesting applications as opposed to primary energy generation. Commercially available thermoelectric modules are flat, inflexible and have limited sizes available. State-of-art manufacturing of TEG devices relies on assembling prefabricated parts with soldering, epoxy bonding, and mechanical clamping. Furthermore, efforts to incorporate them onto curved surfaces such as exhaust pipes, pump housings, steam lines, mixing containers, reaction chambers, etc. require custom-built heat exchangers. This is costly and labor-intensive, in addition to presenting challenges in terms of space, thermal coupling, added weight and long-term reliability. Additive manufacturing technologies are beginning to address many of these issues by reducing part count in complex designs and the elimination of sub-assembly requirements. This work investigates the feasibility of utilizing such novel manufacturing routes for improving the manufacturing process of thermoelectric devices.

Much of the research in thermoelectricity is primarily focused on improving thermoelectric material properties by developing of novel materials or finding ways to improve existing ones. Secondary to material development is improving the manufacturing process of TEGs to provide significant cost benefits. To improve the device fabrication process, this work explores additive manufacturing technologies to provide an integrated and scalable approach for TE device manufacturing directly onto engineering component surfaces. Additive manufacturing techniques like thermal spray and ink-dispenser printing are developed with the aim of improving the manufacturing process of TEGs. Subtractive manufacturing techniques like laser micromachining are also studied in detail. This includes the laser processing parameters for cutting the thermal spray materials efficiently by optimizing cutting speed and power while maintaining surface quality and interface properties. Key parameters are obtained from these experiments and used to develop a process that can be used to fabricate a working TEG *directly* onto the waste-heat component surface. A TEG module has been fabricated for the first time entirely by using thermal spray technology and laser micromachining. The target applications include automotive exhaust systems and other high-volume industrial waste heat sources. The application of TEGs for thermoelectrically powered sensors for Small Modular Reactors (SMRs) is presented. In conclusion, more ways to improve the fabrication process of TEGs are suggested.

Dedicated to my parents

Table of Contents

Table of Contents ... vi

List of Figures ... ix

List of Tables ... xiii

List of Abbreviations ... xiv

Acknowledgments ... xvi

Chapter 1 Introduction ... 1

1.1 Fabrication of Thermoelectric Devices ... 4

1.2 Additive Manufacturing Techniques for Thermoelectrics ... 6

1.3 Motivation for Present Work ... 13

1.4 New contributions from this work ... 17

1.5 Scope of Dissertation ... 19

Chapter 2 Theory and Application of Thermoelectric Devices ... 21

2.1 Thermoelectric Phenomena ... 21

2.2 Thermodynamics of Thermoelectric Phenomena ... 26

2.3 Thermoelectric Figure of Merit (*ZT*) ... 27

2.4 Thermoelectric Materials ... 30

2.5 Thermoelectric Device Configurations ... 34

2.6 Application of Thermoelectric Devices ... 40

2.7 Summary ... 42

Chapter 3 Application of Thermal Spray for Thermoelectric Device Fabrication ... 43

3.1 Materials for Thermals Spray ... 43
3.2 Fabrication of TE devices using Thermal Spray ... 47
3.3 Summary ... 56
Chapter 4 Subtractive Manufacturing Techniques for Thermoelectric Device Fabrication ... 57
4.1 SM Methods for Thermoelectrics ... 58
4.2 Laser Micromachining (LMM) ... 63
4.3 Thermal Modeling ... 72
4.4 Results and Discussion ... 77
4.5 Summary ... 91
Chapter 5 Additive-Subtractive Manufacturing of a Thermoelectric Generator ... 93
5.1 Thermal-Spray-Based Thermoelectric Device Fabrication ... 93
5.2 Results and Discussion ... 99
5.3 Summary ... 107
Chapter 6 Application of Ink-Dispenser Printing for Thermoelectric Devices ... 108
6.1 Materials for Ink-Dispenser Printing ... 109
6.2 Device Challenges of Ink-Dispenser Printing ... 112
6.3 Experimental Setup ... 113
6.4 Results and Discussion ... 117
6.5 Summary ... 129
Chapter 7 Waste-Heat Energy Harvesting Applications for TEGs ... 130
7.1 Overview ... 130
7.2 TEG-based Sensors for Small Modular Reactors ... 131
7.3 Characterization of Commercial TEGs ... 138
7.4 Design and Fabrication of TEG-based Sensor Prototype ... 144

7.5 Results and Discussion 146

7.6 Summary 151

Chapter 8 Conclusions, Enabled Research Topics, and Future Directions 152

Bibliography 157

Appendix A Thermoelectric Material Testing and Characterization Tools 169

A.1 Seebeck Coefficient 169

A.2 Thermal Properties 171

A.3 Electrical Properties 172

List of Figures

Fig. 1-1 Estimated U.S. Energy Use in 2013 [5] 3

Fig. 1-2 Commercial thermoelectric modules and devices 4

Fig. 1-3 Steps for conventional fabrication for TE devices 5

Fig. 1-4 Thermal resistive networks model used for design and analysis of TEG system 16

Fig. 1-5 Overview of current and future research 18

Fig. 2-1 Thermoelectric circuit composed of two different materials A and B 22

Fig. 2-2 Commercial thermocouple (left) and thermoelectric legs (right) 23

Fig. 2-3 Schematic for the Peltier effect and Thomson effect 25

Fig. 2-4 Trade-off between electrical conductivity (σ), Seebeck coefficient (S), and thermal conductivity (κ) that involves increasing the number of free carriers from insulators to metals [65] 29

Fig. 2-5 Figure of merit (*ZT*) as a function of temperature for several bulk thermoelectric materials [1]........ 33

Fig. 2-6 Common design architectures of TE devices (vertical and planar designs)........ 35

Fig. 2-7 Schematic of a typical π-type single-stage thermoelectric device 35

Fig. 2-8 Heat transfer within a thermoelectric generator 37

Fig. 2-9 The efficiency of TEGs with the corresponding ZT and comparison of thermoelectric power generation efficiency with conventional engines [65] 40

Fig. 3-1 General apparatus for thermal spray [85] 44

Fig. 3-2 SEM image showing detail of microstructural features[86]........ 45

Fig. 3-3 Process steps to fabricate a TEG module (a) exhaust component with integrated heat sink (b) apply bottom electrode and pattern, (c) deposit of n and p type TE legs, (d) fill the gap and deposit top electrode and top insulating layer........ 48

Fig. 3-4 Stress developed due to non-uniform cooling of thermal spray layer........ 49

Fig. 3-5 (a) copper sprayed on alumina wafer (b) copper and alumina sprayed on aluminum wafer 50

Fig. 3-6 Coatings resulting from (a) contact masks (b) versus shadow masks [34]........ 51

Fig. 3-7 Mask fabricated from Al to test various offset distances 52

Fig. 3-8 Demonstration of high aspect ratio spraying of TE legs 53

Fig. 3-9 Leg thickness and leg width of sprayed legs vs. offset distance 53

Fig. 3-10 Proposed gap filling procedure (left) Air gap filled with sand/glue mixture and allowed to dry, (center) top conducting layer sprayed after mixture dries, (right) sample baked at elevated temperature to remove filler, leaving air gap 54

Fig. 3-11 (left) Al block with machined grooves filled with PVA/sand mixture to demonstrate gap filling (right) Sample after deposition of 0.7-mm NiCr and bake-out of filler material at 400 °C 56

Fig. 4-1 Classification of Subtractive Machining Techniques 58

Fig. 4-2 Laser patterning of copper 63

Fig. 4-3 Laser irradiance and interaction time for material processing applications [98] 65

Fig. 4-4 Typical laser machining setup 67

Fig. 4-5 Laser pulses from GM-30 Laser 74

Fig. 4-6 Intensity profile of GM-30 laser beam 75

Fig. 4-7 Graph of D^2 vs. $\ln(E_p)$ for FW-150 and FW-40 lasers on copper with holes ablated with 100 and 1000 pulses. 79

Fig. 4-8 Crater diameter versus laser fluence to evaluate ablation threshold for FW-40 laser. Numbers (100, 1000) indicate the number of pulses used to ablate a crater. 80

Fig. 4-9 Crater diameter versus laser fluence to evaluate ablation threshold for FW-150 laser. Numbers (100 and 1000) indicate the number of pulses used to ablate a crater. 80

Fig. 4-10 Crater diameter versus laser fluence to evaluate ablation threshold for GM-30 laser. Numbers (10, 100 and 1000) indicate the number of pulses used to ablate a crater. 81

Fig. 4-11 Ablation rate of the copper as a function of laser pulse energy for (a) FW-40 laser, (b) FW-150 laser and (c) GM-30 laser 83

Fig. 4-12 Material removal rate of the copper as a function of laser power 83

Fig. 4-13 Ablation efficiency of copper as a function of laser power 84

Fig. 4-14 Material removal rate of copper as a function of laser power for GM-30 laser 85

Fig. 4-15 Single line patterning of copper with GM-30 laser 86

Fig. 4-16 Machining parameters for extended machining 88

Fig. 4-17 Multiple line cutting of copper sample with GM-30 laser 88

Fig. 4-18 Surface temperature distribution for a single-pulse on copper substrate 90

Fig. 4-19 Temperature distribution at different times 90

Fig. 5-1 Module design and configuration 96

Fig. 5-2 Process steps to fabricate a TEG module (a) metal substrate, (b) apply bottom electrode and pattern, (c) deposit *n*- and *p*-type TE legs, (d) deposit top electrode layer 97

Fig. 5-3 Results from APS spraying of bottom electrode layer on flat substrate 100

Fig. 5-4 Patterned bottom copper electrode on a flat substrate 101

Fig. 5-5 Thermal Spray of *p*-type and *n*-type legs on flat coupon & masks used 101

Fig. 5-6 (a) Temporary filler material applied to the legs and (b) blanket coating of copper sprayed and (c) final device after micromachining top layer 103

Fig. 5-7 (a) Test stand to characterize TEG and (b) measurement of topside temperature with an infrared camera 104

Fig. 5-8 Thermal resistor model of TE pair 105

Fig. 5-9 Open-circuit voltage measured as function of temperature difference across the TE legs (ΔT_{TE}) 106

Fig. 6-1 Copper powders dispersed in polymer matrix 110

Fig. 6-2 Schematic representation of (a) droplet-based and (b) line-based printing strategies 113

Fig. 6-3 Dispenser system setup 116

Fig. 6-4 TGA of epoxy resin. 118

Fig. 6-5 TGA of p-type as received Bi_2Te_3 powder. 118

Fig. 6-6 TGA of n-type as received Bi2Te3 powder. 119

Fig. 6-7 DSC curves of epoxy resin 119

Fig. 6-8 DSC curves of epoxy resin 120

Fig. 6-9 X-ray powder diffractions (XRD) of the as-received thermoelectric powders. 120

Fig. 6-10 Temperature dependence of through-thickness thermal conductivity measurements of n-type (left) and p-type (right) Bi_2Te_3 sintered at various temperatures. 121

Fig. 6-11 Temperature dependence of Seebeck coefficient of n-type (left) and p-type (right) Bi_2Te_3 sintered at various temperatures. 122

Fig. 6-12 Temperature dependence of electrical conductivity of n-type (left) and p-type (right) Bi_2Te_3 sintered at various temperatures. 123

Fig. 6-13 Power factor and ZT of printed *n*-type (left) and *p*-type (right) Bi_2Te_3 sintered at various temperatures. 123

Fig. 6-14 SEM image of printed n-type Bi_2Te_3 cured at 350°C 124

Fig. 6-15 Temperature dependence of in-plane thermal conductivity of *n*-type (left) and *p*-type (right) Bi_2Te_3 with 0.1% and 0.2% Ag nanoparticles sintered at 350 °C. 125

Fig. 6-16 Temperature dependence electrical conductivity of *n*-type (left) and *p*-type (right) Bi_2Te_3 with 0.1% and 0.2% Ag nanoparticles sintered at 350 °C. 125

Fig. 6-17 Seebeck coefficient of *n*-type (left) and *p*-type (right) Bi_2Te_3 with 0.1% and 0.2% Ag nanoparticles sintered at 350 °C. 125

Fig. 6-18 SEM image of printed *n*-type Bi_2Te_3 with 0.2% Ag cured at 350°C 126

Fig. 6-19 Printed droplet width as a function of dispensing pressure 127
Fig. 6-20 Printed line thickness as a function of dispensing pressure for 27 gauge needle . 127
Fig. 6-21 Printed line thickness as a function of dispensing pressure for 25 gauge needle . 128
Fig. 6-22 Dispenser printing of features using line based printing strategy 128
Fig. 7-1 TEG based sensing and actuation during normal and off-normal conditions 134
Fig. 7-2 Commercial HZ-2 Module 140
Fig. 7-3 TEG test stand configuration 141
Fig. 7-4 Top copper surface thermal image 141
Fig. 7-5 Illustration of the effect of thermal flexible graphite sheet inserted at the boundary between the heat source and TE modules and heatsink. 142
Fig. 7-6 Measurement setup of temperature and heat flux (left) and RTD probes for water inlet and outlets (right) 143
Fig. 7-7 DAQ system for TEG test stand 143
Fig. 7-8 A cross section of prototype of TEG-based sensor package attached to a hot pipe . 145
Fig. 7-9 Open Circuit Voltage vs. temperature difference for HZ-2 module 146
Fig. 7-10 HZ-2 Characteristic Curve 147
Fig. 7-11 Thermal analysis of designed prototype and temperatures at key locations 148
Fig. 7-12 (a) Lab test setup without insulation layer (b) and insulation layer (c) mounted TEGs (d) TEG mounting arrangement (e) mounting 149
Fig. 7-13 Entire design installed on the steam pipe 150
Fig. 7-14 Temperature data collected from TEG sensor for a 20-hour period 150
Fig. 8-1 Additive & Subtractive TEG Manufacturing using Thermal Spray (Additive) and Laser Machining (Subtractive) 155

List of Tables

Table 1-1 Evaluation of AM techniques for thermoelectric devices 12

Table 1-2 Examples of thermoelectric devices fabricated by ink printing 15

Table 2-1 Seebeck coefficients for selected materials at 300 K [4, 57] 23

Table 2-2 Comparison of thermoelectric properties of metals, semiconductors and insulators at 300 K [67] 30

Table 2-3 Summary of current thermoelectric materials [4, 66, 75] 33

Table 3-1 Thermal conductivities [W/m·K] of thermal sprayed materials [86-88] 46

Table 4-1 Comparison of SM Methods Available for Thermoelectric Devices 62

Table 4-2 Choice of available lasers 65

Table 4-3 Thermal and optical properties of copper (300K) [111, 112] 76

Table 4-4 Ablation threshold of copper with different laser system 81

Table 4-5 Laser thermal optical penetration depth of copper for available lasers 85

Table 4-6 Optimum Laser Cutting Parameters 87

Table 5-1 Transport Properties of Materials Used [122-124] 96

Table 5-2 Optimal Laser Cutting Parameters 100

Table 5-3 Laser Cutting Parameters for Top Coating 103

Table 5-4 Thermal resistances of various elements across the TEG 105

Table 6-1 As-Received thermoelectric properties for bulk Bi_2TE_3 powders 114

Table 7-1 Core and steam generator inlet/outlet temperature in SMRs [146] 135

Table 7-2 Temperature ranges and different usable materials[150] 138

Table 7-3 Comparison of Similar TEGs from different Manufacturers 139

List of Abbreviations

Symbol	Units	Description
Upper Case Roman		
A	m^2	heat transfer or laser beam area
C_p	J/K	heat capacity at constant pressure
C_v	J/K	heat capacity at constant volume
Cu		Copper
F	J/m^2	laser fluence
G	S	conductance
I	A	electric current
I	W/m^2	laser intensity
L	$W \cdot \Omega/K^2$	lorenz ratio, k_e/T
P	W	laser power or electrical power
Q	J	heat transported
$\dot{Q}_\pi$	W	Peltier heat
$\dot{Q}_\mu$	W	Thomson heat
R	Ω	resistance
S	J/K	entropy
S	V/K	Seebeck Coefficient
U	J	internal energy
T_C	K	cold side temperature (K)
T_H	K	hot side temperature (K)
ZT	–	thermoelectric material figure merit
$\overline{ZT}$	–	thermoelectric device figure merit
V	V	voltage
W	J	mechanical or work done electrical
Acronym		
APS	–	atmospheric plasma spray thermal spray technique
COP		coefficient of performance
CW	–	continuous wave
DOS		density of states
HVOF	–	high-velocity oxy-fuel thermal spray technique
PPR	*Hz*	pulse repetition rate
SEM	–	scanning electron microscope
VPS	–	vacuum plasma spray

YSZ	–	yttra-stabilized zirconia

Lower Case Roman

e	C	electronic charge
f	m	focal length
c_p	J/kg·K	specific heat capacity at constant pressure
c_v	J/kg·K	specific heat capacity at constant volume
k_g	W/m·K	lattice thermal conductivity
k_e	W/m·K	electronic thermal conductivity
m	–	the ratio of load resistance to device resistance
n	–	refractive index
τ_p	s	laser pulse duration, s
t	s	time
r	Ω	internal resistance
w_0	m	laser beam waist
x	m	horizontal direction
y	m	vertical direction
z	m	axial directions

Greek

Σ	–	Sum
ΔT	K	temperature difference
λ	nm	laser wavelength
α	V/K	Seebeck Coefficient
σ	S/m	electrical conductivity
κ	W/mK	thermal conductivity
α	m^{-1}	linear absorption coefficient
π	W/A	Peltier coefficient
μ	V/K	Thomson coefficient
χ	m/m·°C	thermal expansion coefficient
τ_p	S	laser pulse width, (FWHM)
ω	m	laser beam radius

Acknowledgments

First, and foremost, I thank Professor Jon Longtin for his guidance and support. His direction, advice, and knowledge are unparalleled, and I am honored to have worked under him. Advice from him extended beyond the experimental and technical realm. His emphasis on communication skills, both written and oral are invaluable. The financial support during my tenure with him is most gratefully acknowledged.

I would like to thank Professor David Hwang for his time and valuable comments drawn from his vast research experience to enhance this dissertation. I am grateful for the opportunity to perform experiments in his lab. I have learned a great deal about thermal sciences, lasers, and optics from my many discussions with him.

I would like to thank Professor Sanjay Sampath in the Department of Material Science and Engineering for providing the facility to do my experimental work and his guidance on several aspects of the thermal spray process.

I thank Professor Sotiris Mamalis for reading my dissertation and providing valuable guidance during my time as an instructor for a graduate course.

It has been a rewarding experience to work with other colleagues in Professor Longtin's research group, both past and present. I would like to thank He Tao, Hanfei Chen, Gaosheng Fu, Yikai Chen, Tao Zhang and several others for their assistance and contribution.

Finally, I would like to thank my parents and siblings for their love and support.

Chapter 1

Introduction

Thermoelectric generators (TEGs) are solid-state devices that can convert heat into electricity. The operating principles of thermoelectric power generation and heating/cooling applications are the Seebeck effect and the Peltier effect, respectively. The thermoelectric figure of merit (ZT) is a dimensionless parameter that describes how well a thermoelectric material can convert heat into electricity at a given absolute temperature. High ZT materials can provide higher conversion efficiencies. The vast majority of research in thermoelectric energy conversion efficiency is focused towards improving material performance rather than exploring ways to reduce manufacturing costs. This research focus is on developing novel, high-performance materials or improving existing ones. In addition, improvements in the manufacturing process of TEGs and reducing costs can provide significant benefits to the field of thermoelectricity. Current state-of-art thermoelectric technologies, which are based on prefabricated parts and assemblies, rely on soldering, epoxy bonding, and mechanical clamping. Emerging additive and subtractive manufacturing technologies are well suited to overcome these challenges by eliminating the need for sub-assembly requirements and allowing for an integrated fabrication process. Therefore, exploring novel manufacturing routes that utilize newly emerging fabrication technologies is an important part of this research. In this work, new manufacturing approaches including thermal spray, ink-dispenser

printing, and laser micromachining are investigated to develop an integrated and scalable approach for TEG manufacturing.

There has been considerable interest in the field of thermoelectricity in recent years, following advancements that led to the production of high-efficiency thermoelectric (TE) materials. This interest has led to marked improvements in thermoelectric device efficiency and cost. As a result, they have found widespread applications in numerous areas such as military, medical, industrial, consumer, scientific/laboratory, telecommunication and waste-heat recovery from vehicle exhaust and distributed power generation [1]. The global market for thermoelectric generators is currently small, valued at $245.3 million in 2014, and is projected to grow to $547.7 million by the year 2020. [2] The world energy consumption is projected to grow by 56% between 2010 and 2040, from 524 quads[1] to 820 quads [3]. As the demand for electricity grows, finding alternative sources of electricity that are cheaper and cleaner is essential. Technologies that can harvest energy from the ambient environment can play a huge role in meeting this increasing demand. There is considerable potential for generating electrical power from waste heat sources. This low-quality, low-cost source of energy is ubiquitous in industrial, commercial and residential settings. In the year 2013, ~9.74 quads of energy was produced in the U.S., of which 59% was rejected to the environment as waste heat due to the second law of thermodynamics and energy conversion inefficiencies in power generation systems (Fig. 1-1). Even recovering a small percentage of this

[1] A quad is a unit of energy equivalent to 10^{15} BTU or 1.055×10^{18} J

energy can have enormous benefits. Thus, the development of cost-effective technologies that can generate electricity from waste heat is essential.

The efficiency of thermoelectric generators is low (4-10%)[4] compared to conventional power generation technologies and are, therefore, not suitable for primary power generation. Their efficiency needs to be improved if they are to be broadly implemented beyond a few niche markets, and be competitive with current energy conversion technology on a large scale. However, they are ideal for waste-heat energy harvesting applications. TEGs offer several advantages: they are simple, compact and safe; they are extremely reliable and flexible power sources; they have no moving parts requiring reduced or no maintenance; they are suited for small-scale and remote applications; they are environmentally friendly and have a wide range of applications without significant a reduction in performance.

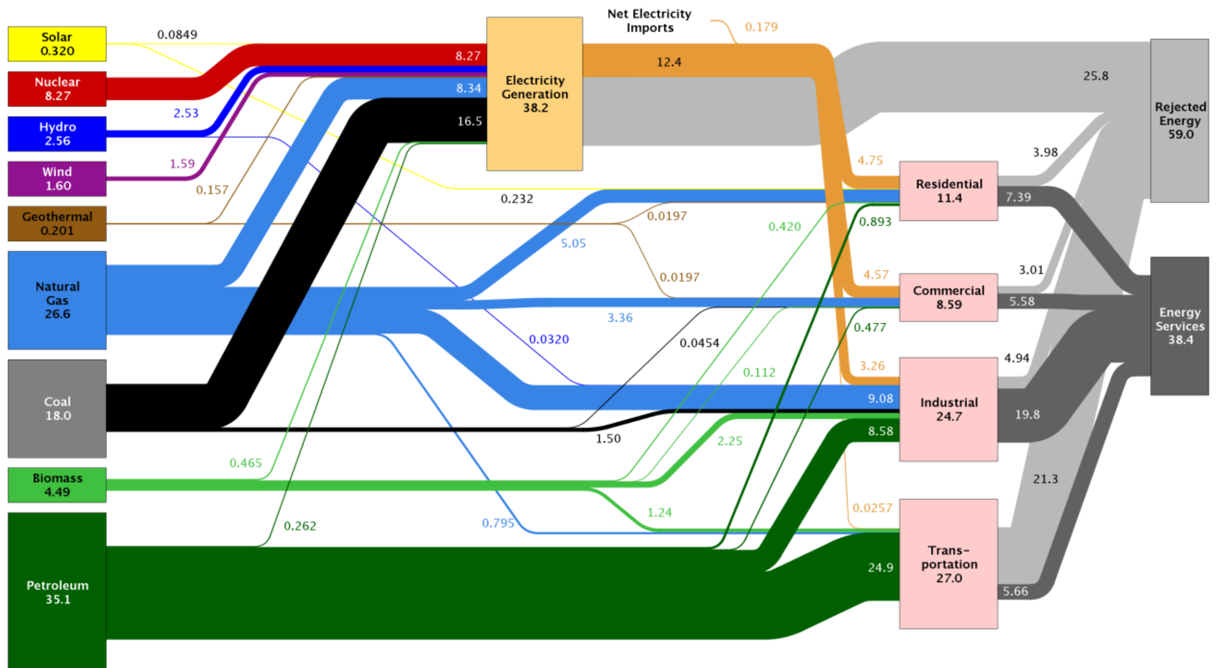

Fig. 1-1 Estimated U.S. Energy Use in 2013 [5]

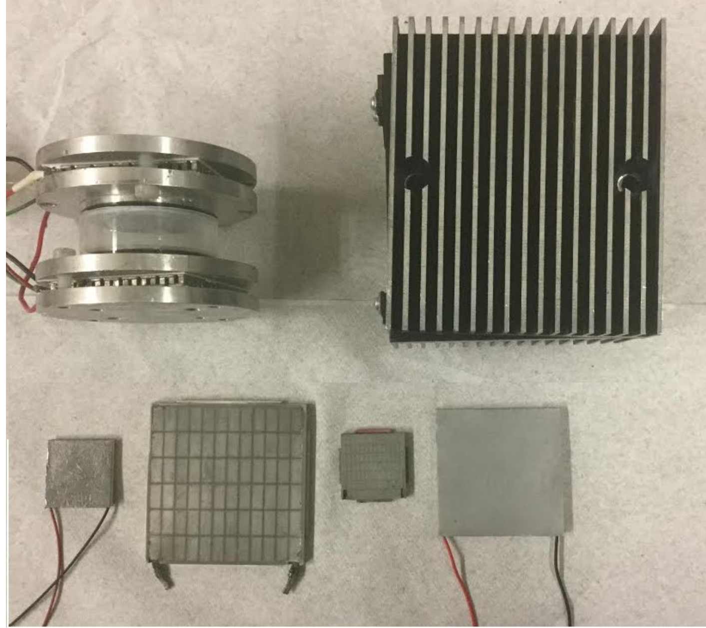

Fig. 1-2 Commercial thermoelectric modules and devices

1.1 Fabrication of Thermoelectric Devices

The manufacturing process for thermoelectric devices varies based on the type of thermoelectric material employed [6]. A large share of the cost of manufacturing TEG modules is in the material preparation and module assembly. Production methods for TE materials include powder or crystal growth based techniques. An overview of the current state-of-the-art manufacturing process for TE modules is shown in Fig. 1-3. Thermoelectric material synthesis begins with high-energy milling, mechanical alloying or melting of stoichiometric ratios of the constituent elements until a specific composition is achieved. Mechanical alloying is a powder processing technique that allows the production of homogeneous materials starting from blended elemental powder mixtures. Powder-based techniques offer an excellent ability to control and maintain desired carrier distributions. In powder techniques, either different powders are mixed with a varying ratio before melting, or they are in different layers as a stack before pressing and melting. In crystal growth techniques, dopants are often mixed with the melt, but diffusion from the gaseous phase can also

be used. In the zone melting techniques, disks of different materials are stacked on top of another and then materials are mixed with each other when a traveling heater causes melting. Melt spinning is a technique that is used for the rapid cooling of liquids. A cooled wheel is rotated while a thin stream of liquid is then dripped onto it causing rapid solidification. This technique is used to develop materials that require extremely high cooling rates to form, such as metallic glasses. The cooling rates achievable by melt spinning are approximately 10^4–10^7 kelvins per second (K/s).

Once the TE material is synthesized in powder or particle form, it is consolidated into ingots, either through hot pressing (HP), hot isostatic pressing (HIP) or one of the many sintering techniques available such as spark plasma sintering (SPS). Thermoelectric properties may be further optimized with post-sintering heat treatment of the materials. The ingots are then diced, polished and cut to form the TE legs as required. The legs and metallic interconnects are assembled into a module using soldering, epoxy bonding, or mechanical pressing [7, 8]. Some challenges present during assembly include material brittleness causing micro-cracks that can degrade performance. It should also be noted that conventional techniques used in the fabrication of macro thermoelectric devices are not suited for micro devices. This is because there are a few patterning techniques for the fabrication of features that are sized below tens of micrometers.

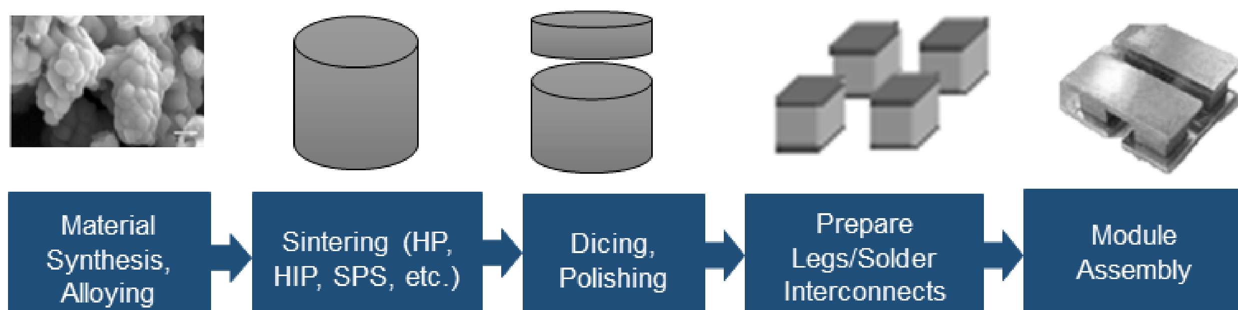

Fig. 1-3 Steps for conventional fabrication for TE devices

1.2 Additive Manufacturing Techniques for Thermoelectrics

The term additive manufacturing (AM) can refer to one of several technologies that include automated fabrication, solid free-form fabrication, 3D printing, layer-based manufacturing or rapid prototyping [9]. AM techniques are different from subtractive manufacturing methods in which parts are fabricated by removing material. In this work, AM is used to describe any fabrication processes that are based on adding material in layers, in contrast to removing materials. These include methods that direct-write (DW) materials in layers. DW technologies can create two- or three-dimensional functional structures directly onto flat or conformal surfaces in complex shapes, without any tooling or masks [10]. These include vapor-transfer spraying and ink-based dispensing methods. Methods that build-up includes selective laser sintering and fused model deposition. AM methods are becoming increasingly important for industrial uses. AM technologies are not limited in the complexity of the parts they can create in a limited timeframe. They can produce far superior results for parts with complex geometries or intricate designs than subtractive methods can. There are different types of AM techniques that are used for the fabrication of thermoelectric materials and devices. Each has their respective advantages and disadvantages regarding manufacturing speed, cost, throughput, and ease of fabrication. For TEGs, the material performance and leg thickness are important parameters.

1.2.1 Physical Vapor Deposition (PVD)

The term PVD describes a variety of vacuum vapor-transfer methods used to deposit thin films by the condensation of a vapor form of the desired film material onto various substrates. There are several types of PVD techniques including *evaporative deposition*, *pulsed laser deposition,* and *sputter deposition*.

Evaporative deposition is a common microfabrication method that has been used to fabricate thermoelectric materials and devices. For example, Bismuth and Tellurium can be co-evaporated at controlled rates to obtain stoichiometric Bi_2Te_3. Co-evaporation offers several advantages in the growth of thin film TEs such as the desirable stoichiometry, simple evaporation equipment, and a relatively short fabrication processing time [11]. Takashiri *et.al* reported high-performance $Bi_{0.4}Te_{3.0}Sb_{1.6}$ thin films with a thermoelectric power factor of 12.2 W/cm·K [12] and thermoelectric generators with the flash evaporation method [13]. Yamamoto *et.al* reported on the in-plane thermoelectric modules fabricated using evaporative deposition and shadow masking techniques [14].

Pulsed laser deposition (PLD) is a method where a high-power laser ablates material from the target into vapor form for deposition. PLD offers flexibility for enhanced TE properties of films by enabling the microstructure and compositions of films to be manipulated extensively with substrate temperatures and ambient pressures. PLD has been used extensively to fabricate bismuth-telluride thin films [15] [16]. Sputtering uses gaseous plasma to accelerate ions from plasma to a target. High-performance thermoelectric materials can be fabricated by sputtering two or more elements (co-sputtering) onto a substrate. Böttner *et.al* reported on a bismuth telluride based TE device using co-sputtered deposition [17] among others [18].

1.2.2 Chemical Vapor Deposition (CVD)

CVD is a vapor-transfer process which involves the deposition of a thin film on a heated substrate by flowing a precursor gas or gasses into a chamber resulting in chemical reactions taking place near the hot surface and condensing into a film on the surface [19]. Depending on the heat source

used to initiate the chemical reaction, the process can be further classified into thermal, laser, focused ion beam or electron beam. CVD is used to produce most metals, non-metallic elements such as carbon, nitride, oxides, intermetallics and other high-quality materials. CVD finds extensive use in the semiconductor industry and has an extensive literature, including a number of books on the subject [20, 21].

The deposition of thermoelectric films reported in the literature uses metal-organic chemical vapor deposition (MOCVD) (which is based on metal organic precursors) to prepare several types of high-quality thin film thermoelectric materials including *n*-BP, Bi_2Te_3 and Se_2Te_3 [22-26]. However, the thickness of the films prepared was limited to <100 nm and had very slow deposition rates. It is also expensive and requires complicated equipment with specific gasses for the deposition. CVD can be used to deposit conformal films since it is not restricted to a line-of-sight deposition but has low deposition rates in general. CVD films can be etched using lithographic or etching techniques.

1.2.3 Electrochemical Deposition (ECD)

Electrochemical deposition (electrodeposition or electroplating) is a process by which a material (metal, oxide, or salt) is coated on a surface of a *conductor substrate* by simple electrolysis of a solution containing the desired metal ion or its chemical complex. It has applications for protective or decorative coating of surfaces and can form thin and tightly adherent coatings. ECD has been investigated for TE device fabrication because of its cost-effectiveness, rapid deposition rates, and relative ease in controlling film thickness from the nanoscale to a few millimeters. Depending on the current density used in deposition, the deposition rate can be varied widely, up to several tens of microns per hour [27]. It has been used to coat thin films by different types of thermoelectric

materials including Bi_2Te_3, Sb_2Te_3, PbTe and $CoSb_3$ [27-33]. In most of this work, the thickness of the electrodeposited thermoelectric films reported has been lower than 10 μm. However, the thermoelectric properties of the deposited films after annealing were comparable to the bulk values. ECD films can be patterned using lithographic techniques.

1.2.4 Thermal Spray

Thermal spray is a process that accelerates material to high velocities and deposits them on a substrate. The material is introduced into a combustion or plasma flame (plume) in powder or wire form. The plume melts and imparts thermal and kinetic energy to the material, creating high-velocity droplets [34]. The particles (10-100 μm in size) are fed into a high-enthalpy jet, which simultaneously melts and accelerates the particles towards the surface of the component to be sprayed. By controlling the plume characteristic and material state (e.g., molten or softened), it is possible to deposit a wide range of metals, ceramics, polymers, or composites. Thermal spray finds application in many industrial fields, from the aeronautical and terrestrial turbines (e.g. thermal barrier coatings, abradable seals, etc.) to the biomedical industry (e.g. bio-integrable coatings onto orthoprotheses), the paper industry (e.g. abrasion wear resistant and corrosion-resistant coatings), etc., among others [35]. Particles can be deposited in a solid or semisolid state, which enables the creation of useful deposits at or near room temperature. The heat source can be a combustion flame, plasma jet, or an arc struck between two consumable wires.

The use of thermal spray to find the optimized thermal spray parameters as an alternative means of fabricating high-quality thermoelectric materials include Mg_2Si [36, 37], $FeSi_2$ [38] and Si-Ge[39]. These studies were not able to achieve high *ZT* values, but research in this area is ongoing

and is expected to improve *ZT* values comparable to, if not more than traditional fabrication methods such as HP or SPS. The use of thermal spray for the fabrication of TE devices has not been attempted before. Another variation of thermal spray is cold spraying where the materials being sprayed remain below the melting temperature and the bonding energy for the splats comes from the kinetic energy of the particles to obtain a high density, low porosity coating which is machinable [40]. Cold spraying benefits the fabrication of thermoelectric materials because of minimal thermal exposure.

1.2.5 Ink-Based Processes

Liquid inks represent the simplest, most varied and least expensive approach to AM. These inks contain the basic materials that become part of the desired structure. The inks are deposited onto a surface through screen-printing or dispenser printing. A significant number of ink types are available including colloidal inks, nanoparticle-filled inks, fugitive organic inks, polyelectrolyte inks, and sol–gel inks. After deposition, these inks solidify due to evaporation, gelation, solvent-driven reactions, or radiative curing to leave a deposit of the desired properties. Numerous researchers have focused on the development of new and improved inks and dispensing parameters.

Screen-printing is a technique that uses a pre-shaped screen with open areas that transfer ink or other printable materials onto a substrate. The paste can then be pressed through the mesh as a sharp-edged image onto a substrate. Screen-printing has several important advantages for mass production, such as a simple process sequence, short process time, low fabrication cost, low equipment cost, and a large temperature difference across the thick film. Several researchers have demonstrated the use of screen printing for fabricating thermoelectric materials, including Kim *et*

al. on thick-film of Sb_2Te_3 fabricated by a screen-printing technique [41], Lee *et al.* on screen-printed ZnSb films and modules [42, 43], Bi_2Te_3 [44-47] and metals [48].

Dispenser printing is a process in which a liquid or gel-based ink is deposited with a syringe, pen, or by inkjet printing. The solvents in the ink can be dried naturally or cured with radiation leaving solid material behind. Nozzle dispensed processes are technologies which use a mechanical or pneumatic syringe mechanism to push inks through an orifice for deposition onto a substrate. Several research studies have demonstrated the fabrication of TE materials and devices using dispenser printing [49, 50]. The primary benefits of inkjet approaches to direct write are their speed and low cost. Although ink layers up to several hundred microns are possible, the aspect ratios are limited by the parameters of the printing technology and several layers are necessary to achieve the height of the needed structure. Parallel sets of inkjet print heads can be used for the rapid deposition of inks onto a substrate. Inkjet printing for the deposition of different kinds of materials and devices [51] including thermoelectric composite structures [52] and electronics [53] have been demonstrated.

1.2.6 Selective Laser Sintering (SLS)

Selective laser sintering is a powder-based fusion process where thin layers (100 μm) of powder that has been spread across the build area using a roller are fused using a laser. The part grows downward on the build platform as successive layers of powder are sintered together [9]. While SLS techniques have potential for preparing TE legs from powders, they are not well suited for the integrated fabrication of the TEGs. SLS has inherent limitations in depositing multiple materials. As a result, there have not been many efforts into utilizing SLS technology for thermoelectric material or device manufacturing.

1.2.7 Evaluation of AM techniques for TE manufacturing

The methods discussed above can be evaluated for their application to the fabrication of thermoelectric materials and devices. Table 1-1 shows the advantages and disadvantages of each method described earlier. While some of the above listed AM methods have suitable material properties, they are limited in thickness and size. For example, vapor deposition methods are well suited for fabricating high-quality thermoelectric materials but are not practical for the fabrication of an entire TE module. This is because a TE module requires multiple layers with different geometries and sizes, and the task of tuning both material and module fabrication parameters is difficult. It is useful to evaluate the AM techniques according to their module fabrication advantages. Thermal spray and dispenser printing seem suitable techniques for the fabrication of TE devices on flat and non-flat surfaces. As in most AM techniques, there is an inherent trade-off between material deposition, speed, and accuracy. It is also important to investigate the possibility of combining these techniques.

Table 1-1 Evaluation of AM techniques for thermoelectric devices

AM Method	Advantages	Disadvantages
CVD	Very good materials: High ZT., Conformal surfaces	Low deposition rate, expensive
ECD	Very high deposition rate. Can be patterned	Low ZT, low thickness
Sputtering	Good deposition rate. Average ZT value. Composition can be controlled	Annealing (or substrate heating) improves ZT. Composition difficult to control (depends on power).
PLD	Very good materials, High ZT.	Low deposition rate, low thickness
Thermal co-evaporation	High ZT. Good deposition rate. Control of film composition. Simple/inexpensive equipment.	Needs substrate heating. Needs precise control of deposition rate and crucible temperature.
Thermal Spray	Rapid deposition rates, novel phases,	Low ZT, previously not demonstrated

Screen Printing	Average ZT, simple process sequence, short processing time, low fabrication and equipment cost	Flat surfaces, multi-layer difficult, low material transfer efficiency
Dispenser Printing	Average ZT, thick coatings, high material transfer efficiency	Requires curing and sintering
SLS	High throughput	Difficult to fabricate with multiple materials

1.3 Motivation for Present Work

Much of the research effort in thermoelectrics is spent on finding new high-*ZT* materials or ways to improve the performance of existing ones. Although there is no generally accepted theoretical limit on *ZT* value, it is recognized that progress will be slow, and one should not wait for *ZT* to increase before committing to practical applications [54]. Since each application has its own set of requirements that vary in level of importance, it is more important to focus on competitive electricity cost (*cost per watt*) rather than efficiency when considering them.

The cost of a thermoelectric power generator system consists of the device cost and the operating cost. When considering waste-heat energy harvesting applications, the operating cost is negligible compared to the device cost. The device cost includes the cost of producing both the TEG module and system. A large share of the manufacturing cost is in material preparation and module assembly. Assembling many prefabricated pairs of legs into one module without soldering is a challenge and may require different solutions for different materials. Thermal expansion of all pairs further aggravates the stress accumulation. The device packing densities when using bulk elements is also restricted due to the physical limitations of pick and place methods. Contact resistance is a critical issue in designing TE system using prefabricated modules. Since the device operates under a large temperature difference, this leads to thermomechanical stress, diffusion and

chemical reactions between materials used at the interfaces. TE materials have high electrical conductivity and, therefore, very low electrical contact resistances are required between the materials and the electrodes. These problems limit the choice of materials to those with high electrical and thermal conductivities relative to the TE material. Thermal expansion coefficients should also match with that of the TE material. The TE materials should be chemically stable over the lifetime of the module. Because thermoelectric devices operate under large currents and a large temperature gradient, both electrical and thermal migration could occur. This necessitates the use of diffusion barriers to prevent the diffusion of certain electrode materials into the thermoelectric materials [55].

In addition, commercially available TEGs are flat, inflexible and are available in only a limited range of sizes. Efforts to incorporate them onto components with curved surfaces such as exhaust pipes, pump housings, steam lines, mixing containers, reaction chambers, etc. require custom-built heat exchangers. This adds cost and is labor-intensive, in addition to presenting challenges in terms of space, thermal coupling, added weight and long-term reliability. This potentially reduces their durability while also increasing manufacturing costs and energy use.

A *novel* approach that attempts to address both of these issues is to fabricate the thermoelectric devices *directly* onto the waste-heat component surfaces. The goal is to develop an integrated fabrication process whereby TEGs are fabricated using a combination of additive and subtractive techniques to fabricate the dielectric layers, conducting interconnects and active materials of the TEG directly onto the component. Because additive manufacturing can be used on conformal (non-flat) geometries, the flat module design is no longer a restrictive requirement. Additional cost savings can be realized by optimizing the device geometry and operating the device at a larger temperature difference.

Fabrication of Bi_2Te_3 based devices by vapor deposition of thin films (1–10 μm thick) to create in-plane architectures or dispenser printing of legs (10–120 μm) to create π-type architectures have been demonstrated. There have been few reported works of powder-based thick film fabrication of thermoelectric devices with a leg thickness of 1-2 mm thick. This is because of an inherent limitation in the printing process. A summary of reports utilizing dispenser printing or screen-printing techniques for TEG device manufacturing is shown in Table 1-2.

In addition, this work aims to develop cost-effective printing techniques that are compatible with larger surfaces and allows for better mass production than the conventional production techniques. Powder based thick film processing technologies offer a commercially attractive route for the low-cost manufacture of TEG devices.

Table 1-2 Examples of thermoelectric devices fabricated by ink printing

Architecture	**Processing**	**Materials**	**Material Thickness (μm)**	**TE legs**	**Thermo-power (μV/K)**	***ZT***	**Ref.**
Unileg Planar Design	Dispenser Printing	Bi_2Te_3	120	62	0.27	0.31@RT	[50]
Planar Design	Screen Printing	$(Bi,Sb)_2$-$(TeSe)_3$	80	5	123	0.61@RT	[46]
Thin film	Screen Printing	Bi_2Te_3	80	-	140		[45]
Planar design	Screen printing	$Bi_{0.85}Sb_{0.15}$ alloy	100	97	97	-	[56]

Device testing is another challenge facing the thermoelectrics community. Unlike PV cell efficiency measurements, thermoelectric device efficiency measurements require quantifying the heat input to the hotter side and the heat removed from the colder side and quantifying the electrical output, which is the maximum at the matched load. For constant properties, the maximum efficiency occurs when the external load is matched with the internal resistance. In reality, this load

matching is best achieved by using a programmable current source that runs in reverse to the current direction driven by the temperature gradient. The most difficult part of the efficiency measurements is in determining precisely the heat input or heat removed since the electrodes and thermocouples can all lead to additional thermal leakage. Careful calibration of the various heat losses is essential for an accurate determination of the efficiency. The thermoelectric community presently lacks a standard in efficiency measurements. This can be contrasted with the PV field, where efficiency is used to rate performance rather than material parameters. However, for practical applications, the cost of power generation – as governed by material, manufacturing, and heat exchanger costs – is also a critical factor that is not captured in *ZT* alone. The *ZT* parameter does not take into account the integration of a heat sink and a heat source.

A waste-heat recovery system typically consists of a TEG mounted on a heat source, the requisite electronics needed to condition the power output, and a battery to store and save the power for later use. The total energy extracted depends on the temperature gradient, system design, integration, and heat sink, all of which need to be optimized for power and efficiency.

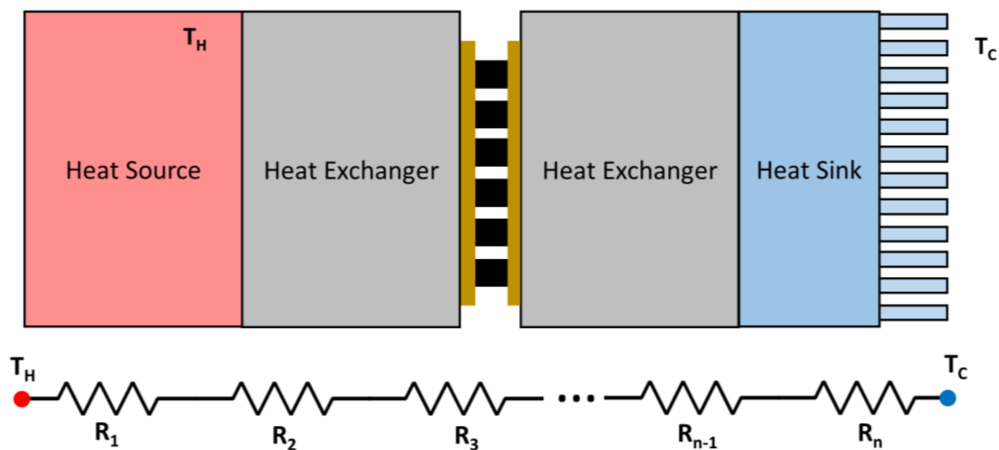

Fig. 1-4 Thermal resistive networks model used for design and analysis of TEG system

Waste-heat sources come in a variety of shapes and sizes. Adapting flat TEG modules to non-flat surfaces requires modifying the existing heat source to accommodate the TEG geometry. When designing TEGs for waste-heat recovery systems, it is important to consider thermal resistance matching of the TEG with the heat source. Proper matching of the thermal resistances of the TEG to the source provides a maximum temperature difference across the generator. A simplified thermal resistance model can be used to design and analyze a TEG waste-heat recovery system (Fig. 1-4). The total heat flow through the TEG system is given by:

$$Q = \frac{\Delta T}{\sum R_i} \qquad \text{(Eq. 1-1)}$$

where R_i represents the thermal resistance (K/W) of each component including the interfaces. Different values of thermal resistances of the heat exchangers at either side of the thermoelectric module have an influence on the performance of the system. Designing the heat exchangers and heat sinks with minimal thermal resistance can maximize the temperature difference and increase the power output. The addition of heat pipes can also help in improving the heat throughput from the device. Several cooling options are also explored including fan cooled and natural cooled systems.

1.4 New contributions from this work

The new contributions from this work include the development of additive and subtractive manufacturing techniques for TE device fabrication. Overall, significant is achieved progress towards developing an integrated, one-step process to fabricate thermoelectric materials, bonding materials, and electrical contacts using AM. This approach will largely resolve the interface, durability, and heat transfer issues prevalent with the conventional approach of integrating pre-fabricated TE

modules onto exhaust components. Figure 1-5 provides a summary of current research areas and enabled future research directions.

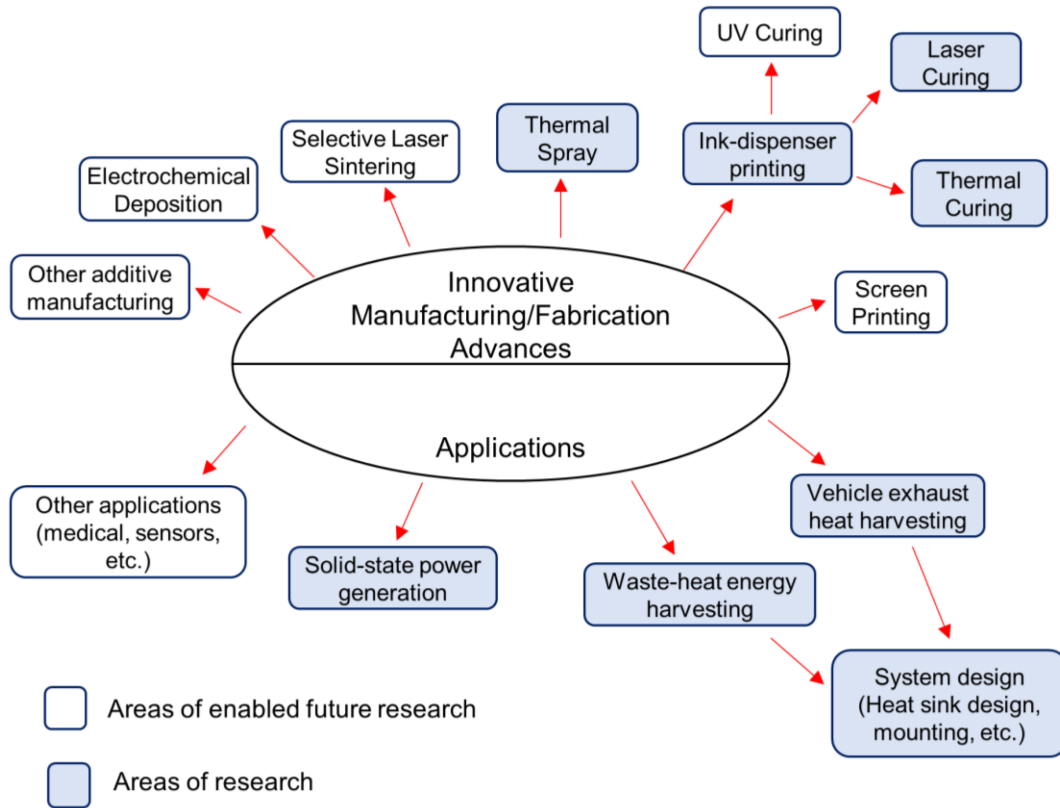

Fig. 1-5 Overview of current and future research

The feasibility of using thermals spray, ink-dispenser printing, and laser micromachining as a novel route for TE device fabrication was confirmed. Technique for bridging the air gap between adjacent thermoelectric elements for the top layer based on a sacrificial filler material was also demonstrated. A flat (50.8 × 50.8 mm) TEG module is fabricated *for the first time*, using thermal spray. The steps required to fabricate a thermoelectric device are developed, including the formation of the bottom and top metallic layers and the thermoelectric. The feasibility of dispenser printing as technique for the fabrication of TE materials is also demonstrated. This includes the optimum printing variables such as ink, viscosity, pressure, shot height and shot spacing.

In addition, the optimization of laser parameters for successful electrical isolation needed in thermal spray device manufacturing and high-quality feature machining was demonstrated. The optimum laser parameters that minimize the heat-affected zone and resulted in the fastest processing times are determined. Finally, the application of a TEG-based sensor for nuclear power plants monitoring was also demonstrated.

1.5 Scope of Dissertation

Chapter 2 introduces thermoelectric phenomena, thermoelectric devices and application of thermoelectricity. Background on TE device configuration, performance and efficiency are also provided.

Chapter 3 investigates the feasibility of using thermal spray for the manufacturing route of thermoelectric materials and devices. The challenges encountered are outlined and solutions are proposed which are verified experimentally.

Chapter 4 presents a description of different subtractive manufacturing techniques for thermoelectric device fabrication. Laser micromachining of thermal spray coatings is investigated in detail with both experiments and modeling.

Chapter 5 presents results from the feasibility studies that are used to fabricate a working TEG using thermal spray directly onto engineering components. The steps required to fabricate a thermoelectric device are presented, including the formation of the bottom and top metallic layers and the thermoelectric legs. The results from the characterization of the fabricated module are also discussed.

Chapter 6 investigates ink-dispenser printing as a fabrication route for high-quality thermoelectric materials. This includes material development for ink-dispenser printing and the optimization of printing techniques.

Chapter 7 presents the application of thermoelectric generators in waste-heat energy harvesting. A case study for the application of thermoelectric generators for powering sensors in small modular nuclear reactors is presented. Results from the characterization of various commercial TE modules is presented.

Finally, Chapter 8 summarizes the key research findings and proposes future research directions.

Chapter 2

Theory and Application of Thermoelectric Devices

In this chapter, background on thermoelectricity is presented including the Seebeck effect, the Peltier effect and the Thomson effect. The fundamental equations of a thermoelectric device arising from the direct coupling of heat and electricity are provided.

2.1 Thermoelectric Phenomena

In 1821, Thomas J. Seebeck observed that an electromotive force or a potential difference is produced across the junction of two dissimilar metals held at different temperatures. This phenomenon is called the *Seebeck* effect. Fig. 2-1 shows a circuit made from two dissimilar materials (A and B) soldered together at two points which are kept at temperatures T_H and T_C, respectively maintaining a temperature difference, ΔT, across them.

Because the electrons on the hotter side have more kinetic energy than those on the colder side, they diffuse across the temperature gradient resulting in a voltage difference that can be measured at the contacts. This relative voltage measured is proportional to the temperature difference and is known as the Seebeck voltage.

$$V \propto \Delta T \qquad \text{(Eq. 2-1)}$$

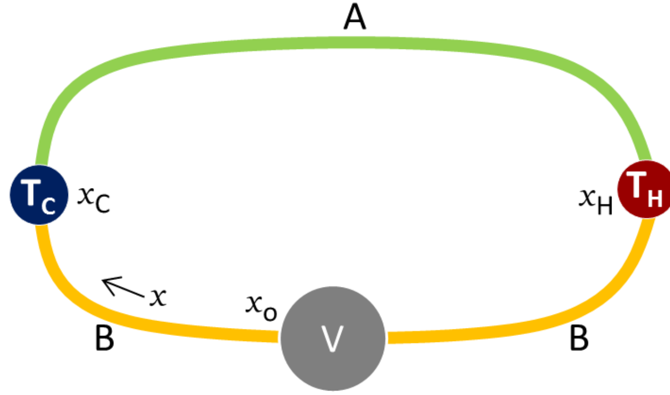

Fig. 2-1 Thermoelectric circuit composed of two different materials A and B

In practice, one rarely measures the absolute Seebeck coefficient because the voltage read is the relative Seebeck voltage between the two wires. This can be seen from the microscopic description of the temperature dependent Seebeck coefficient, which is obtained by taking an infinitesimal temperature difference to relate the local temperature gradient to the local potential gradient and expressed as:

$$\alpha(T) = \lim_{\Delta T \to \infty} \frac{\Delta V}{\Delta T} \qquad \text{(Eq. 2-2)}$$

The total voltage measured at the end of one rod is given by the path integral along the rod:

$$V = \int_{x_C}^{x_H} \alpha(T) \frac{\partial T}{\partial x} dx = \int_{T_C}^{T_H} \alpha(T) dT \qquad \text{(Eq. 2-3)}$$

The relative Seebeck voltage is expressed in terms of the absolute Seebeck coefficients of materials A and B. The path integral around the rods is evaluated to obtain the total Seebeck voltage across the whole circuit. The contact potentials at the soldered points cancel out and by averaging the temperature dependent coefficients along the rods, the Seebeck coefficient for the combined material couple at the given temperature difference is given by:

$$V = (\bar{\alpha}_B - \bar{\alpha}_A)\int_{T_C}^{T_H} dT = (\bar{\alpha}_B - \bar{\alpha}_A)\Delta T = \bar{\alpha}_{AB}\Delta T \qquad \text{(Eq. 2-4)}$$

Materials can have positive or negative Seebeck coefficients (*p*-type *or n*-type) based on their majority carrier type. Typically, materials with Seebeck coefficients of opposite sign are chosen to maximize the resulting voltage. The Seebeck coefficient of most metals is in the range of 1-10 μV/K while semiconductors have Seebeck values of 1-10 mV/K. Some organic materials have high Seebeck values, even millivolts per Kelvin[4]. The Seebeck effect is used in temperature measurement applications in thermocouples as shown in Fig. 2-2. Because the Seebeck coefficients of many metals have been measured, the voltage measured between two metal junctions can be used for temperature measurement applications. Practical TE devices are made from semiconductors, which are normally brittle, and cannot be drawn into a wire to form a junction as in metallic thermocouples. They require a metal strip (copper, aluminum, etc.) to form a thermoelectric junction (TE leg) as shown in Fig. 2-2.

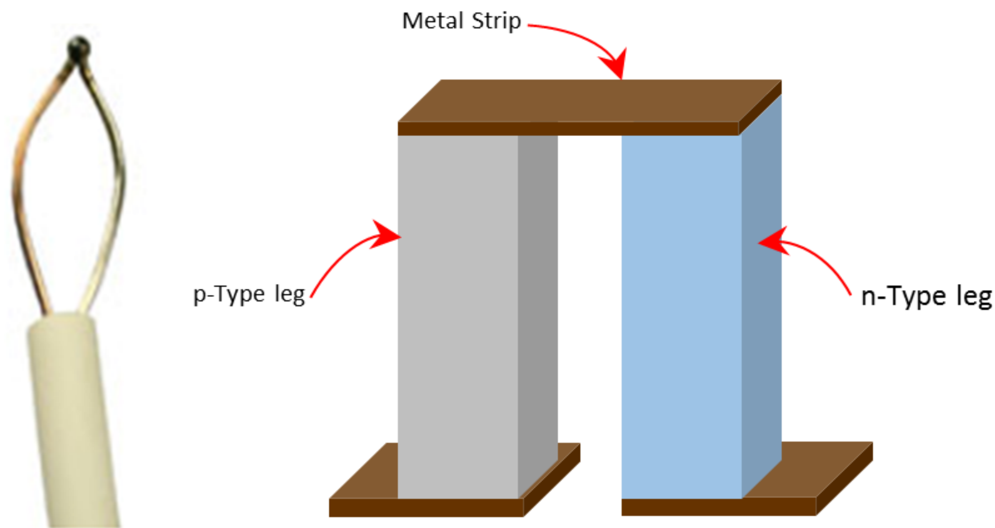

Fig. 2-2 Commercial thermocouple (left) and thermoelectric legs (right)

Table 2-1 Seebeck coefficients for selected materials at 300 K [4, 57]

Metals		Semiconductors		Organic Materials	
Material	**α [μV/K]**	**Material**	**α [μV/K]**	**Material**	**α [μV/K]**
Copper	6.5	Se	900	PEDOT:PSS	27.3
Nickel	-15	n-Bi_2Te_3	-230	P3HT: TFSI	50
Nichrome (NiCr)	25	p-$Bi_{2-x}Sb_xTe_3$	300	PEDOT: ClO_4	74
Constantan	-35	PbTe	-180	PEDOT: TOS	40

In 1834, Jean Charles Peltier observed that a temperature gradient is established when current flows through the junction of two dissimilar materials. Heat must be continuously added or subtracted at the junction to keep its temperature constant. The heat is proportional to the current flow and changes sign when the current is reversed. In 1838, Lenz realized that both the material combination and the direction of the current flowing could control whether the junction is heated or cooled. This phenomenon is known as the Peltier effect. The heat absorbed or released at the junction is given by:

$$\dot{Q}_\pi = \pi_{AB}\, I \qquad \text{(Eq. 2-5)}$$

where π_{AB} is the Peltier coefficient and the sign heat flow depends on the direction of the current applied as shown in Fig 2-3. The heating or cooling is reversible between heat and electricity and is the basis for solid-state cooling applications.

A third thermoelectric effect, known as the Thomson effect, was discovered by Thomson (and later Lord Kelvin) after relating the Seebeck and Peltier coefficients. Assuming that we have a homogeneous conductor with a temperature gradient applied, carriers traversing the temperature gradient gain or release energy depending on their relative direction to the temperature gradient, and on applying local energy balance, the energy change of the traversing carriers is absorbed or released as heat, respectively. The total Thomson heat absorbed or released along one rod in Fig. 2-3 is given by

$$\dot{Q}_\mu = \int_{T_C}^{T_H} \mu(T) I dT = \bar{\mu} I \Delta T \qquad \text{(Eq. 2-6)}$$

where $\mu(T)$ is the temperature-dependent Thomson coefficient.

Together, these three effects are known as *thermoelectric effects* [4, 58].

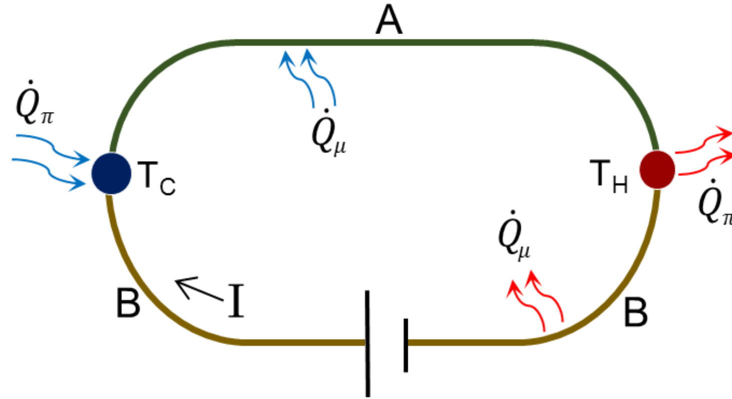

Fig. 2-3 Schematic for the Peltier effect and Thomson effect

All the thermoelectric coefficients discussed above are, in general, dependent on the magnetic field, *B,* with the principal parameters used in thermoelectrics [4]. Two important effects are the Nernst effect, *N*, where a transverse electric field E_y is produced by a longitudinal temperature gradient d*T*/d*x* in the presence of a magnetic field B_z. In the Ettingshausen effect, *T*, if an electric current, I_x, is passed through the sample in the *x* direction in the presence of a magnetic field B_z, a temperature gradient is set up in the *y* direction [59].

$$|N| = \frac{E_y}{B_z}\frac{dT}{dx} \qquad \text{(Eq. 2-7)}$$

$$|T| = \frac{1}{I_x B_z}\frac{dT}{dy} \qquad \text{(Eq. 2-8)}$$

2.2 Thermodynamics of Thermoelectric Phenomena

The three main *reversible* thermoelectric phenomena are related based on fundamental thermodynamics with two other *irreversible* processes, namely heat dissipation and heat conduction [60-62]. As heat and electrical current flow through the thermoelectric material, both heat dissipation (Joule heating) and heat conduction occur. However, by neglecting these effects, and applying the principle of conservation of energy, thermodynamics relations between the Seebeck, Peltier, and Thomson coefficients can be derived.

$$W = \dot{Q}_{\pi} + \dot{Q}_{\mu} \qquad \text{(Eq. 2-9)}$$

$$I\alpha_{AB}\Delta T = I\pi_{AB}(T_H - T_C) + I\int_{T_C}^{T_H}(\mu_B - \mu_A)dT \qquad \text{(Eq. 2-10)}$$

Rearranging equation 1-10, we obtain

$$\alpha_{AB} = \frac{\pi_{AB}(T_C + \Delta T) - \pi_{AB}(T_C)}{\Delta T} + \frac{1}{\Delta T}\int_{T_C}^{T_C+\Delta T}(\mu_B - \mu_A)dT \qquad \text{(Eq. 2-11)}$$

The energy relation between the three effects is obtained by letting ΔT approach zero.

$$\alpha_{AB} = \frac{d\pi_{AB}}{dT} + \mu_B - \mu_A \qquad \text{(Eq. 2-12)}$$

Second law effects must also be considered in regards to the entropy of the system. The approximation that thermoelectric circuits may be treated as being thermodynamically reversible simplifies the analysis of their relationships [4]. Thus, the net change in entropy of the entire process may be approximated as being equal to be zero. However, due to heat conduction and heat dissipation, the total entropy of the process will increase [63]. There is an analogy between a classical heat engine and a thermoelectric generator. Whereas the transfer of entropy in heat engine is by a working fluid, electrons are responsible for the transfer of entropy in a thermoelectric engine. Irreversibility is introduced from entropy sources such as non-adiabatic carrier heat transfer (joule

heating). Nonequilibrium thermodynamic theory is used to treat the relationship between the irreversible transport of heat and charge along a temperature gradient [61].

2.3 Thermoelectric Figure of Merit (*ZT*)

The thermoelectric figure of merit (*ZT*) is a dimensionless parameter that describes how well a thermoelectric material can convert heat into electricity at a given absolute temperature, *T*, and is expressed as:

$$ZT = \frac{S\sigma^2}{\kappa_e + \kappa_l} \qquad \text{(Eq. 2-13)}$$

where *S* is the Seebeck coefficient, σ is the electrical conductivity and κ_e and κ_l are the electronic and lattice contributions of the thermal conductivity, respectively. The numerator $S^2\sigma$ is known as the *power factor*. Favorable thermoelectric materials should have reasonably high electrical conductivity combined with low thermal conductivity, in addition to having high Seebeck values. Due to the interdependence of these three transport properties, it is challenging to optimize one parameter without affecting the others. Such materials are hard to find in nature and difficult to engineer. For most materials, it is difficult to alter the property of individual parameters independently, especially σ and κ (as κ is reduced, σ also is reduced).

Boltzmann transport theory describes both electrical and thermal transport in a majority of crystalline solids and provides a general understanding of the Seebeck coefficient and electrical conductivity. The Seebeck coefficient and the electrical conductivity can be expressed as:

$$S = \frac{8\pi^2 k_B^2}{3eh^2} m^* \left(\frac{\pi}{3n}\right)^{\frac{2}{3}} \qquad \text{(Eq. 2-14)}$$

$$\sigma = ne\mu \qquad \text{(Eq. 2-15)}$$

where k_B is the Boltzmann constant, e is the carrier charge, h is Planck's constant, m^* is the effective mass of the charge carrier, n is the carrier concentration, and μ is the carrier mobility [4]. Metals have high electrical conductivity since a partly filled conduction band allows electrons to move freely in the crystal as described by the free-electron or nearly-free electron model[64]. The Wiedemann-Franz law states that the total thermal conductivity of a solid is the sum of two independent components, a lattice contribution, κ_l and an electronic contribution κ_e. According to the Wiedemann-Franz law,

$$\kappa_e = L\sigma T \qquad \text{(Eq. 2-16)}$$

where L is the Lorenz number, taken as 2.4×10^{-8} W·Ω·K^{-2} in metals [4]. The Lorenz number is a quantitative measure of a materials' relative ability to conduct heat with respect to its ability to conduct electrical charge. The thermal conductivity of insulators only depends on the phonon (lattice) contribution [64]. From equations 2-14, 2-15 and 2-16, it can be seen that thermoelectric parameters are strongly interrelated and often follow opposing trends. For example, if the charge carrier concentration, n, is increased, the Seebeck coefficient decreases accordingly and the electrical conductivity increases as shown in Fig 2-4.

Charge carriers carry heat, but phonons do not carry a charge. They may indirectly heat electrons by the transfer of heat energy from the lattice to the electrons. Good thermoelectric materials call for materials with electrical conductivity comparable to metals but with thermal conductivity similar to glasses. These are so-called *phonon-glass electron-crystals*.

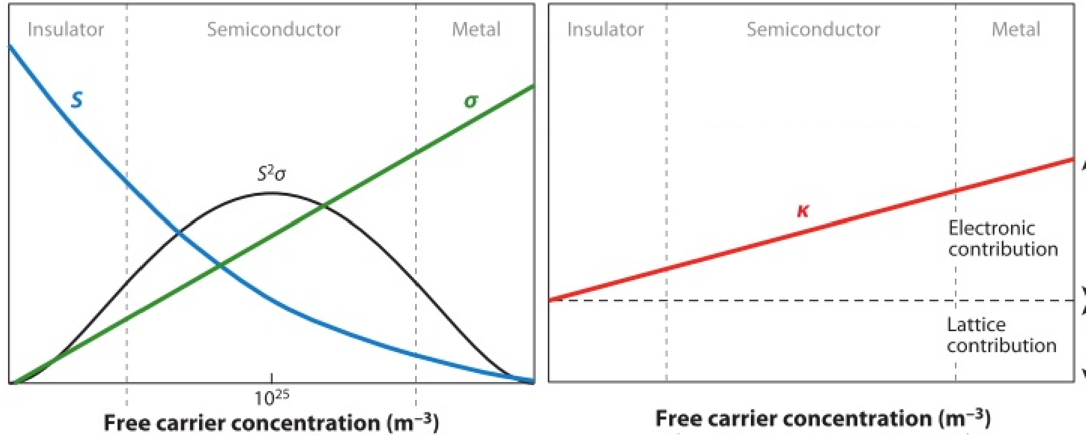

Fig. 2-4 Trade-off between electrical conductivity (σ), Seebeck coefficient (S), and thermal conductivity (κ) that involves increasing the number of free carriers from insulators to metals [65]

Metals have poor *ZT* due to their low Seebeck values (< 50 μV/K) and high thermal conductivities. The conductivity of metals decreases with impurities that function as scattering sites for electrons. Insulators have poor *ZT* have due to their reduced electrical conductivity (Table 2-2). Semiconductors have thermal conductivities lower than that of metals with a majority of the contribution coming from the lattice. The conductivity of semiconductors decreases with increasing temperature as electron-phonon scattering is promoted at a higher temperature. The best thermoelectric materials are semiconductors that are heavily doped so that their transport properties resemble metals [66]. Semiconductors have the highest power factor due to their moderate Seebeck coefficients and electrical conductivities. Further improvements to *zT* can be made by reducing the thermal conductivity without reducing the electrical conductivity. In semiconductors, rigorous analysis of carrier transport shows that the sign of the Seebeck coefficient depends on the asymmetry of the density of states (DOS) near the Fermi level [66]. The electrical conductivity of semiconductors increases with impurities that serve as dopants. The electrical conductivity also increases with temperature because the Fermi distribution extends into the conduction and valence bands with increasing temperature, further increasing the carrier concentration.

Table 2-2 Comparison of thermoelectric properties of metals, semiconductors and insulators at 300 K [67]

Properties	Metal	Semiconductor	Insulator
S (μV/K)	~1	~10^2	~10^3
σ (1/Ω·m)	~10^8	~10^5	~10^{-10}
κ (W/m·K)	~10-10^2	~1-10^2	~10^{-2}
z (K^{-1})	~10^{-5}-10^{-6}	~ 10^{-2}-10^{-1}	~10^{-14}

2.4 Thermoelectric Materials

The discovery of the thermoelectric phenomena did not immediately lead to applications such as cooling or power generation, due to the lack of efficient thermoelectric materials. In 1911, Edmund Altenkirch paved the way for the formulation of the thermoelectric figure of merit by concluding that high-quality thermoelectric materials are characterized by high Seebeck coefficients, high electrical conductivities and low thermal conductivities [68]. However, materials satisfying these requirements were extremely difficult to find in nature.

In the 1950s, semiconductors meeting these requirements became widely available, resulting in intensified research activity. The discovery of Bi_2Te_3-based semiconductors opened up opportunities for energy generation and refrigeration applications. It was during this time when Ioffe formulated the basis of modern thermoelectric theory [4, 69, 70]. The efficiency of thermoelectric generators could be raised to due to the favorable material properties of semiconductors. The thermoelectric figure of merit became an important tool for evaluating candidate TE materials. Continued materials research led to the successive discovery of materials with increasing *zT* over a wide range of temperature ranges. The basic configuration of a thermoelectric generator was also established during this time. Over the following three decades (1960–1990), the thermoelectric industry grew steadily by finding niche applications for space missions, laboratory equipment, and medical applications. For example, in the 1970s, research also focused on the development of

radioisotopic generators (RTGs) for long-range space vehicles. During this period, materials research received little attention from the worldwide scientific research community. Starting in the early 1990s, theoretical predictions suggested that thermoelectric efficiency could be greatly enhanced through nanostructural engineering (material modification in the atomic range), which led to experimental efforts to demonstrate the proof-of-principle and high-efficiency materials. Also, new families of advanced bulk thermoelectric materials (such as Skutterudites, Clathrates, and half-heusler alloys) were explored and found to have high efficiencies [66, 71].

Research in bulk materials emphasizes the reduction of thermal conductivity and distorting the electronic density of states with resonant impurity levels. Nano-structuring can reduce the relationship between thermal and electrical properties by introducing new scattering mechanisms for *ZT* enhancement. Tuning the electronic structure to obtain a narrow density of states (DOS) around the Fermi level increases the Seebeck coefficient in these materials [4]. These methods either reduce the thermal conductivity of the materials or increase the Seebeck coefficient and electrical conductivity, or a combination of both for an overall improvement in *ZT*. These techniques are also used to achieve low thermal conductivities by having a microstructure that can significantly reduce the lattice part of the thermal conductivity while leaving the electronic part as high as possible. Good thermoelectrics are therefore crystalline materials that manage to scatter phonons without significantly disrupting the electrical conductivity [66]. These methods have been successful in yielding high *ZT* values. Thermoelectric materials based on these techniques have a non-uniform structure and their properties vary considerably from bulk values. As a result, understanding their properties from a pure crystal structure model is not possible. The other approach is to search for new materials capable of operating over broader temperature regimes.

Research in thermoelectricity has resulted in the development of a wide range of TE materials, which are summarized in Table 2-3. Among the vast number of materials known, relatively few have been viable as TE materials, and even fewer have been used commercially. Because a thermoelectric material operates at its maximum efficiency at a specific temperature, different materials are needed for temperature ranges. Bismuth telluride (Bi_2Te_3) based alloys are the most common thermoelectric materials near room temperature. Doping Bi_2Te_3 with Selenium (Se) makes it *n*-type material and doping with Antimony (Sb) make it *p*-type material. Bi_2Te_3 with superlattice structures have ZT values as high as 2.4 at 300 K reported [72]. While Bi_2Te_3 is the most common TE material used, the cost of Tellurium and limited temperature range limit its application for high-temperature applications. For mid-temperature power generation (500–900 K), materials based on group-IV tellurides (PbTe, GeTe or SnTe) are used. Successful, high-temperature (>900 K) thermoelectric generators have typically used silicon–germanium alloys for both *n*- and *p*-type legs. Lead telluride or one of its alloys can be used at temperatures of up to 900 K and silicon-germanium alloys are used up to 1300 K. Oxides with metal atoms which are stable at elevated temperatures that show promising thermoelectric properties include $Ca_3Co_4O_9$, ZnO, and $SrTiO_3$ [73]. Figure 2-5 shows the ZT, for various temperatures of the state-of-the-art thermoelectric materials. Notable reviews about recent advances in TE materials and applications are available in the literature [54, 74]. The cost and complexity of many of these materials – even though they have very attractive *ZT* – make them unrealistic for many practical applications.

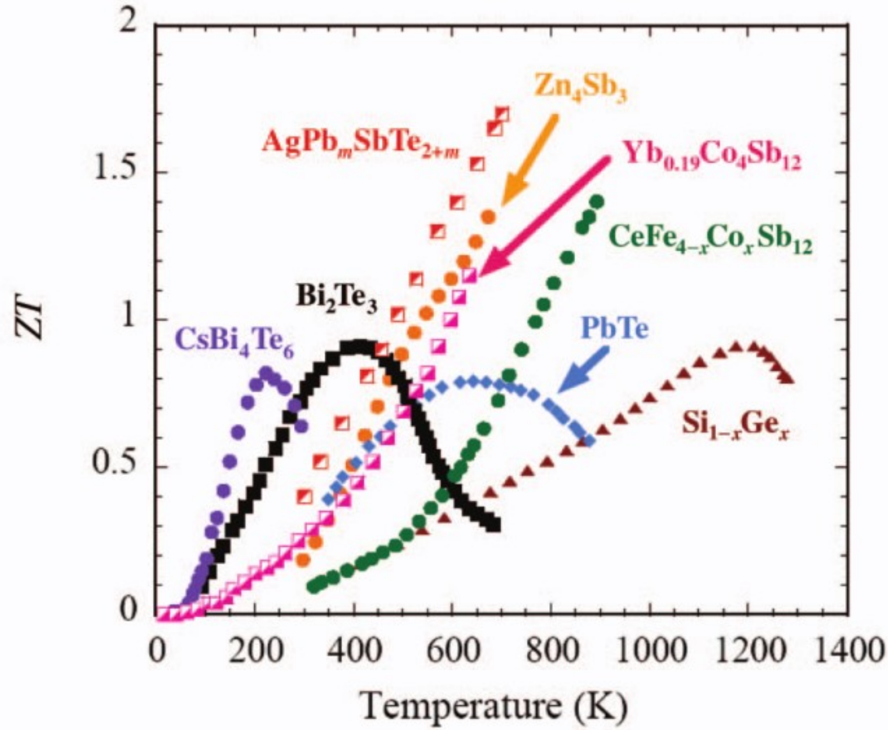

Fig. 2-5 Figure of merit (*ZT*) as a function of temperature for several bulk thermoelectric materials [1].

Table 2-3 Summary of current thermoelectric materials [4, 66, 75]

Thermoelectric Material Class	Examples	Properties
BiTe alloys	$Bi_2Te_{2.7}Se_{0.3}$ $Bi_{0.5}Sb_{1.5}Te_3$	Most established material, High *ZT*, expensive
IV-VI compounds	Si-Ge	Environmentally benign, High-temperature performance
Skutterudites	$Yb_{0.19}Co_4Sb_{12}$, $Na_{0.48}Co_4Sb_{12}$	High efficiency, Lower-lattice thermal conductivity
Clathrates	$Sr_8Ga_{16}Ge_{30}$, $(Cl_2)_8(H_2O)_{46}$	Tunable thermal conductivity
PbAgSbTe (LAST) compounds	$AgPb_mSbTe_{2+m}$	High *ZT*
Chalcogenides	PbTe-SnSe, PbSe-SnSe, SnTe-SnSe	High *ZT*
Half-Heusler alloys	MNiSn, MgAgAs	High thermopower, Environmentally benign
Ceramic oxides	$Ca_3Co_4O_9$, ZnO	High temperature performance
Organic Thermoelectrics	PEDOT, PANI, and TTF-TCNQ	Very low thermal conductivity, Moderate electrical conductivities

2.5 Thermoelectric Device Configurations

In general, a thermoelectric device consists of alternating rows of *p*- and *n*- type thermoelectric elements arranged in series to provide increased voltage output of the device. Thermoelectric modules are constructed by assembling many of these thermoelectric couples. A serial configuration is used to enhance the output voltage and minimize parasitic losses in series electrical resistance of wires and interconnects. For the thermal arrangement of TEGs, there are two different design architectures: *vertical* design and *planar* design, each with different variations. The vertical π–design is the most popular design when using thick TE legs with high current densities and low voltages (Fig. 2-6a). The individual thermoelectric elements are arranged electrically in series and thermally in parallel, which increases the operating voltage of the module while reducing its electric current. This design is also popular because the temperature gradient is perpendicular to the substrate. An advantage of this type of design is that multiple devices can be cascaded to form multi-stage devices, which can operate over a wide range of temperature ranges. A variation of this vertical architecture is the uni-layer approach (Fig. 2-6b), which uses either the *n*-type or *p*-type material [73]. In this case, the thermoelectric legs are linked thermally in parallel and electrically in series with the connecting electrical connections now running top-to-bottom, linking the hot and cold sides of the TEG. The voltage generated by each module in the uni leg design is smaller, but the metal conductor between the hot and cold ends of the module may occupy less space than the thermoelectric element [73]. The metal conductor must be kept small to reduce the heat transfer between the hot and cold sides of the module. Other common variations of the π–design architecture such as segmented and linear segmented are shown in Fig. 2-6c, d.

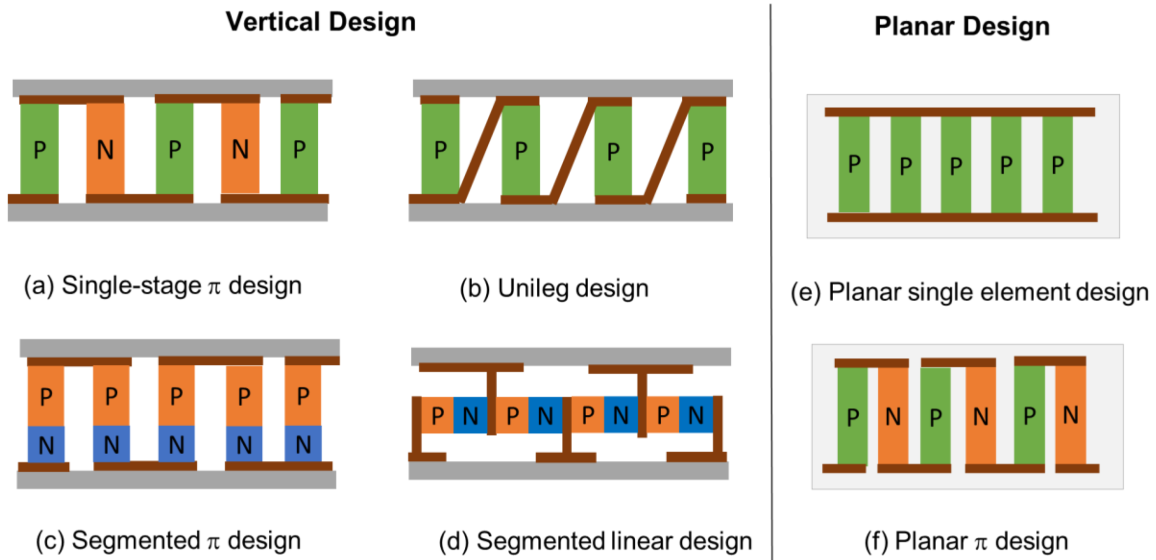

Fig. 2-6 Common design architectures of TE devices (vertical and planar designs)

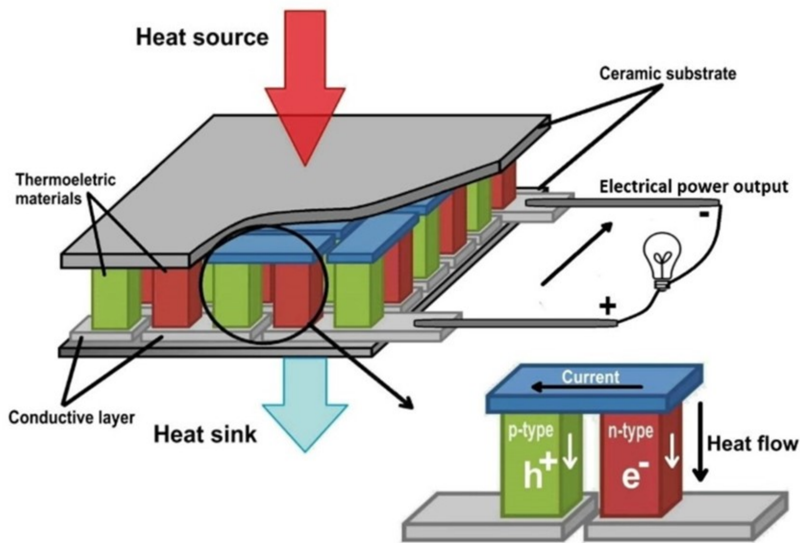

Fig. 2-7 Schematic of a typical π-type single-stage thermoelectric device

Thin-film manufacturing techniques have opened up the possibility of utilizing planar or lateral structures that use one or both *p*- and *n*-type materials (Fig. 2-6e, f). In such structures, the thermal flux no longer passes from the top face to the bottom face through the device but instead flows parallel to the film. Significant losses can occur if the thermal conductivity of the substrate

is comparable to that of the thermoelectric materials. This loss can be mitigated by using thin substrates that reduce the parasitic transmission losses.

Improvement in the design of TE devices is critical to utilizing the gains in improved material ZT values. Numerous parasitic losses in a TE device stemming from packing, soldering and contact resistance lower the efficiency below the predicted values based on the material's efficiency. Thus, the efficiency of a TEG, or the device figure of merit ($\overline{ZT}$) will depend on factors beyond simply the material properties. It is important to understand and reduce these losses as much as possible by analyzing the heat flow through a thermoelectric device and to determine the losses along the path.

Device design techniques involve analyzing the heat transfer along a single TE leg to determine an expression for the overall $\overline{ZT}$ of the device. The equivalent circuit for the thermoelectric voltage generation is illustrated in Fig. 2-8. The thermally parallel configuration allows the same level of increase the heat flux throughout the entire device at the same thermal gradient.

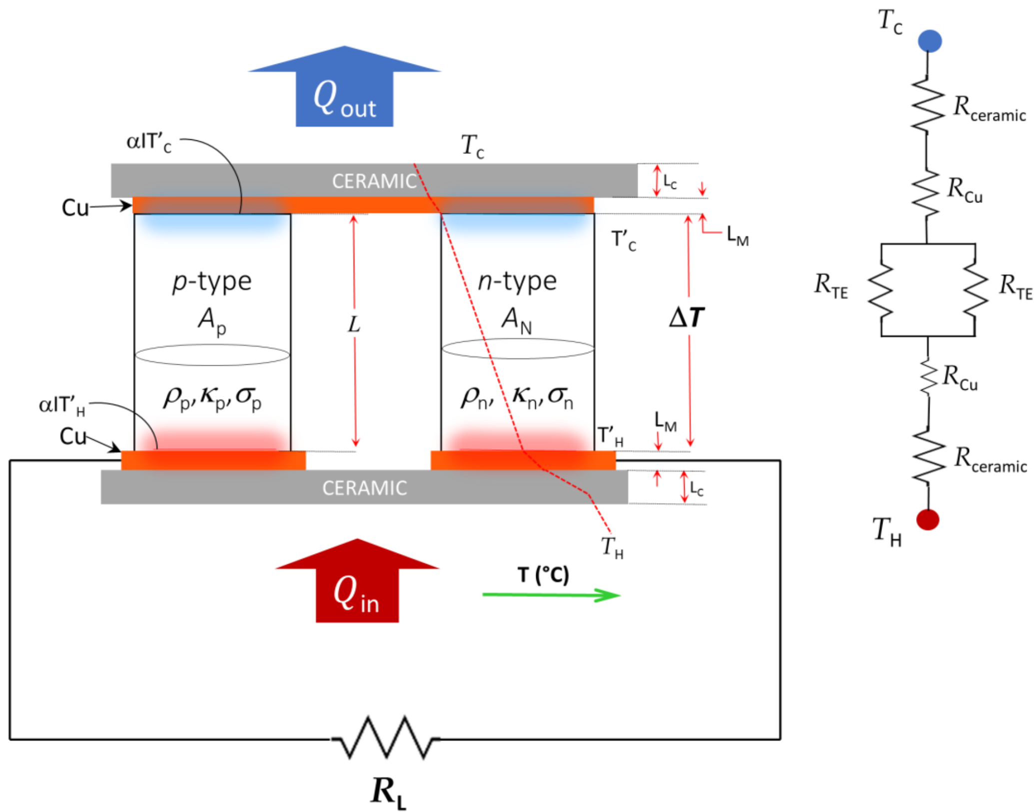

Fig. 2-8 Heat transfer within a thermoelectric generator

The total thermal conductance G for the TE element is calculated from the resistor model shown in Fig. 2-8. If only the TE legs are considered, the thermal conductance of the two branches in parallel is given by:

$$G = G_p + G_n = \frac{k_p A_p}{L} + \frac{k_N A_N}{L} \quad \text{(Eq. 2-17)}$$

The electrical resistance of the two branches in series is given by:

$$R = R_p + R_n = \frac{\rho_p L}{A_P} + \frac{\rho_N L}{A_N} \quad \text{(Eq. 2-18)}$$

The magnitudes of the heat input and output (assuming that half of the Joule heat ($\frac{1}{2}I^2R$) is absorbed at the heat source while the other half is absorbed at the heat sink) [69] are given by:

$$Q_{in} = \sigma_{np} T'_H I + G\Delta T - \frac{1}{2} I^2 R \quad \text{(Eq. 2-19)}$$

$$Q_{out} = \sigma_{np} T'_C I + G\Delta T - \frac{1}{2} I^2 R \quad \text{(Eq. 2-20)}$$

where T'_H and T'_C are the hot and cold side temperatures of the thermoelectric legs and ΔT is the temperature difference across the legs as shown in Fig. 2.8. The voltage and power generated from TEG are given by:

$$V_L = \sigma_{np} \Delta T \frac{R_L}{R_L + R} \quad \text{(Eq. 2-21)}$$

$$P_L = R_L \left(\frac{\sigma_{np} \Delta T}{R_L + R} \right)^2 \quad \text{(Eq. 2-22)}$$

where V_L is the load voltage, P_L is the output power, R and R_L are the internal resistance of TEG and load resistance, respectively, and ΔT is the temperature difference between the two sides of TEGs. The conversion efficiency is the ratio of electrical power delivered to the load of resistance R_L relative to the thermal power input:

$$\eta = \frac{I^2 R_L}{Q_{in}} = \frac{I^2 R_L}{\sigma_{np} T'_H I + G\Delta T - \frac{1}{2} I^2 R} \quad \text{(Eq. 2-23)}$$

This expression may be simplified by eliminating the current:

$$I = \frac{\sigma_{np} \Delta T}{R + R_L} = \frac{\sigma_{np} \Delta T}{R(1 + m)}; \;\; m = \frac{R_L}{R} \quad \text{(Eq. 2-24)}$$

where m is a parametric measure of the load resistance relative to the generator resistance. The efficiency expression then becomes:

$$\eta = \frac{I^2 R_L}{(1 + m) T'_H + \frac{(1 + m)^2}{Z} - \frac{\Delta T}{2}} \quad \text{(Eq. 2-25)}$$

where z is the thermoelectric figure of merit of the TE material pairs expressed by:

$$Z = \frac{\left(\alpha_p - \alpha_n\right)^2}{GR} \qquad \text{(Eq. 2-26)}$$

Conversion efficiency and power out are two key parameters needed to evaluate the performance of a TEG. The maximum power, at matched load ($R = R_L$) and the maximum efficiency are given by:

$$P_{max} = \frac{\left(\alpha_{np}\Delta T\right)^2}{4R} \qquad \text{(Eq. 2-27)}$$

$$\eta = \frac{\left(1 - \frac{T_c}{T_h}\right)}{\frac{2T'_C}{T'_H}\left(1 + \frac{T'_C}{T'_H}\right) + 2 - \frac{1}{2}\left(1 - \frac{T'_C}{T'_H}\right)} \qquad \text{(Eq. 2-28)}$$

If the contact resistances of the conducting interconnects are taken into account, a similar expression for the maximum power density and efficiency of a single TE device when operated under a matched load condition can be derived [76].

The efficiency of a TEG depends on factors other than the maximum ZT of the material. This is primarily due to the temperature dependence of all the materials properties (α, σ, κ). The device figure of merit $\overline{ZT}$ is lower than the material's figure of merit ZT [77]. The efficiency η of a TEG is given by:

$$\eta = \eta_{CR}\frac{\sqrt{1 + \overline{ZT}} - 1}{\sqrt{1 + \overline{ZT}} - T_C/T_H} \qquad \text{(Eq. 2-29)}$$

where η_{CR} is the limiting Carnot efficiency, and T_H and T_C are the hot side and cold side temperatures, respectively [78]. Figure 2-9 shows the power generation efficiency of TEG as a function of

heat source temperature at different ZT values in comparison to various conventional power generation technologies. The Carnot limit specifies limits on the maximum efficiency that any heat engine can obtain. The Carnot limit, given by $(T_H - T_C)/T_H$, solely depends on the temperature difference between the hot and cold temperature reservoirs.

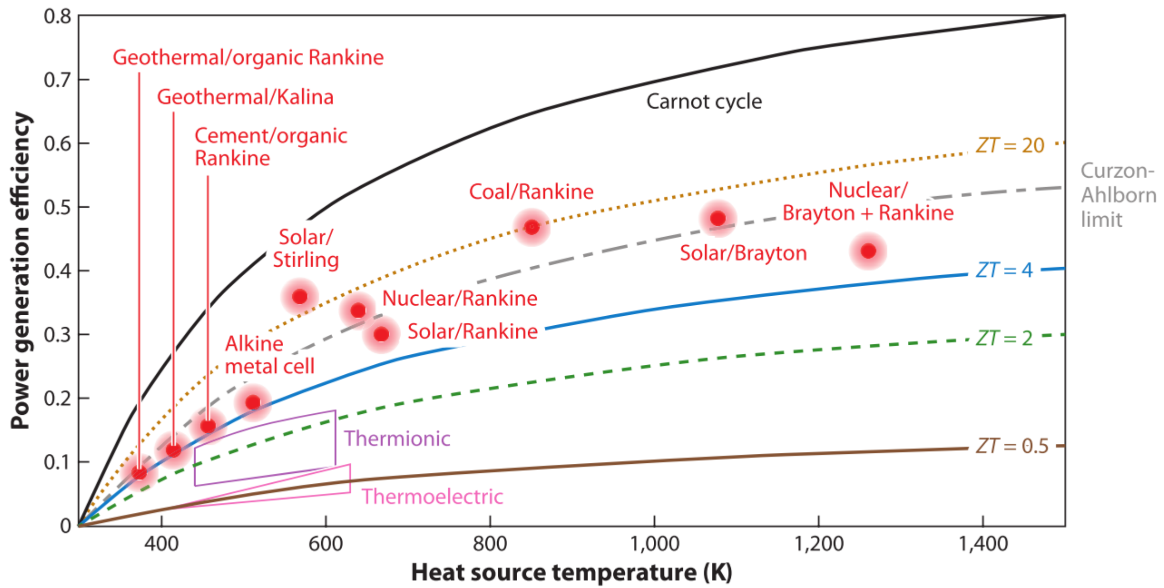

Fig. 2-9 The efficiency of TEGs with the corresponding ZT and comparison of thermoelectric power generation efficiency with conventional engines [65]

2.6 Application of Thermoelectric Devices

Applications for thermoelectric modules cover a wide spectrum of product areas. These include equipment used by military, medical, industrial, consumer, laboratory, and telecommunications organizations. Thermoelectricity is an important field for the development of environmentally friendly thermal systems. Due to their solid-state nature and the lack of moving parts, thermoelectric generators have long service lifetimes and extremely long maintenance intervals. While these qualities are beneficial in a series of remote applications, under extreme conditions new applications have also been enabled. Applications range from small to large thermal systems including

heat exchangers, calorimeters, lasers, constant temperature baths, scientific instruments, integrated circuit cooling, infrared detectors, power generators and refrigeration systems.

The most prevalent application is as thermocouples for temperature measurements. The initial configuration of TE as illustrated in Fig. 2-2 is used for temperature measurement applications [79]. In measurement applications, high Seebeck coefficients are less important than a linear behavior in the desired temperature range. Metallic alloys, which have slightly higher Seebeck coefficients than pure metals, have been used as thermocouple materials. Typical materials for thermocouples used in temperature measurement applications are alloys of nickel with chromium as well as aluminum and copper, iron, platinum, and rhodium and cover a range of temperatures from 270-3000 °C.

Thermoelectric devices can be used for power generation and cooling and are designed to fit each application. Commercial power conversion applications are enabled after the introduction of semiconductors as thermoelectric materials with conversion efficiencies in the range of 5-10%. Furthermore, reported power densities are rather low, which is another limitation for some weight sensitive applications. While these efficiencies are still very low in absolute terms, limited economic uses for niche applications are still feasible, where reliability outweighs the low conversion efficiencies. For power generation, thermoelectric generators have demonstrated their use in space applications [4], remote power along oil and gas pipelines [80] and body temperature powered watches[50]. TEGs are also used as a security backup power source to establish a defined state in emergency cases on offshore oil rigs and for seismic measurement, stations in earthquake prediction are as well as early remote communication gear; and as radio and TV relay stations [4]. Current prevailing applications for TEGs have come from waste-heat energy harvesting in vehicles. While

technological advancements in energy harvesting face equally difficult challenges as energy storage devices, advancements in research and engineering will provide increased efficiency and longer lifespans. Commercially available thermoelectric generators also have applications for waste heat recovery in processing combustible solid waste [81]. In addition, thermoelectric devices have been used for powering sensors from waste heat generated in nuclear plants [82].

In extreme situations, radioisotopes are used as a heat source. Strontium-90 (29 years half-life) has been used as a continuous power source for space applications. The most prominent application of radioisotope powered thermoelectric generators is as a power source for space vehicles such as satellites and research gear on several missions. Novel applications of TE materials include biothermal batteries to power heart pacemakers, enhanced performance of optoelectronics coupled with solid-state TE cooling, and power generation for deep-space probes via radioisotopic TE generators [1]. Recent applications include solar thermoelectric generators (STEGs), to concentrate solar energy to create heat that a TEG turns into electricity [83]. They use a wavelength-selective absorber typically inside a vacuum to provide hotter temperatures on the surface of the TEG, thereby maximizing device efficiency.

2.7 Summary

In this chapter, a brief overview of the three thermoelectric effects as well as their relationships is discussed. The thermoelectric figure of merit, as well as new thermoelectric materials, are presented. The operation of a thermoelectric device and different type of device configurations are discussed. Finally, the application of thermoelectric devices is also presented.

Chapter 3

Application of Thermal Spray for Thermoelectric Device Fabrication

In this chapter, the application of thermal spray for the fabrication of thermoelectric devices is presented. Thermal spray is a process used to apply metallic or nonmetallic coatings on surfaces. A major advantage of thermal spray processes is the extremely wide variety of materials that can be used to produce coatings [84]. Other advantages include of thermal spray processing include extremely high volumetric deposition rates, material flexibility, and moderate thermal input during processing, allowing for deposition on a variety of substrates. The materials requirements that need to be fulfilled for the insulating layers conducting layers and thermoelectric legs are described. Challenges encountered when attempting to fabricate a thermoelectric device using thermal spray are also presented. New solutions are proposed to overcome these challenges, which are verified experimentally.

3.1 Materials for Thermals Spray

Thermal spray is a process that accelerates material to high velocities and deposits them on a substrate as shown in Fig. 3-1. Based on the heat source and spray environment, thermal spray processes can be categorized into atmospheric plasma spray (APS), high velocity-oxy-fuel (HVOF), vacuum plasma spray (VPS), flame spraying and cold spraying among others. The microstructure properties of thermal spray coatings strongly depend on the processing parameters

utilized. The materials for thermal spray come in powder or wire form. Powders are typically 1-100 μm in diameter. When powders are sprayed on a substrate, splats of near-circular lamellae (10-100 μm in diameter and a few micrometers thick) flatten and solidify upon impact on the substrate forming a dense coating[34]. Each droplet cools at very high rates (>10^6 K/s for metals) to form uniform, fine-grained, polycrystalline coatings or deposits.

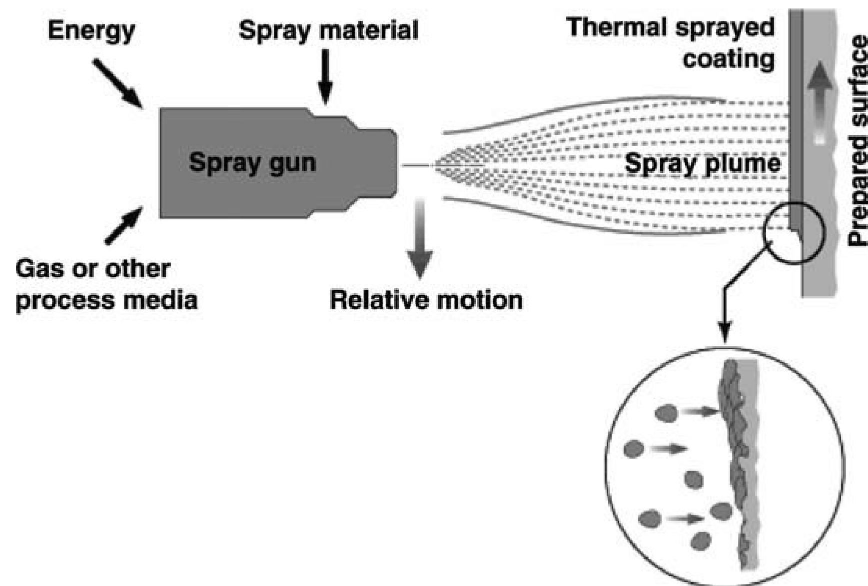

Fig. 3-1 General apparatus for thermal spray [85]

These coatings stack on top of each other creating a unique microstructure that is composed of splats, cracks, interfaces, and pores. A typical microstructure of thermal spray materials is shown in Fig 3-2.

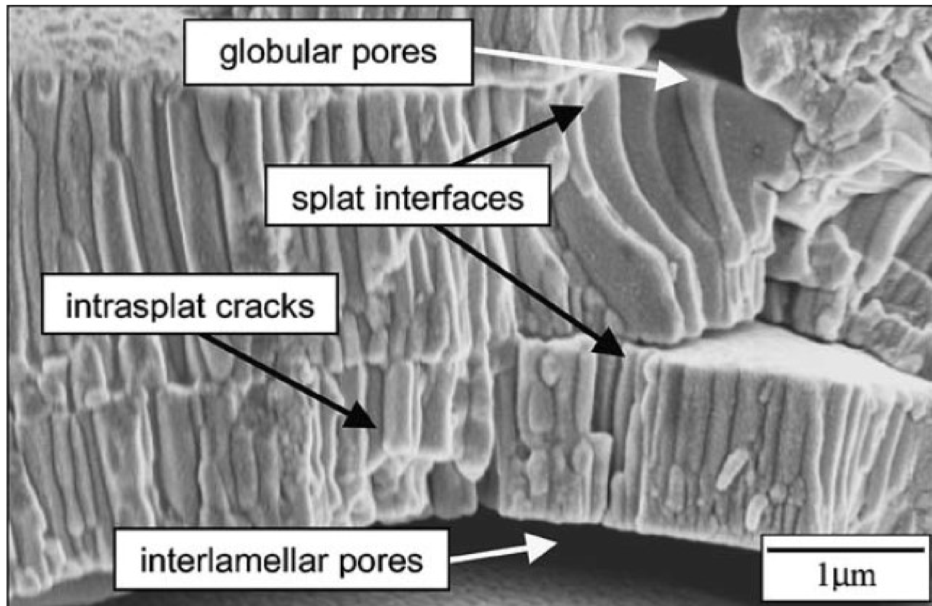

Fig. 3-2 SEM image showing detail of microstructural features[86]

Thermally sprayed coatings are known to be structurally complex due to the nature of the coating build-up process. The continuous impact of molten and semi-molten droplets during the spraying process produces an anisotropic layered arrangement of microstructural defects (pores, cracks, etc.) in the coating. This coating structure can have a significant effect on thermal transport properties. The coating is made even more heterogeneous because sprayed deposits usually contain some level of porosity, typically 0 and ~10%, some unmelted or partially melted particles, fully melted and deformed "splats," metastable phases, and oxidation from entrained air [34].

Thermal spray materials have reduced thermal conductivity due to their layered structure. While the difference depends on several factors, the properties of thermal spray materials are different from the bulk materials. Measurements of thermal conductivity of thermally sprayed coatings are common methods of material characterization. Table 3-1 shows a comparison of thermal conductivities of thermal spray materials compared to the bulk.

Table 3-1 Thermal conductivities [W/m·K] of thermal sprayed materials [86-88]

Material	Bulk Thermal Conductivity	Thermal Sprayed Thermal conductivity	
		Through-thickness	In-plane
Yttria-stabilized Zirconia (YSZ)	2.5	1.1–1.4	1.6–1.9
Molybdenum (Mo)	142	15	40
Nickel-Aluminum (NiAl)	80	11-22	15-29

Thermal spray can be used to create conductors for contacts, electrical connections, and heating elements [89]. Several different types of metals and alloys are routinely sprayed including aluminum, aluminum-zinc, copper, molybdenum, nickel-aluminum alloys, and nickel-chromium alloys for TE devices. Metals are required for the conducting interconnects. Typical conductivities of these sprayed metals are reported to be 40 to 90% of their wrought material counterparts, depending on the spray coating method used [34].

Thermally sprayed ceramic coatings are good protective coatings for abrasion and corrosion resistance. Ceramic coatings also provide good electrical insulation. Ceramic materials can be used as the insulating layers of TEG devices. Commonly sprayed ceramics coatings include alumina (Al_20_3), Yttria-stabilized Zirconia (YSZ) and Titania (TiO_2).

As described earlier, the *ZT* of a thermoelectric material is dependent on the crystal structure, phase, and microstructure and — for semiconductors — the doping level. Bismuth Telluride, which is the most commonly used TE material, is not feasible for the thermal spray process because it would result in the oxidation of the powders used, significantly changing its phase and degrading its thermoelectric properties. The cost of the Bismuth Telluride is also prohibitive for testing. Other powders considered suitable for thermal spraying (e.g. Mg_2Si) will not provide the expected ZT values without optimized spraying parameters and post heat treatment.

In light of these factors, metal powders are found to be the most suitable to demonstrate the feasibility of this manufacturing method. While the reduced thermal conductivity of thermal sprayed coatings may be advantageous for improved ZT, it is also essential to improve the electrical properties. For high-temperature processes like APS and HVOF, finding the right stoichiometric composition is very difficult. In general, using high purity powders and reducing oxidation are important. Another option is to spray metal alloys with slightly higher Seebeck coefficient than pure metals. These include Nickel and Ni alloys such as Ni-Al, Nichrome, and constantan.

One of the challenging issues with this project was the poor material performance parameters for the thermally sprayed thermoelectric materials. The proposed material was Mg_2Si. Three different spraying methods of spraying were tested. These were atmospheric plasma spray (APS), high-velocity oxy-fuel coating spray (HVOF) and vacuum plasma spray (VPS). The best TE performance was achieved using VPS. However, the performance were less than 30% of bulk reported values for Mg_2Si. In addition, limitations due to material cost and repeatability is a limiting factor in using this material. As a demonstration of the actual manufacturing process, we used thermocouple materials instead, which have reduced power output but reduced cost.

3.2 Fabrication of TE devices using Thermal Spray

The fabrication of TE devices using thermal spray involves material deposition and subtractive manufacturing. Figure 3-3 shows the steps used to fabricate a complete TEG on an exhaust pipe. First, blanket layers of insulating and conducting materials are thermally sprayed. Then the *n*- and *p*-type TE materials are deposited alternatively. Finally, a blanket layer of top conducting material is sprayed to complete the device.

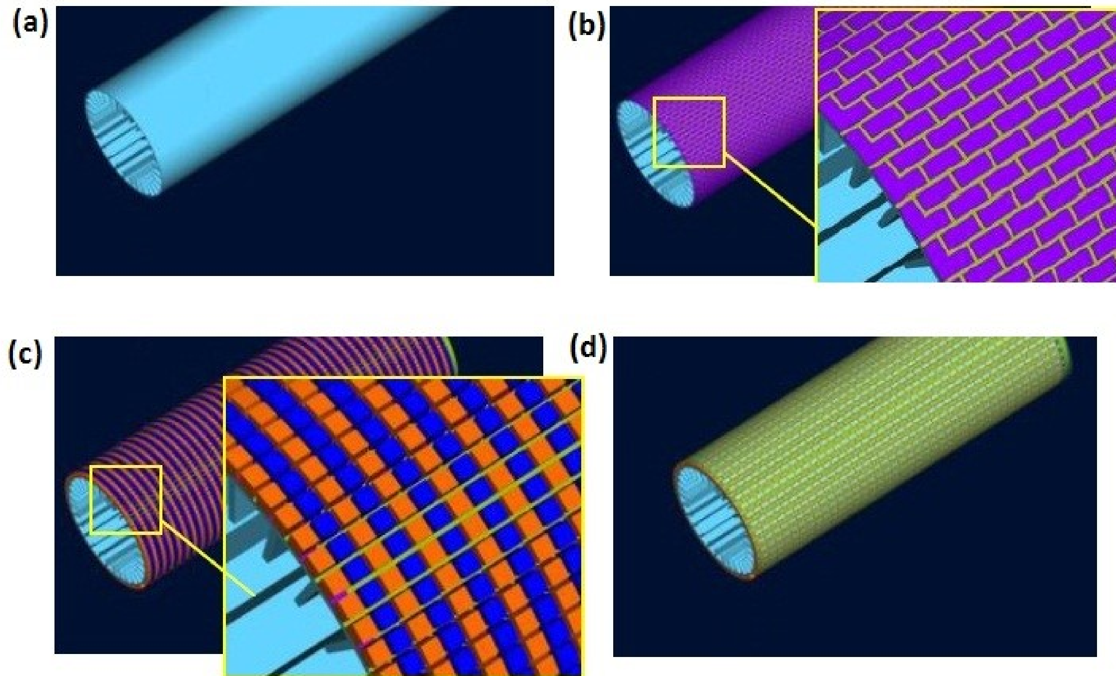

Fig. 3-3 Process steps to fabricate a TEG module (a) exhaust component with an integrated heat sink (b) apply bottom electrode and pattern, (c) deposit of n- and p-type TE legs, (d) fill the gap and deposit top electrode and top insulating layer.

The steps that are required present several unique challenges. Interfacial bonding of the sprayed material on the substrate is one key challenge. Insufficient bonding can result in the delamination of the coating from the substrate. Pre-treatment of the substrate using grit blasting is important. The choice of substrate and conducting material is also very critical for overall device performance.

If the materials used in the fabrication of the thermoelectric generator do not have comparable thermal expansion coefficients, residual stresses can develop at the joints, which can affect interfacial bonding. The diffusion layer between the two adjacent materials should be at least a few microns thick to ensure good contact and be stable when exposed to hot-side temperatures over time. This is also important in creating multilayer structures. One reason for delamination is thermal shock resistance caused by non-uniform heating/cooling as shown in Fig. 3-4. Rapid

quenching of the sprayed layer results in the layer contracting faster than the substrate; developing tension that results in delamination. As a result, the temperature differences are very important to determine if the stresses that develop are too large to cause delamination. When the total stress exceeds tensile strength, cracks can form. The stress developed, σ, is given by:

$$\sigma = -E\alpha_l(T_2 - T_1) \qquad \text{(Eq 3-1)}$$

where E is the Young's modulus, α_l is the thermal expansion coefficient, T_1 is the temperature of the substrate and T_2 is the temperature of the sprayed layer. The temperature difference depends on the material types sprayed as well as the thickness of the layers. Therefore, material combinations need to be optimized experimentally to obtain well-bonded layers. Several material combinations must be tested to determine which will adhere to each other. Thermal expansion coefficient mismatch and residual stress must thus be matched to reduce cracking of coatings leading to delamination.

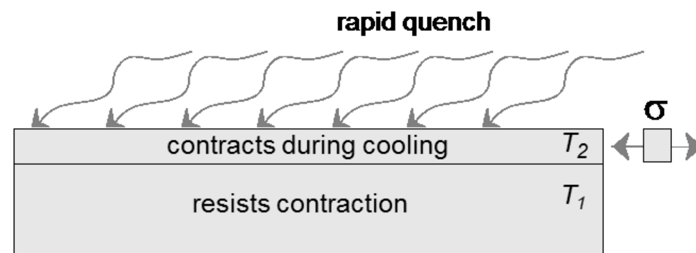

Fig. 3-4 Stress developed due to non-uniform cooling of thermal spray layer

To prepare the multi-layered structure, bulk alumina substrates are uniformly sprayed with a copper layer. This resulted in the copper film peeling off, demonstrating that directly spraying copper onto an alumina substrate results in poor adhesion (Fig. 3-5). Differential thermal expansion at the joints between dissimilar materials can result in stresses that can easily exceed the maximum stress of the thermoelectric material. To improve the interfacial bonding between the

two layers, aluminum substrates were also tested. This layer is first sprayed with a ceramic coating before the copper layer is applied. It was found that this significantly improved the bonding between the copper layer and the substrate. In automotive thermoelectric applications, thermal gradient, thermal cycling, and vibration will impose stress on the thermoelectric materials. Therefore, adhesion between different layers is a very important issue for long-term, reliable TEG performance.

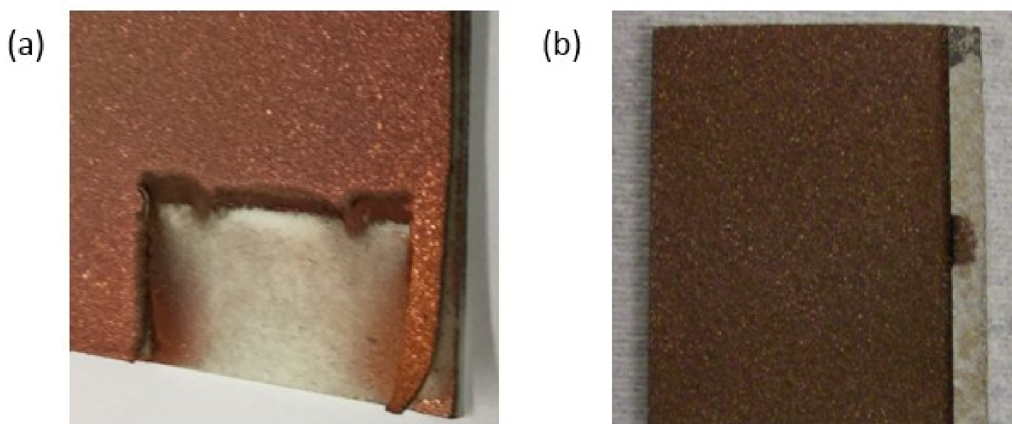

Fig. 3-5 (a) copper sprayed on alumina wafer (b) copper and alumina sprayed on aluminum wafer

Spraying TE legs requires spraying targeted regions of the substrate with specific types of material, i.e. the ability to selectively spray specific areas of a substrate or protect component areas next to the target zone from impact by overspray particles. Masking techniques are available including paint on masking compounds, metal masks, and high-temperature tapes.

Masking compounds are useful for providing short-term protection from overspray although they are not useful for protection from grit blasting. Available compounds include refractory particles such as graphite, carried in water- or solvent-soluble binders and applied by brushing or spraying. Residual compounds are easily removed by rinsing with water or solvents depending on

the carrier solubility. Masking compounds are easy and convenient to use despite their shortcomings. When dry, the film prevents material from sticking. While the refractory particles provide short-term heat protection, excessive exposure to the spray stream will cause these compounds to break down, causing the spray particles to stick. Since the TE legs are thick and thus require prolonged spray times, this method is not suitable for device production.

Tape masks are applied by wrapping areas that do not require a coating. After spraying, accumulated material is removed along with the tape, leaving the protected areas. Each part needs to have tape applied. Many different tapes are available commercially for thermal spraying. The best tapes have sufficient toughness to resist both grit blasting as well as heat resistance to withstand the hot gas and particle impact during spraying. The coating line when the tape is removed after the application of thin coatings leaves a neat and clean edge, but if the coating is thick, chipping is likely to result.

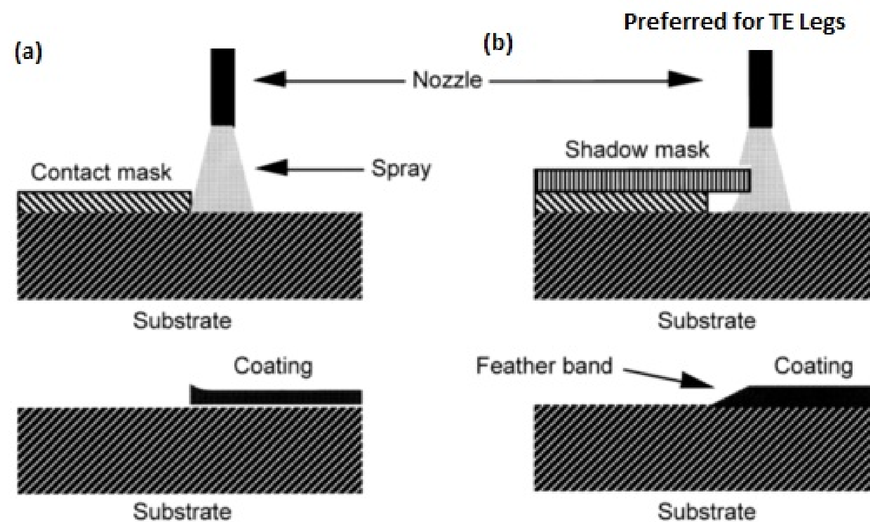

Fig. 3-6 Coatings resulting from (a) contact masks (b) versus shadow masks [34]

Contact masks are placed directly on the part to be sprayed, shielding selected areas from the spray deposit (Fig. 3-6a). Metal shadow masks can be placed on top of the part to be sprayed

or in front of the spray torch (Fig. 3-6b). The target spray area may be stationary or rotating. As the spray stream traverses across the target area through the mask, the unwanted spray is prevented from reaching the substrate collecting on the mask. Contact masks leave a sharp edge, which may act as a stress raiser that leads to debonding of the coating. Shadow masks, on the other hand, placed approximately two to three times the total coating thickness away from the part results in a narrow feathered band rather than a sharply defined line (Fig. 3-6b). The advantage of metal contact or shadow masks is that they can repeatedly be used, subject only to the amount of spray buildup and/or distortion due to heat from the spray process. Complex patterns can be manufactured once and be used to fabricate multiple components. Sheet metal masks are also preferred for HVOF spraying because tapes do not stand up to high-velocity particle impact.

To determine the optimum mask parameters to spray the TE legs, different size holes were made in a 3.1 mm thick aluminum coupon with tapered holes machined to test various offset distances as shown in Fig 3-7. The hole dimensions are square and vary in size from 2 mm to 6 mm. Fig. 3-8 shows the results after spraying on different masking holes with different offset distance.

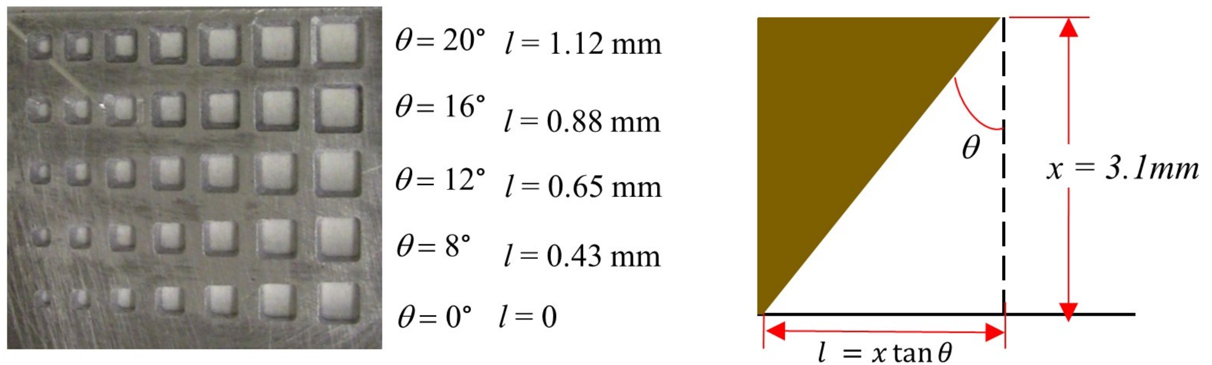

Fig. 3-7 Mask fabricated from Aluminum to test various offset distances

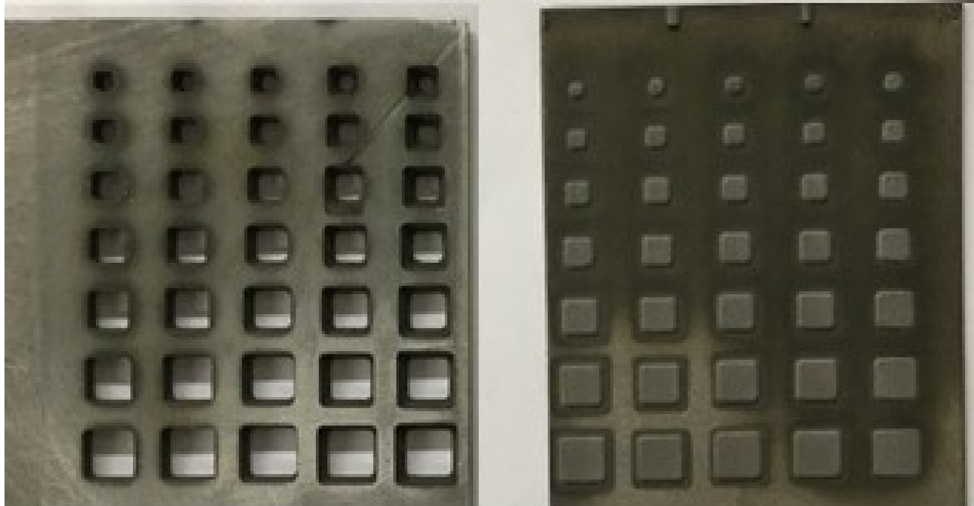

Fig. 3-8 Demonstration of high aspect ratio spraying of TE legs

Figure 3-9 shows the sprayed leg thickness and leg width for 2 mm square holes. The leg thickness increases with increasing offset distance (taper angle) to a maximum value of the spray thickness. The width of the leg decreases with increasing offset distance (taper angle). Based on this finding, an offset distance of 0.8 mm was determined to be the optimal value for full thickness and high aspect ratio. This corresponds to a taper of angle ~15° for a 3.1 mm thick mask.

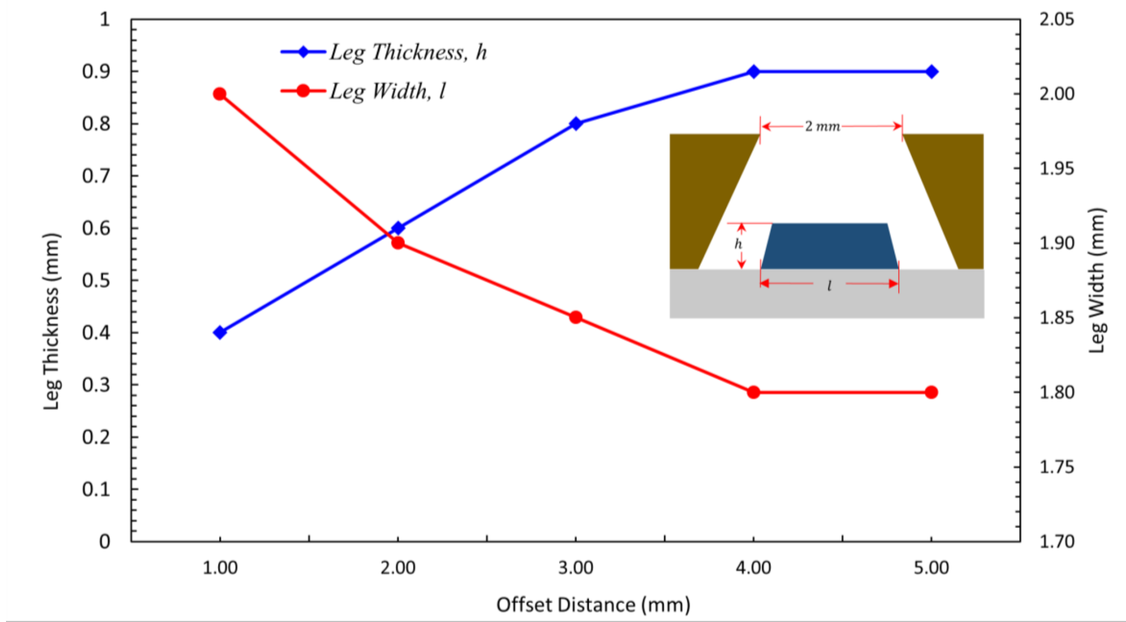

Fig. 3-9 Leg thickness and leg width of sprayed legs vs. offset distance

The final challenge is to spray a copper layer over the TE elements while maintaining a gap between the legs. This layer provides an electrical path across two adjacent *p*- and *n*-type legs. A permanent filler material could be introduced into the gaps to act as a bridge when the top conducting layer is sprayed. However, this would reduce the performance of the TE device as the filler material would lead to a higher parasitic heat loss and a reduction of electrical power. Since air is an excellent thermal insulator compared to a filler material, an alternative is to use a temporary filler material that can be removed after the top conducting layer has been deposited. A temporary filler must survive the thermal spray process while also being easy to remove after the thermal spray is complete.

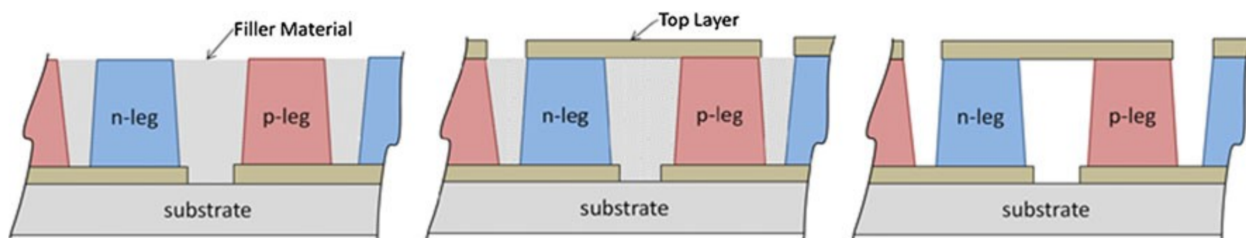

Fig. 3-10 Proposed gap filling procedure (left) Air gap filled with sand/glue mixture and allowed to dry, (center) top conducting layer sprayed after mixture dries, (right) sample baked at elevated temperature to remove filler, leaving air gap

Some materials that can be used include silica sand (SiO_2), bentonite clay, gypsum, silicate bond, low-temperature alloys and water-soluble polymers. The best materials are powders carried in water- or solvent-soluble binders that can be dissolved or burned out after spraying the top coating. Several materials are explored as a binder. Based on the temperatures experienced in the thermal spray process, Polyvinyl alcohol (PVA or white glue) (SoapGoods.com, Smyrna, GA, USA) is found to work the best. PVA is water-soluble and has a density of 1.3 g.cc. PVA has a number of useful and tailorable properties – it is odorless and non-toxic, and it has excellent film forming, emulsifying, and adhesive properties [90]. It is mixed with fine sand to provide support

and high-temperature tolerance for the thermal spray process, while the PVA acts as a binder for the sand that can be removed by heating. PVA decomposes to a black powder at 400 °C. It can be easily removed after it decomposes but is stable to withstand the thermal spraying process. Just enough glue can be used to hold the sand in place when dry. Referring to Fig. 3-10, the mixture is squeegeed into the grooves and allowed to dry, followed by spraying of the top Cu conducting layer. The sample can then be placed in an oven to burn out the glue, after which the sand is removed by gently tapping the part.

To evaluate techniques for the gap bridging required to deposit the top conducting layer, a 50 mm x 50 mm x 6.35-mm aluminum block was machined with grooves of different widths to simulate the air gap between TE elements (Fig. 3-11). A mixture of fine white sand and water-soluble polyvinyl alcohol (PVA) was squeegeed into the grooves and allowed to dry overnight (Fig. 3-11, left). Next, a 0.7-mm top conducting NiCr layer was sprayed over the elements and the filled gaps. After this layer had been sprayed, the sacrificial sand/PVAmaterial was removed by placing the sample in an oven at 400 °C for 20 min to burn out the PVA. The loose sand is then easily removed from the grooves. The results are shown in Fig. 3-10 (right). Thin strips of white paper are passed through the grooves through the entire length of the Aluminum block, indicating that the channels have no solid material in them.

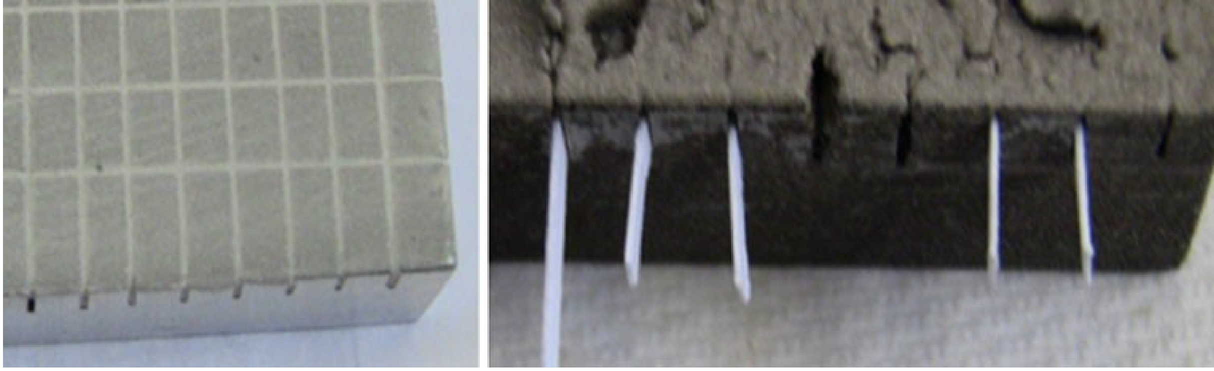

Fig. 3-11 (left) Al block with machined grooves filled with PVA/sand mixture to demonstrate gap filling (right) Sample after deposition of 0.7-mm NiCr and bake-out of filler material at 400 °C

3.3 Summary

In this chapter, the feasibility of thermal spray as a means of fabrication for TE materials and devices has been investigated. Thermally sprayed materials are well suited for fabricating the insulating and conducting layers of a TEG, but have poor thermoelectric performance. In this work we have presented progress towards developing an integrated, one-step process to fabricate thermoelectric materials, bonding materials, and electrical contacts using ink-dispensed laser sintering. Preliminary results have also been presented. It is anticipated that this approach will largely resolve the interface, durability, and heat transfer issues prevalent with the conventional approach of integrating pre-fabricated TE modules onto exhaust components. This fabrication method eliminates the need for soldering, gluing/epoxying, and mechanical pressure joining which significantly simplifies the device fabrication process while reducing cost and improving reliability. Further work is required to optimize the process, explore additional potential filling materials, and obtain high-quality coatings.

Chapter 4

Subtractive Manufacturing Techniques for Thermoelectric Device Fabrication

Subtractive manufacturing (SM) is a traditional form of manufacturing process that involves the controlled material removal from a piece of raw material into a desired final shape. There are many different kinds of SM methods used in the manufacturing industry. When manufacturing prototypes, the major factors in choosing the manufacturing method are *cost*, *lead times*, *material selection* and *quantity*. While AM methods can produce highly complicated prototype designs difficult to replicate by SM, material selections and strength of the finished parts may be limited. In this context, additive and subtractive methods may be compared with each other. However, in the larger context of manufacturing as a whole, they are taken to be complementary. At present, while AM is best suited for prototyping, SM is still the preferred method for parts requiring a high degree of precision or parts that have a highly specialized function. In addition, SM is well suited for high volume manufacturing of the same parts without changes, and for parts with a simple design.

In this chapter, the role of SM techniques in thermoelectric device fabrication is briefly reviewed. The respective advantages and disadvantages of each method are also evaluated. Laser processing, as a candidate for high speed, high accuracy SM technique, is discussed in detail. A detailed investigation of the role of laser micromachining in processing thermal sprayed films is

of particular interest. This is because thermal spray films have unique properties that differentiate them from their bulk counterparts. Therefore, laser processing of thick or thin thermal sprayed films is essential to the optimization of the device fabrication process. In this regard, the feasibility of laser micromachining as a superior SM technique for thermal spray materials is presented.

4.1 SM Methods for Thermoelectrics

Subtractive manufacturing processes can be categorized as mechanical, thermal-electric or chemical based on the type of energy used for the material removal process [10]. The general types of each process are shown in Fig. 4-1. Selected machining processes are discussed in regards to their application to thermoelectric material and device fabrication. The advantages and disadvantages of the machining process are also discussed in detail.

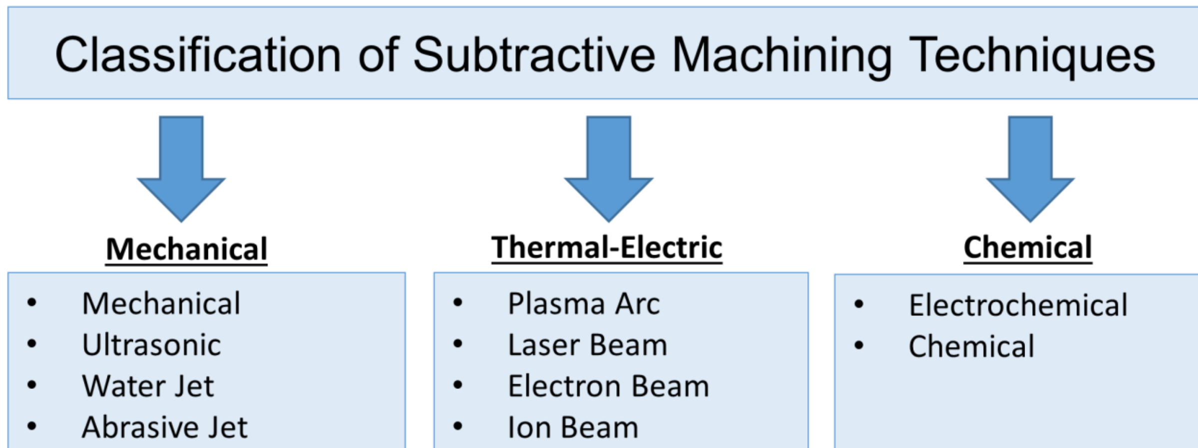

Fig. 4-1 Classification of Subtractive Machining Techniques

4.1.1 Mechanical Material Removal

Mechanical material removal, also known as *machining*, is a process in which a raw material is cut into a desired shape and size by a controlled material removal process using mechanical force through plastic or brittle damage. In general, these methods include any process that makes use of machine tools (hand tools or power tools), water jets, ultrasonic, abrasive jet, etc. It is widely used

to manufacture many metal parts but is also suitable for materials such as wood, plastic, ceramic, and composites.

Micro-machining is the use of machining to fabricate parts with micron or sub-micron level precision and accuracies In micro- machining operations, a highly concentrated force is applied in a small area of the workpiece resulting in elastic/plastic deformation and fracture with high strain rates and temperature for which material properties vary during the process. In addition, when the tool dimension or a feature to be generated is of the same order as the grain size, or where material cannot be treated as isotropic and homogeneous, the cutting mechanism differs substantially from conventional machining [91].

Cutting-tool-based machining is the most common type of machining operations such as milling, turning, drilling, boring, etc., combined to form a variety of shapes and sizes. Milling produces parts that are not axially symmetric, such as holes, slots, pockets, and even three-dimensional surface contours. Drilling is used to cut a hole into a workpiece. Turning produces rotational parts with features such as holes, grooves, threads, tapers, various diameter steps, and contoured surfaces. At present, all of these machining operations are controlled by what is known as computer numerical control (CNC) machining. Limitations of cutting-tool-based micromachining include the cutting tool material, size and the type of workpiece. Commercially-available micro-drills are typically on the order of 50 μm in diameter [91]. One example of micromachining is wire saw cutting in order to shape crystals and has emerged as a leading technology for wafer production in the semiconductor and photovoltaic industry. It can cut very thin wafers from large diameter crystalline ingots and bars of semiconductor materials. In the wire saw, a single strand of thin wire (~100 μm in diameter) moves from a feed reel to a take-up reel. The wire wraps around wire guides

that have multiple nets to create a wire web. The ingot crystal is fed together with an abrasive slurry to produce a cut. It can also be used to dice wafers into rectangular shapes. Wire saws have a kerf loss of 200-300 μm per cut with yields of up to 30 wafers per inch. Wire saw cutting is also used widely for TE device fabrication. Hot pressed ingots of semiconducting thermoelectric materials can be cut to the required shapes, and size dies [92, 93]. Other techniques like ultrasonic, water jet and abrasive jet methods are not well suited for micromachining [94].

4.1.2 Thermal-Electric Methods

Thermal-electric methods use energy supplied by heat (plasma arc), light (laser beam) or electrons (electron beam) for controlled material removal. The general procedure is to concentrate the energy onto a small area of a workpiece to melt, vaporize or ablate material for removal. Generally, the mechanical properties of the workpiece do not influence the machining process because temperatures generated by an electrical discharge, a laser beam or an electron beam can easily exceed the boiling point of any known materials. In contrast, thermal properties such as melting point, boiling point, thermal diffusivity and heat capacitance significantly influence machining characteristics.

The three main types of thermal-electric machining methods include plasma, laser and electron beam. Plasma cutting uses a plasma torch to cut materials. While it is economical, it is very rough and not suitable for micromachining applications. Laser beam machining (LBM) is based on material removal by heating and vaporization of a workpiece exposed to laser radiation. When the incident power density on the workpiece is extremely high, direct removal of material by vaporization or sublimation occurs, skipping the melting phase entirely. Melt cutting by using non-reactive gasses or oxygen assisted (chemical reaction enhanced) processes are also commonly

used. However, finding suitable laser parameters is necessary before machining. Electron beam machining (EBM) is a process where high-velocity electrons are concentrated into a narrow beam and directed toward the workpiece, creating heat and vaporizing the material. They are scalable processes and suited for materials which are hard to machine, such as ceramics. Electron beams have longer penetration depths than laser beams. LBM and EBM can be finely tuned to process materials accurately. They are also good for making very fine cuts and holes in difficult to machine materials [93-95]. In addition, surface finish qualities are improved compared to other methods.

4.1.3 Chemical Methods

Chemical machining involves the material removal by chemical action without any force acting on the surface. A strong acidic or alkaline chemical reagent is used for the controlled etching of the machined workpiece, where the parts to be machined are immersed in a tank containing etching solutions without electrical assistance. Electrochemical dissolution in a liquid solution is also utilized. In this type of process, the removal mechanism is based on an ionic reaction on the work-piece surface. The selective machining applications ensure that special coatings and masks protect the remaining areas. Chemical etching processes have a narrow range of application and require a suitable material-enchant match. Chemical etching finds applications in TEG device fabrication especially for micro-devices [96, 97].

4.1.4 Evaluation of SM Methods for Thermoelectrics

The above-listed SM methods can be evaluated based on their advantages and disadvantages and are summarized in Table 4-1. While mechanical machining offers a low-cost method for processing the TE materials, it is not well suited for multi-layered and thin structures since it produces considerable stress on the machined parts. Chemical methods are attractive for their precise capabilities, but have very low material removal rates (MRR) and require finding a suitable match of

materials for the etchant. LBM/EBM stand out as a cost-effective solution for machining a wide range of materials for scaling and industrialization. One remarkable advantage is that the machining force on the workpiece is negligible, and the molten material can be removed without affecting the workpiece. A drawback is an uncertainty in specifying the dimensions of the workpiece since the tool does not contact the workpiece mechanically. Moreover, in LBM and EBM, the outline of the tool (shaped beam) itself is not exactly clear. Another drawback is the formation of a heat-affected layer on the machined surface. Since it is impossible to remove all of the molten material from the workpiece, a thin layer of molten material often remains on the workpiece surface, which resolidifies upon cooling. The immediate inner layer of the workpiece is not melted, but heating changes its structure. The presence of such a layer may cause problems when the product is in use. The surface after machining is free from any damage, residual stress or heat effects.

Table 4-1 Comparison of SM Methods Available for Thermoelectric Devices

SM Method	Advantages	Disadvantages
Mechanical	• High stresses on part • Not suitable for micromachining tiny features (<1 mm) • Good tolerance • Short lead times • Uniform surfaces	• Limited shape complexity • High equipment cost (e.g., abrasives and slurry base), • Significant tool wear • Large amount of scrap • Part may require several operations and machines
LBM/EBM	• Versatile • machine fine features • contact-free	• Limited penetration depth for metals • Needs optimization
Chemical Etching	• No stress or affected zone • Simple to implement • Cheap • No additional cleaning step needed	• Wet process • Hazardous chemicals • Limited material-enchant matches

4.2 Laser Micromachining (LMM)

Laser radiation is monochromatic, coherent, easily collimated and focused light. Lasers are available up to very high intensities ($\geq 10^{20}$ W/cm^2) making them well suited for processing a wide range of materials (metals, glass, ceramics and plastics and composites). For example, laser cutting a 10 μm wide groove on copper is shown in Fig 4-2. A typical laser machining system consists of a laser source, a movable stage for work-piece or a scanning mirror and a computer control for synchronizing the beam with the workpiece. In this work, the application of lasers in the machining of multi-layered thermal spray films is studied experimentally.

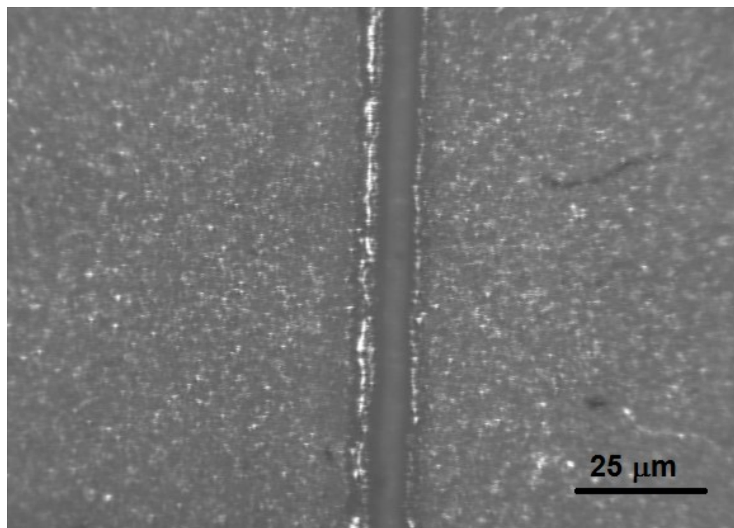

Fig. 4-2 Laser patterning of copper

4.2.1 Laser Choice

There is a wide range of laser sources spanning the far infrared (IR) to UV spectrum used for laser processing operations. Common lasers include CO_2 lasers, argon lasers, Nd:YAG, Nd:YLF lasers and high power diode-pumped solid-state (DPSS) lasers to handle a wide range of material types. The laser source chosen determines the wavelength and highest laser irradiance available. When low to moderate intensity lasers are used, the absorption property of the material is important. For higher intensities, the choice of laser is more flexible. The MRR is primarily

dependent on laser intensity. The choice of laser, therefore, depends on the laser power required, cost and availability [98]. Pulsed lasers, where power is delivered in pulses, are preferred over continuous wave (CW) lasers for machining operations due to their high intensities. The optimum pulse duration for a laser in a material operation depends on the target material [98]. The appropriate selection of laser irradiance and the duration of the interaction are critical to the application considered. The ranges of laser irradiance for which individual processes dominate the interaction are summarized in Fig. 4-3.

Laser machining is caused by material *ablation* in which laser energy in excess of the binding energy directly decomposes and removes the atoms from the workpiece. Therefore, higher intensity corresponds to a faster ablation rate. The ablation of thick films has a wide range of industrial applications. The most important parameters to consider when choosing a laser are the wavelength, pulse duration, pulse repetition rate and beam quality [99]. The wavelength should be chosen to minimize the optical penetration depth (α^{-1}) and to achieve high energy density in a small volume for rapid and complete ablation. A short pulse duration laser is preferred to maximize peak power and to minimize the thermal penetration depth. The repetition rate of the laser should also be optimized. If the repetition rate is too low, some of the energy not used for ablation will leave the ablation zone allowing cooling. If the residual heat can be retained, thus limiting the time for conduction, by a rapid pulse repetition rate, the ablation will be more efficient. More of the incident energy will go toward ablation, and less will be lost to the surrounding work material and the environment. Finally, the beam quality determines the homogeneity and ease of focusing the laser beam for efficient delivery to the workpiece. The beam quality also determines the size and quality of the machined parts. The choice of laser also depends on the cost of the system.

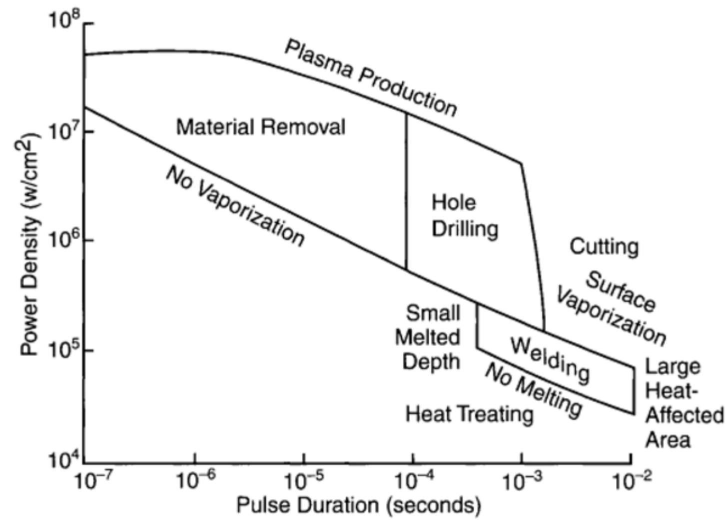

Fig. 4-3 Laser irradiance and interaction time for material processing applications [98]

Table 4-2 Choice of available lasers

Manufacturer	Yuco Optics	Yuco Optics	Photonics Industries
Model No.	FW-150	FW-40	GM-30
Wavelength (nm)	1064	532	527
Maximum Power (W)	20	10	20
Pulse Width	30-50 ns	20-50 ns	250 ns
Repetition Rate (kHz)	0-100	0-100	0-10

The lasers investigated in this work are short-pulsed lasers in the visible and near-IR range. They represent the most common lasers used for micromachining and patterning operations commercially. The lasers used along with their main parameters are given in Table 4-2.

4.2.2 Experimental Setup

An overall schematic of the laser micromachining system used for processing of the thermal spray coatings is shown in Fig. 4-4. The GM-30 laser is an arc-lamp-pumped Nd:YLF laser with 20 W power output. It has a 0-10 KHz repetition rate and a uniformly distributed beam profile. The FW-150 and FW-40 lasers are diode-pumped Nd:YAG lasers with 20 W and 10 W power output, respectively. They both have a variable pulse repetition rate of up to a 100 kHz.

Two motion control setups are used for the GM-30 laser – a linear stage for processing flat samples and a rotary stage for processing cylindrical samples. Linear motion control is achieved by assembling three translation stages (*Coherent LabMotion*) on a rigid post. The stages are oriented mutually perpendicular to each other along *x*, *y*, and *z* directions to move the sample as needed and control the laser beam delivery. Each stage has a resolution of 0.5µm and a motion range of 50 mm. The rotary stage consists of a single high precision, high-speed rotation stage (Micos, DT-120-DC) that is controlled through a nuDrive multi-axis power amplifier (4CX-001) and a National Instrument motion controller (PCI-7344). The motion control system can be programmed to control the laser beam delivery and execute a preprogrammed motion profile. The rotary stage has a maximum speed of 8000 rpm. The GM-30 laser power is adjusted by changing the pump current and monitoring the laser power. The laser beam is controlled by an external signal from the motion controller. The beam diameter of the green laser is larger than the infrared laser, hence, a plano-convex lens of focal length f =50mm were used.

The motion control stage for the FW-150 and FW-40 lasers consists of two high-resolution *x-y* stages controlled through an Aerotech motion controller. The beam focus is controlled by adjusting the lens position in reference to the sample surface to get a clear focus on the surface. Each stage has a resolution of 100 nm and a motion range of 10 mm. Inert gasses (nitrogen, helium, argon and compressed air) are also available for use as purge gasses during laser processing to improve the machined feature quality and can be used as desired during the processing. The setup for the FW-150 and RGH-20 laser consists of a half-wave plate and a polarizing beam splitter to attenuate the power level as needed. The laser PRR can also be adjusted internally through the Q-switch. The beam delivery is controlled by a 150 Hz fast electronic shutter (*Newport*), and the beam is focused by a plano-convex lens of focal length f =100mm. In order to investigate the effect

of purge gas on the cutting process, different types of assist gasses (Nitrogen, carbon dioxide, argon, helium and compressed air) were used and investigated.

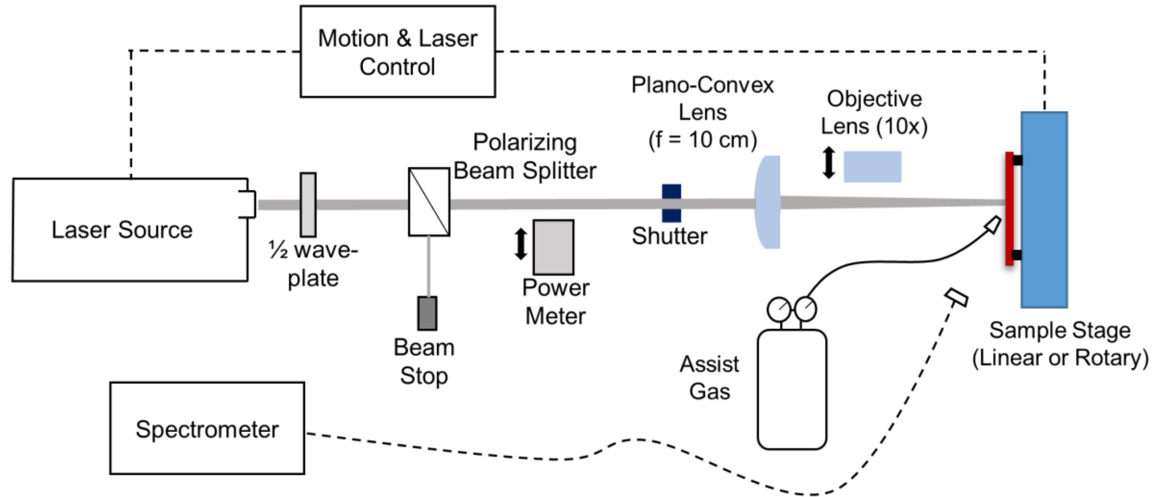

Fig. 4-4 Typical laser machining setup

The power measurements at the laser wavelength were performed with an LM-45 power meter (*Coherent Inc.*, US), which is capable of measuring laser powers from a few mW to 30W. The accuracy of the power meter was quoted to be ~2% in a spectral range of 0.25-10.6 μm. The power meter measures the average power and cannot directly measure the energy of individual pulses. The pulse energy can be calculated by dividing the average power measured by the repetition rate of the laser. For pulsed lasers, since the laser radiation comes in a series of pulses, the intensity is used to describe the power delivered per unit area by a single pulse (i.e., peak power (W) / focal spot area (cm^2)). The peak power is the energy of each pulse per unit time (i.e., pulse energy (J) / pulse duration (sec)). Similarly, the fluence (J/cm^2) is defined as the energy delivered per unit area of each pulse (laser pulse energy (J) / focal spot area (cm^2)). In all the experiments presented in this work, the incident pulse energies were measured after the microscope objective, taking into account the transmission and reflection losses of all the optics.

4.2.3 Characterization Methods

The surface morphology of laser-processed samples was studied with scanning electron microscopy (SEM) and optical microscopy (OM). OM images were taken with a MEIJI microscope (*Meiji Techno Co., Ltd*., Japan) of different magnifications (20x, 40x, 60x, 100x) and an MU1403 CCD camera (*AmScope,* US). In most cases, OM images are sufficient for characterization of ablation-induced damages, such as measuring damage and ablation threshold, etch depth/diameter and ablation. For a more detailed investigation of processed samples, SEM images are used.

Two types of in-situ monitoring techniques are also utilized. The first method uses a CCD camera to view the substrate while being processed. For multi-layer samples, a spectroscope is used to indicate when the sample has been completely removed. This is a commonly employed laser-induced breakdown spectroscopy (LIBS) technique [100], where the elemental composition of the ablated materials can be determined by measuring the emission from the sample with a high-resolution spectrometer. Once the spectrometer detects the material in the bottom layer, the laser is stopped. In this way, line patterning to the bottom surface of the top layer can be realized. It can considerably improve the laser machining efficiency and feature quality.

4.2.4 Materials

The Center for Thermal Spray Research (*CSTR*) at Stony Brook University provided the thermal spray blanket coatings and multilayer structures for this work. The samples surface were not polished and had surface defects, impurities, oxides, and adsorbates (as in many practical cases of materials processing). All the samples provided were sprayed using APS. In addition, bulk copper samples were also used to determine the effect of thermal spray microstructure on the laser parameters.

4.2.5 Spot Size Determination

For a Gaussian beam, the spatial fluence profile, $\phi(r)$, is given by:

$$\phi(r) = \phi_0 e^{-\frac{2r^2}{\omega_0^2}} \qquad \text{(Eq. 4-1)}$$

where r is the distance from the beam center and the laser-dependent Gaussian beam radius, ω_0 ($1/e^2$ criterion), and ϕ_0 is the peak fluence which is directly related to the pulse energy, E_p by:

$$\phi_0 = \frac{2E_p}{\pi\omega_0^2} \qquad \text{(Eq. 4-2)}$$

Assuming no aberrations, the diffraction-limited minimum focus spot size, hence the maximum fluence, of a focused laser beam can be estimated from the beam profile. The beam profile is related to the beam size and depth of focus through the beam quality factor, M^2. A beam with a Gaussian profile has a beam quality factor of $M^2 = 1$. For a given numerical aperture NA, and a wavelength of λ, the beam diameter at the focus can be expressed as:

$$d_f = \frac{2\lambda}{\pi}\frac{M^2}{NA} \qquad \text{(Eq. 4-3)}$$

where the beam has filled the lens aperture ($1/e^2$ criterion) [101]. The accuracy of fluence determination largely depends on the measurements of the spot size on the sample surface. One method is to measure the spot size directly with a CCD beam profiler. This method is limited to large beam sizes since typical CCD pixel sizes are limited to a range of 20 µm. Another method to determine the spot size of a focused beam is using the knife-edge technique [102], where a knife-edge is scanned through the focus of the beam and the transmitted signal is measured as a function of the lateral coordinate of the knife-edge. However, to ensure a good result, the plane of the knife-edge

scan has to coincide with the sample surface. It is also possible to estimate the focus spot size from the experimental data when measuring material ablation thresholds through the dimensions of the ablation crater [103].

4.2.6 Ablation Threshold Measurements

Damage threshold fluence (ϕ_{th}), is the minimum fluence at which any visible damage (but not removal) of the target surface appears [104]. The ablation threshold is an important parameter in laser processing because it defines minimal energetic requirements of a laser. Assuming a beam with Gaussian spatial intensity, the square of the ablated crater diameter, D^2, is given by:

$$D^2 = 2\omega_0^2 \, ln\left(\frac{\phi_0}{\phi_{th}}\right) \qquad \text{(Eq. 4-4)}$$

where ϕ_{th} is the material dependent surface damage threshold fluence and ϕ_0 is the peak fluence in the beam[103]. Because of the linear dependence of the peak laser fluence on the pulse energy, it is possible to determine the beam radius, ω_0, from a plot of D^2 versus the laser pulse energy, E_p. Once the beam radius is determined, the ablation threshold fluence, (ϕ_{th}), can be obtained by extrapolation.

4.2.7 Ablation Rate Measurement

The material removal rate (mm^3/s), i.e., the volume of material ablated per unit time and the ablation efficiency (mm^3/mJ), which is the volume of material ablated per unit energy are determined for copper. They were evaluated by milling rectangular holes with a lateral dimension of 0.5×0.5 mm^2 at different laser power settings. The number of pulses, scanning speed, the spacing distance between scans and the number of scans were kept constant. The depth of the holes ablated was measured and used to evaluate the ablation rate.

4.2.8 Optimal laser processing parameters

Thermal spray films are relatively thick (>100 μm) compared to typical thin-film processing applications, which are less than a few μm, commonly found in laser processing applications. This presents three challenges. The first challenge is maintaining electrical isolation across several layers due to the structure of the TEG. Second, since more *p*-*n* junctions mean higher added voltage, high processing speeds are necessary for long electrical isolation processing paths. Therefore, the laser processing conditions require fast material removal rates. Finally, the control of the sidewall profile by minimizing recast, which can electrically short two adjacent regions, is critical.

Another aspect of laser processing thermal sprayed coatings for TEGs is that it is necessary to maintain electrical isolation across several layers. This includes the need to maintain isolation between the bottom electrode layer and active thermoelectric material layers. The need to minimize material loss and maximize electrical power necessitate the requirement of narrow electrical isolation lines for higher TEG efficiency by minimizing the dead zone (non-active region). Therefore, the use of the usual laser machining line width at laser focal spot size (~10–100 μm) is challenging since it corresponds to a high aspect ratio for thick thermal spray coatings (> 0.3 mm).

The adhesion between thick multilayer coatings is also critical for the operation of the TEG. Traditional machining methods like milling and grinding are impractical. The high residual stress and weak adhesion nature of thick thermal sprayed coatings mean that laser ablation induced shock should be minimized to avoid delamination near the line edges. Thermal damage and heat diffusion effects need to be minimized to prevent delamination of the coatings.

A final practical requirement is to use one single laser source for all processing operations. This requires selecting the parameters for a laser system that can perform these three operations in

a single system. The selection of an appropriate laser system and associated parameters is essential for reducing processing times and improving feature quality, especially when features are small and it is necessary to protect sample integrity. Key features required include minimizing the heat-affected zone (HAZ), maintaining consistent material removal and to avoid forming large depth variations and high throughput.

4.3 Thermal Modeling

Thermal modeling of ablation is useful in order to estimate some of the general micromachining process parameters. Simple analytical models provide an approximate understanding of the process parameters and mechanism. The primary purpose of modeling is to solve for the temperature profile, ablation depth and ablation efficiency. These parameters coupled with experimental results are useful for optimizing the laser processing parameters [105]. Despite this apparent diversity in both the lasers and the material types, thermal models for laser ablation share many common features. For nanosecond or longer pulse durations, thermal transport is based on Fourier's law. Models for shorter pulses the need to account for the separate contributions from both electrons and phonons.

The simplest models to solve are thermal models that do not involve the dynamics of the melting and vaporization or plasma plume expansion. Such models can be used to determine the temperature distribution of a laser source, moving or stationary, on a substrate and provide insight into cooling times and heating times of interest. Numerical methods are required to solve the hydrodynamic and plasma effects. Numerical methods have several advantages over analytical methods because the heat source does not have to be concentrated in a point, line or plane. Temperature-dependent thermo-physical properties and real boundary conditions can be included, and

effects such as phase change and melt expulsion as well as plasma shielding can be accounted for. Despite these advantages, however, only a few numerical models for heat flow in laser processing have been developed so far. This is partly because of the complexity of building these models and partly because it is difficult to extract useful trends. An analytical solution, for example, would show that the temperature of a surface is proportional to 1/√time. This would not be so apparent from a numerical solution, which is specific for a given time [106]. To get a trend, one would have to run the model several times to develop a sensitivity curve.

1.1.1 Laser Beam Properties

The beam profile is a key parameter that is used in controlling the laser cutting operation are beam diameter and the depth of focus of the beam. The beam profile is related to the beam size and depth of focus through the beam quality factor, M^2, given by equation 4.3. The laser power for a continuous laser can be described by the intensity (W/cm^2) which is the power per unit area. The envelope of these spikes exhibits the form of a rising exponential, followed by a flat top and culminating in the falling exponential decay. The output from a pulsed laser is more easily described by approximating the form of the true output. The dimensionless temporal profile of a pulsed laser is given by:

$$p(t) = \begin{cases} \frac{I_{pk}(t)}{I_{pk;max}}, & t < t_{pulse} \\ 0, & t > t_{pulse} \end{cases} \quad \text{(Eq. 4-5)}$$

where $I_{pk;max}$ is the maximum intensity at t_{max}. For example, the GM-30 laser has an average pulse width of 250ns at a repetition rate of 1 kHz. The temporal profile of the beam described by equation 4-6 is shown in Fig 4-5.

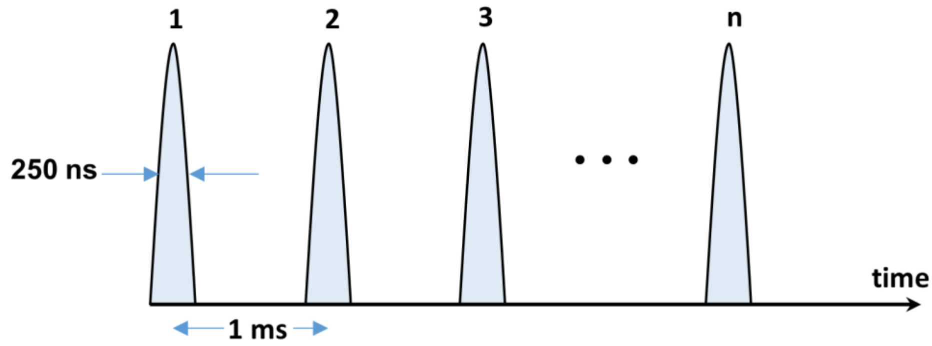

Fig. 4-5 Laser pulses from GM-30 Laser

In general, the output pulse from the GM-30 laser is not easily fitted by any mathematical expression. It has an intensity distribution similar to the TEM_{33} mode of a laser from the solution of the paraxial wave equation [101].

$$E_{mn}(x,y) = E_0 H_m\left(\frac{\sqrt{2}x}{w_o}\right) H_n\left(\frac{\sqrt{2}y}{w_o}\right) e^{ik(x^2+y^2)/2R(z)} e^{-(x^2+y^2)/w^2(z)} \qquad \text{(Eq. 4-6)}$$

Where m and n represent the transverse mode numbers and H_m and H_n represent Hermite polynomials and w_0 is the characteristic mode. The propagation of the electric field can be solved by the paraxial wave equation solutions as:

$$\left(\frac{\partial^2}{\partial x^2} + \frac{\partial^2}{\partial y^2}\right) E_o = -2ik\frac{\partial E_0}{\partial z} \qquad \text{(Eq. 4-7)}$$

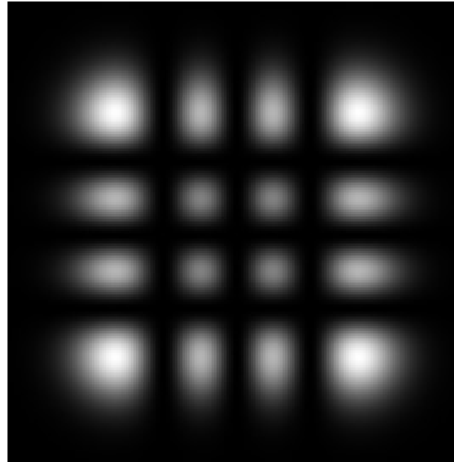

Fig. 4-6 Intensity profile of GM-30 laser beam

The propagation of the laser beam of higher order modes is the same as the lowest order mode [107]. The solution for the TEM_{33} mode is shown in Fig. 4-6.

4.3.1 Material properties

The properties of thermal spray coatings are different from their bulk values. The material parameters that are important include the specific heat capacity of the solid in all three phases, the melting point, the boiling point, the heats of fusion, the thermal conductivity, the optical properties (absorptivity and reflectivity). Most metals have high reflectivity (~99%) in the IR laser range [108]. It can drop to values as low as 0.1 during laser ablation, when the irradiance is high enough (approx. $10^8 W/cm^2$). This is could be attributed to roughening due to the temperature increase of the surface and melting of the surface [109] [110]. The reflectivity of copper is not very dependent on the angle of incidence at this wavelength. The effect of the laser beam penetration to the thermal diffusion length is used to select the type of heating the laser will include, whether it is surface heating or volumetric heating. This means that the thermal diffusion width inside the sample needs to be greater than the beam penetration width and smaller than the beam radius and the material thickness. Focusing high-energy laser pulses on a target causes heating, melting, and evaporation of a

thin layer of the irradiated material. Absorption of the laser energy by the evaporated particles leads to the ionization of the plume and the formation of plasma in front of the target. Due to the formation of plasma, the laser beam is partially absorbed by the plasma before reaching the target plasma shielding. The plasma shielding effect can have a significant influence on the choice of laser parameters required.

Table 4-3 Thermal and optical properties of copper (300K) [111, 112]

Parameters	Values
Mass density, ρ (Kg/m^3)	8940 (*s*) 8000(*l*)
Specific heat, C_p, (J/Kg·K)	420 (*s*) 494 (*l*)
Thermal conductivity, k (W/m·K)	390 (*s*) 170 (*l*)
Thermal Diffusivity, D (m^2/s)	1.15x10-4 (*s*) 4.3x10-5 (*l*)
Melting point, T (K)	1358
Boiling point, T (K)	2836
Heat of fusion, ΔH (J/ Kg·K) l_s	2.05×10^5
Heat of vaporization, ΔH (J/ Kg·K) l_v	4.073×10^6
Absorption depth, l_α (λ[μm]) (nm)	14 (0.532) 13 (1.06)
Absorption coefficient, α (λ[μm]) (cm^{-1})	7.1×10^5(0.532)
L_{th} (μm)	1.43
Reflectivity used in the model, R	.5 (enhanced with roughness)

4.3.2 Model

The solutions are given in two-dimensional axisymmetric coordinates with the following modeling assumptions:

1) Thermal equilibrium between the electrons and the lattice
2) Semi-infinite target
3) Constant material thermal and optical properties
4) Constant *absorption coefficient* and *surface reflectivity*.
5) No *plasma absorption*

6) Thermal properties of the material are assumed to be temperature independent

Using a semi-infinite heat transfer model with surface skin absorption and constant heat flux, the temperature profile is given by

$$T(z,t) = T_o(z) + \frac{2F_o}{k}\sqrt{\alpha t}\, ierfc\left(\frac{z}{2\sqrt{\alpha t}}\right),\ t < t_i$$
$$T(z,t) = T_o(z) + \frac{2F_o}{k}\left[\sqrt{\alpha t}\, ierfc\left(\frac{z}{2\sqrt{\alpha t}}\right) - \sqrt{\alpha(t-t_o)}\ ierfc\left(\frac{z}{2\sqrt{\alpha(t-t_o)}}\right)\right], t > t_{pulse} \qquad \text{(Eq. 4-8)}$$

Equation 4.8 is used to estimate the single-pulse temperature distribution profile on the substrate. Using an energy balance, the volume of the heat-affected zone can be determined by:

$$(1-R)E_{pulse} = \rho V_{HAZ}\left(c_p \Delta T_{s\to 1} + L_m + c_p \Delta T_{1\to v} + L_v\right) + E_{plasma} \qquad \text{(Eq. 4-9)}$$

$$V_{HAZ} \cong \begin{cases} \pi r^2\sqrt{\alpha t_p}, & r \gg \sqrt{\alpha t_p} \\ \frac{4}{3}\pi(\alpha t_p)^{\frac{3}{2}}, & r \ll \sqrt{\alpha t_p} \end{cases} \qquad \text{(Eq. 4-10)}$$

4.4 Results and Discussion

4.4.1 Laser Selection

The laser selection for the efficient ablation of thermal spray films is based on determining the ablation thresholds and ablation efficiency for the three lasers at similar power levels (0.8 - 2.0W). However, the beam spot sizes must first be determined. For the FW-40 and FW-150 laser, which have a Gaussian beam profile, the approximate beam radius, ω_0, can be computed from the slope, m, of a semi-logarithmic plot of the square of the ablated crater diameter, D^2, as a function of pulse energy based on [113]:

$$\omega_0 = \sqrt{\frac{m}{2}} \qquad \text{(Eq. 4-11)}$$

To determine the beam spot size at the target surface, the diameter of all the ablation holes was measured with the aid of software imageJ from optical microscope images taken for 100 and 1000 shot experiments. From these measurements, D^2 vs. $ln(E_p)$ graphs were plotted for both the 100-shot and the 1000-shot measurements. Pulses numbers less than 100 were difficult to obtain due to slow shutter speeds.

As seen in Fig. 4-7, the slope of the 100-shot and 1000-shot graphs for both the FW-40 and FW-150 laser are slightly different. The beam radius for the FW-40 based on 100 and 1000 pulses is determined to be 27.2 μm and 26.50 μm, respectively. The average beam radius for the FW-40 laser is 26.88 μm. The beam radius for the FW-150 for 100-shot and 1000-shot experiments are 13.9 μm and 14.01 μm respectively. The average beam radius for the FW-150 laser is 14 μm. The R^2 values obtained for each data set shows that the data points obtained fit very well to the logarithmic regime. The experimental results of the beam spot size are approximately twice the diffraction-limited theoretical value calculated using a 10x (NA 0.25) objective lens.

Because the beam profile of the GM-30 is not Gaussian, the beam spot size for the GM-30 is calculated based on equation 4-3 from the manufacturer supplied beam quality factor. The focused beam spot size for the GM-30 laser is calculated to be 11 μm for a 100 mm plano-convex lens.

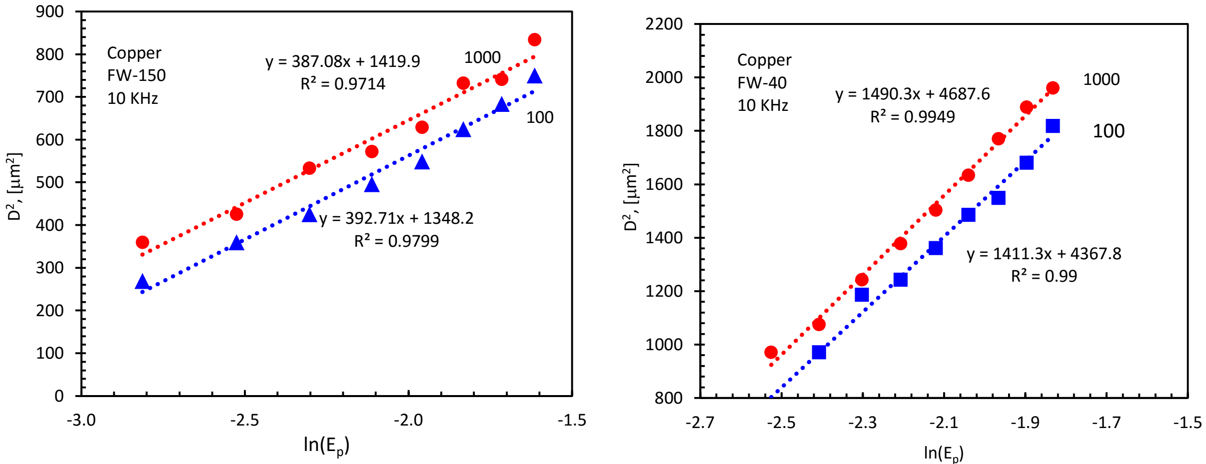

Fig. 4-7 Graph of D^2 vs. $\ln(E_p)$ for FW-150 and FW-40 lasers on copper with holes ablated with 100 and 1000 pulses.

The ablation threshold for copper by irradiation with the FW-40, FW-150, and GM-30 lasers was also investigated by ablating craters at different laser fluences. The diameter of all the ablation holes was measured with the aid of software imageJ from optical microscope images for both 100 and 1000 shots experiments. Experimental results are shown in Fig. 4-8, Fig. 4-9 and Fig. 4-10 for craters made in copper. For the GM-30 laser, data for some craters made at high repetition rates were not included because only surface melting was observed. Craters with the evaporation of the material were created at higher pulse energy or with more laser pulses. At high fluence, a steeper increase of the crater diameter is observed. The ablation threshold depends on the number of pulses incident on the same location of the sample. Results of the evaluation according to equation 4-6 are given in Table 4-4.

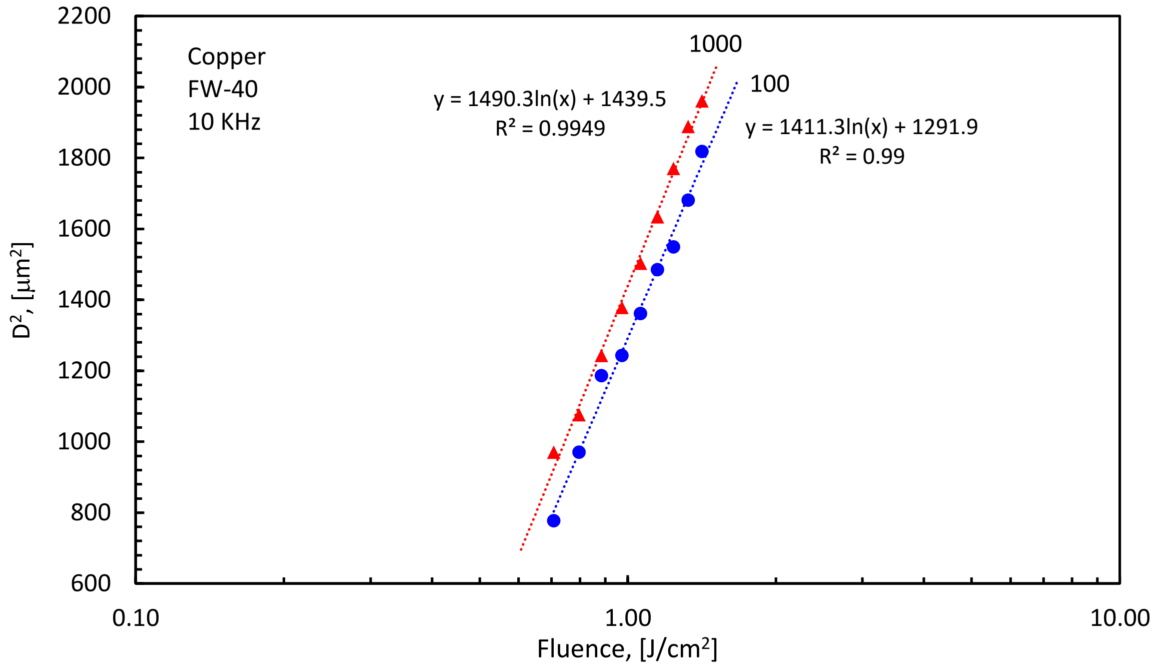

Fig. 4-8 Crater diameter versus laser fluence to evaluate ablation threshold for FW-40 laser. Numbers (100, 1000) indicate the number of pulses used to ablate a crater.

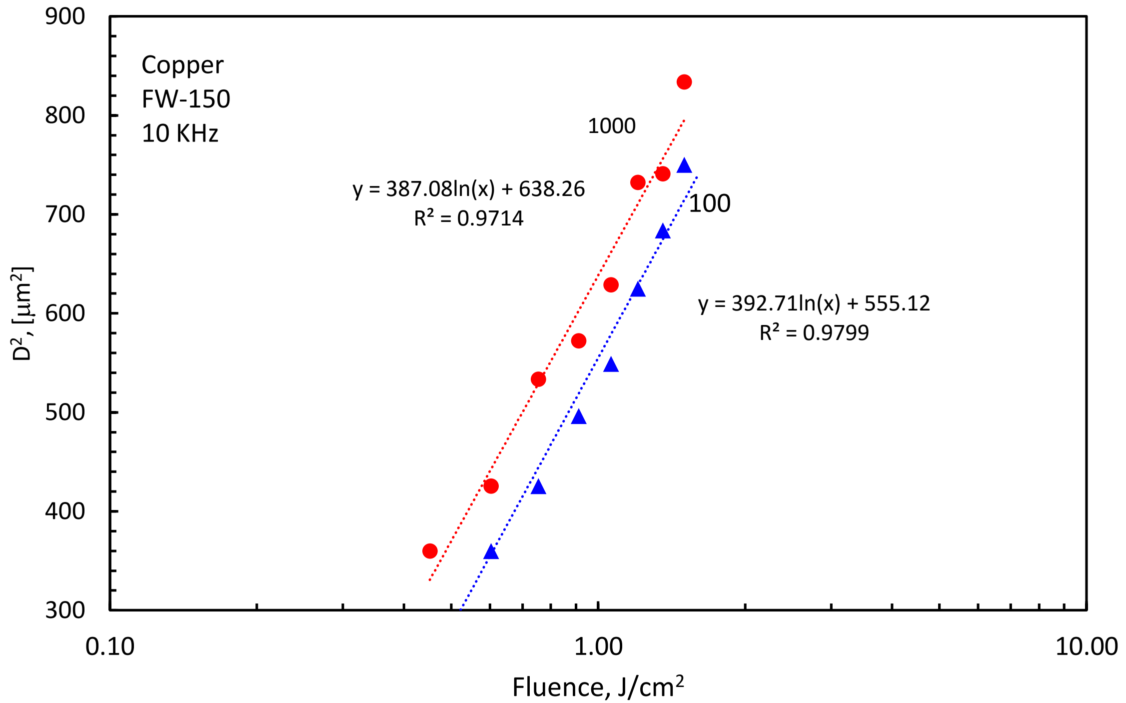

Fig. 4-9 Crater diameter versus laser fluence to evaluate ablation threshold for FW-150 laser. Numbers (100 and 1000) indicate the number of pulses used to ablate a crater.

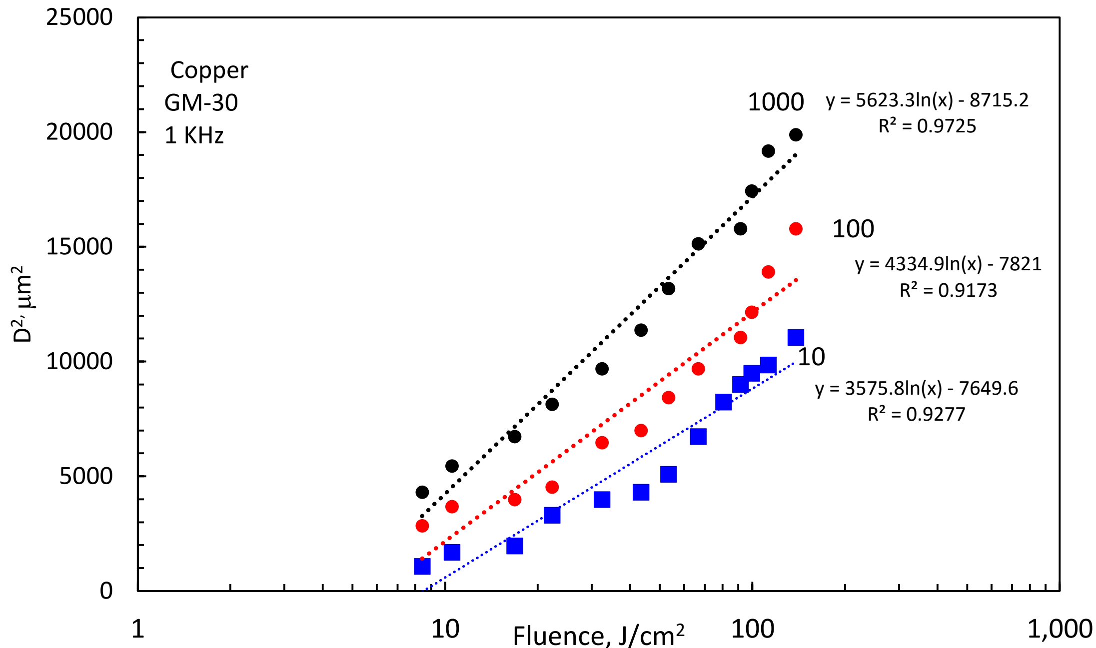

Fig. 4-10 Crater diameter versus laser fluence to evaluate ablation threshold for GM-30 laser. Numbers (10, 100 and 1000) indicate the number of pulses used to ablate a crater.

Table 4-4 Ablation threshold of copper with different laser system

Laser	**Pulse Width**	**Ablation Threshold, (ϕ_{th}) J/cm²**			
		10 Pulses	100 Pulses	1000 Pulses	Reference value
FW-40	35 ns	-	0.33	0.38	0.375 [114]
FW-150	40 ns	-	0.27	0.22	-
GM-30	250 ns	8.49	5.83	4.71	-

The ablation threshold fluence decreases with an increasing number of pulses due to the incubation effect, in which the time interval between subsequent pulses is smaller than the time for heat diffusion into the bulk. As a result, the temperature rise due to the first few pulses increases the absorption for the following pulses. This is useful to increase the material removal rate during industrial laser milling processes using high repetition rate ultrafast laser sources [115].

The ablation rate was determined for the three lasers by milling square holes with the lateral dimension of 0.5 mm × 0.5 mm with multiple laser pulses. The laser power was varied during the

experiments while the number of laser pulses was kept constant for the same laser. For the FW-40 laser, 2.5 million pulses were applied with the pulse energies from 80-160 µJ. For the FW-150 laser, 0.5 million pulses were applied with pulse energies from 80-200 µJ. For the GM-30 laser, 0.25 million pulses with pulse energies from 0.8-13 mJ were applied. The depth of the holes was measured from OM images, and the volume of ablated material was calculated. The depth of laser-milled cavities varied from 15 up to 200 µm. The ablation rate (µm/pulse) obtained for the FW-40, FW-150, and GM-30 laser is shown in Fig. 4-14.

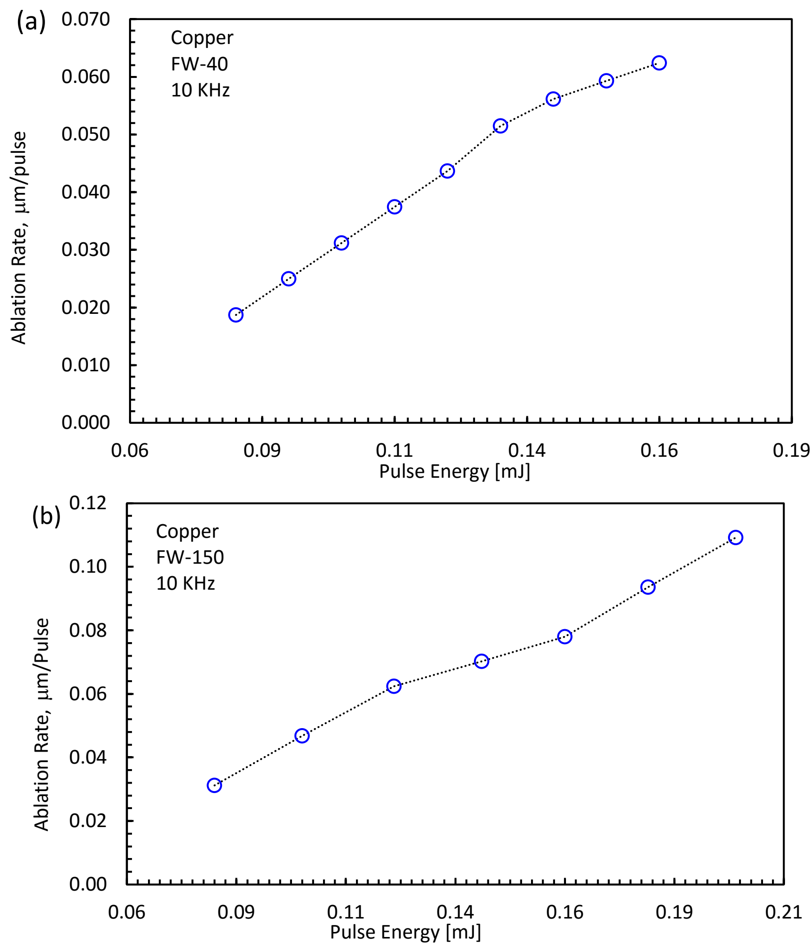

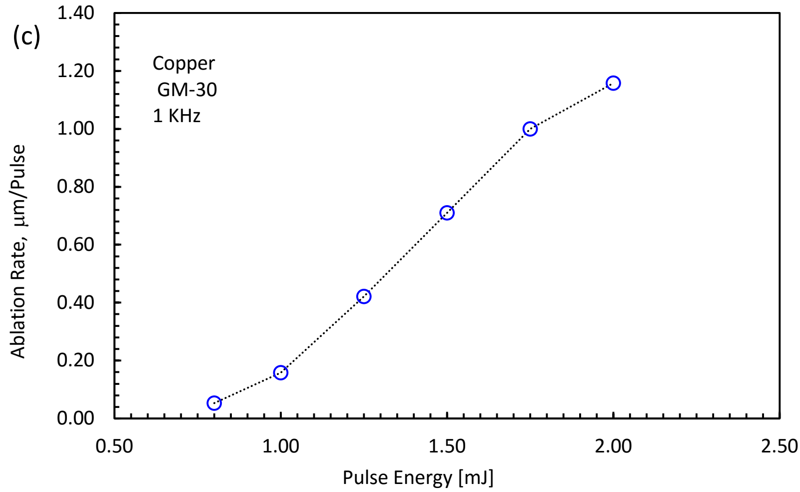

Fig. 4-11 Ablation rate of the copper as a function of laser pulse energy for (a) FW-40 laser, (b) FW-150 laser and (c) GM-30 laser

The mean ablation rate does not give the efficiency of machining, which is needed for laser selection. Therefore, the measurements were used to calculate the material removal rate (mm^3/s), and the ablation efficiency (mm^3/mJ) to represent the real efficiency of laser processing. Figure 4-12 shows the material removal rate as a function of the mean laser power and Fig. 4-13 shows the ablation efficiency as a function of the laser power.

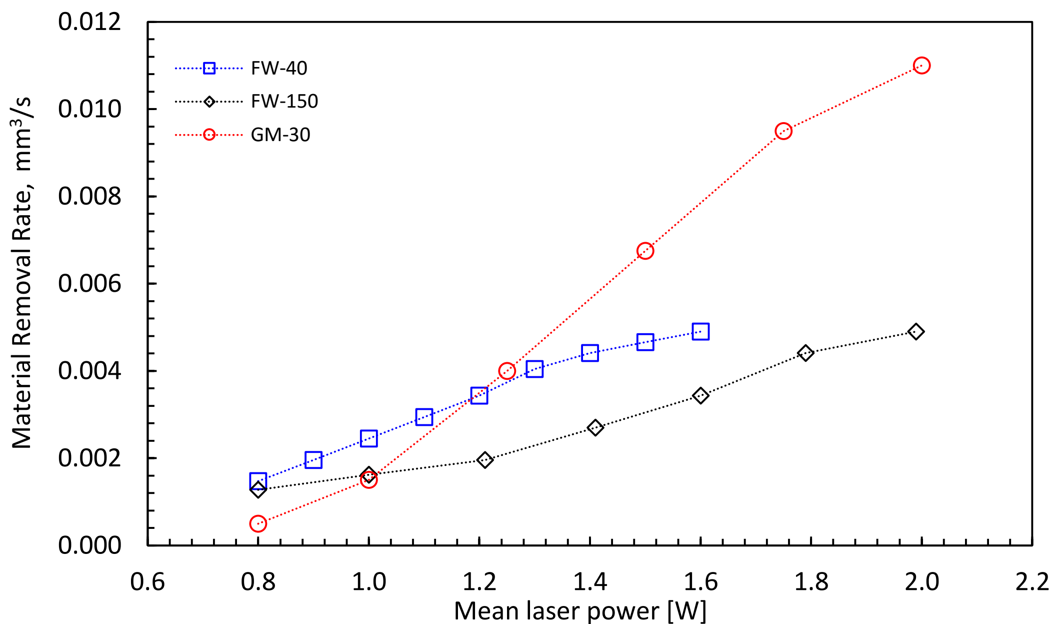

Fig. 4-12 Material removal rate of the copper as a function of laser power

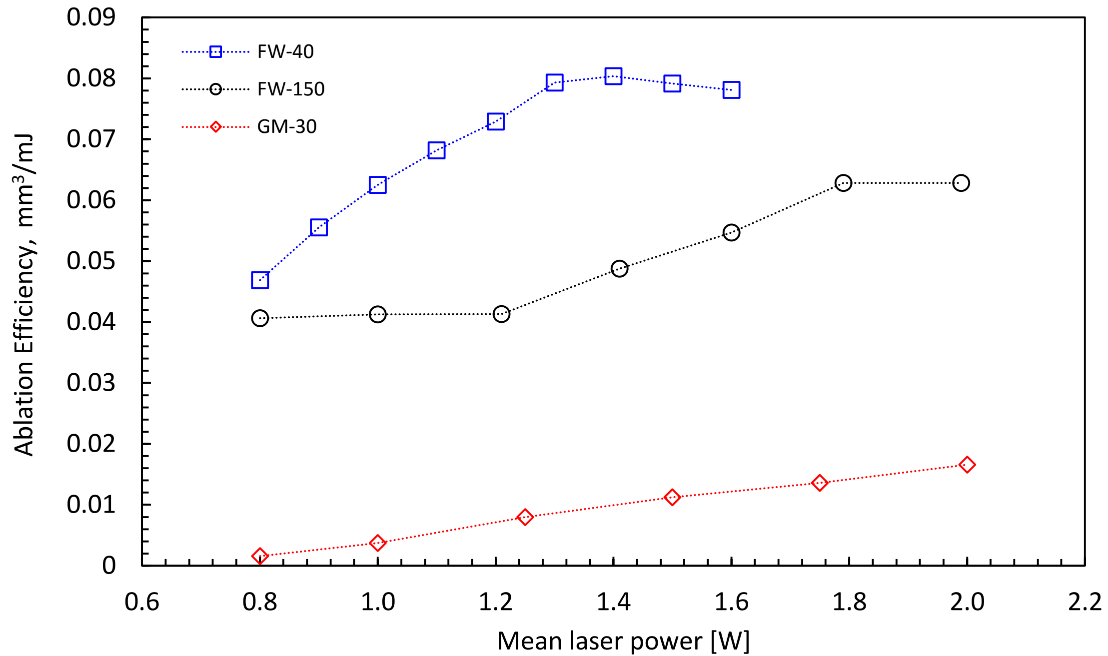

Fig. 4-13 Ablation efficiency of copper as a function of laser power

The energetic ablation efficiency of the FW-40 laser is the highest followed by the FW-150 laser and the GM-30 laser as expected. However, the GM-30 had the highest material removal rate from the three lasers. This is a result of the increased pulse energy and longer penetration depth. The thermal and optical penetration depths values are given in Table 4-5. The FW-40 laser has the lowest thermal penetration depths, which explains its low MRR even though it has high ablation efficiency. For the same average laser power and cost, lower pulse energy requires more laser shots, especially when the pulse energy is near the ablation threshold. As a result, it is important to understand that simply using higher PRF does not allow a higher processing speed if the pulse energy is not sufficient. Based on this finding, the GM-30 laser is the main choice for further processing applications.

Table 4-5 Laser thermal optical penetration depth of copper for available lasers

Laser	Wavelength (nm)	Pulse Width, τ (s)	Thermal penetration depth, $(D\tau)^{½}$ (m)	Optical penetration depth, α^{-1} (nm)
FW-40	523	3.5×10^{-8}	1.9×10^{-6}	1.71×10^{-8}
FW-150	1060	4.0×10^{-8}	2.1×10^{-6}	1.20×10^{-8}
GM-30	527	2.50×10^{-7}	5.2×10^{-6}	1.70×10^{-8}

4.4.2 Optimal laser processing parameters

The GM-30 laser was used to determine the optimal parameters for patterning the copper substrate. The ablation rate as a function of laser power was determined in a similar fashion to the previous section. The results are shown in Fig. 4-14, where it can be seen that the material removal rate peaks around 5.0 W.

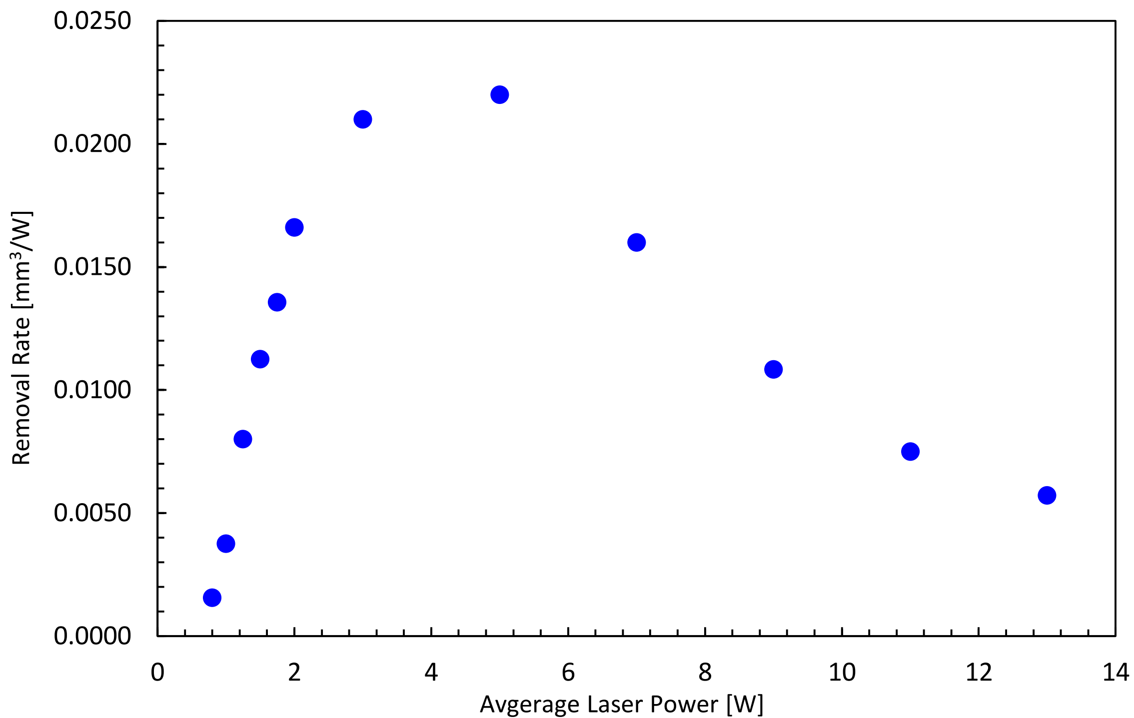

Fig. 4-14 Material removal rate of copper as a function of laser power for GM-30 laser

The processing strategy and optimization procedure are as follows. The first step was to scribe lines on a thermal spray copper surface close to the highest material removal rate. The laser cutting speed is adjusted until all of the material is removed, and the substrate is visible, i.e., that

electrical isolation is made. The optimal laser cutting parameters are shown in Table 4-6. The increase of scanning speed reduces the material removal rate by decreasing the overlap degree between individual laser pulses. Complete film removal by a minimal number of shots per length is usually desirable since otherwise repeated heating and melting tends to degrade the machining quality and induce unwanted intermetallic diffusion from film to the underlying layer. This trend assists in faster processing. In addition, the upper limit of the pulse energy is set to damage threshold of the underlying layer(s) or film delamination limit; for the current material system, it is likely that the film delamination limit will form the upper limit due to high residual stress and large film thickness. The delamination limit should be determined in the course of the offset scanning procedure.

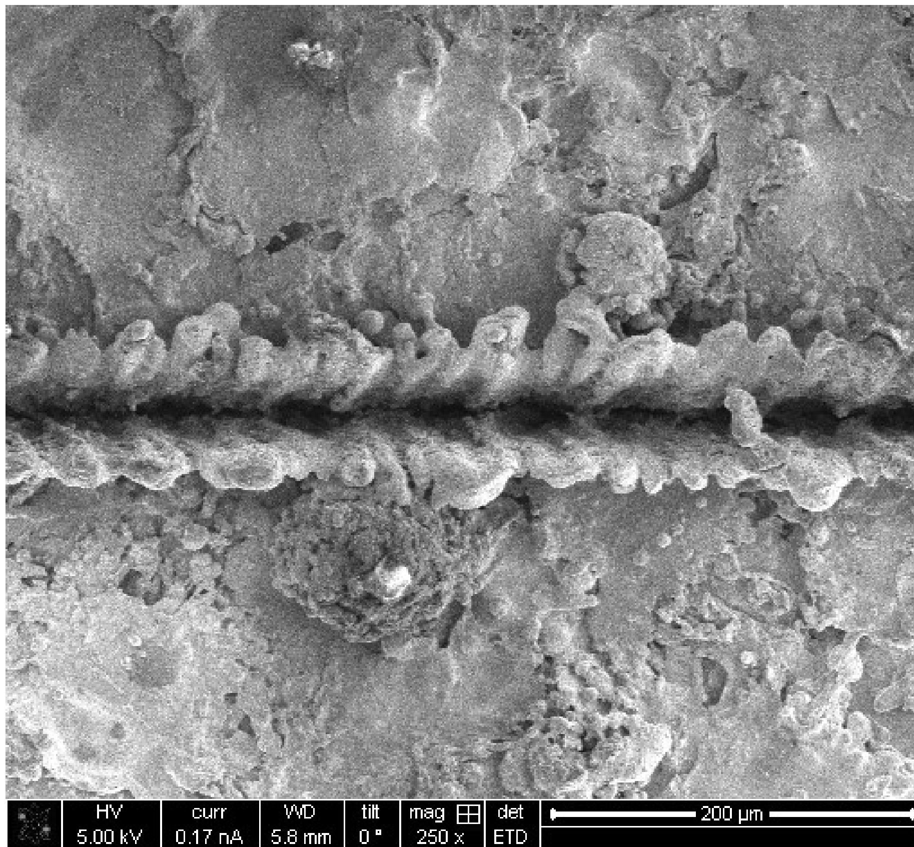

Fig. 4-15 Single line patterning of copper with GM-30 laser

Table 4-6 Optimum Laser Cutting Parameters

Material	Thickness	Laser Wavelength (nm)	Power (W)	Focal length (mm)	Cutting Speed (mm/s)	Gas Assist
Cu	70 µm	527	6.5	100	7	None

Note that it is difficult to isolate a thick film with multiple scans along a single path (i.e., no offset) due to tapering in trench shape. The incubation effect by the multi-shot effect broadens the entrance of the machined trench without ensuring isolation at the bottom interface of thick film making it difficult to achieve high-quality isolation. A top-flat beam shaping can mitigate this issue but with increased laser power and system budget.

Because large grooves are required, machining was performed by scanning the area where cutting is repeatedly performed and offsetting by a specified distance, as shown in Fig 4-16. In this way, the laser beam power, the scanning speed and the number of passes are empirically optimized to provide efficient removal of material while minimizing the heat affected zone (HAZ) and the amount of material removed from the substrate. After the best laser parameters had been found, laser cutting was performed by removing material from the top of the thermal spray surface by a focused laser beam while the motion stage moves to execute a programmed motion. The scan spacing is also an important parameter that was optimized. A similar test was performed on the cylindrical copper sample to determine the optimum cutting parameters. Because the rotary stage can go up to high speeds, a wide range of power and scanning speed combinations are available. The optimum laser parameters were 13 W @ 1 kHz and scan speed of 0.67 rad/s, which is equivalent to 25mm/s on a linear stage. The linear stage, in contrast, has a maximum speed of 10 mm/s.

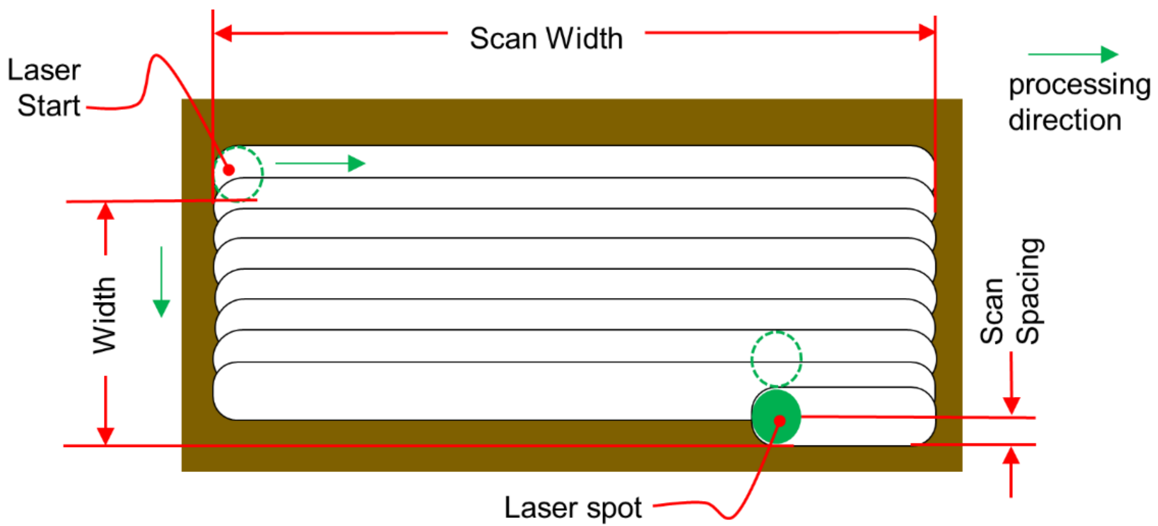

Fig. 4-16 Machining parameters for extended machining

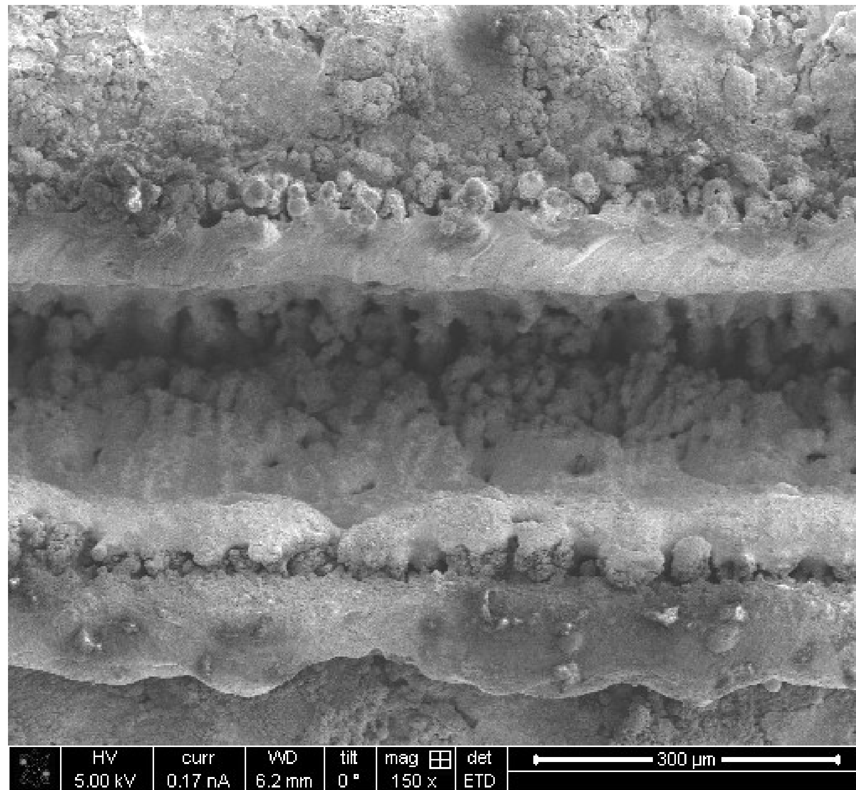

Fig. 4-17 Multiple line cutting of copper sample with GM-30 laser

4.4.3 Effect of shield gas

It was found that laser cutting in ambient air did not result in good cut quality. Re-deposited debris from re-solidified molten material on the cut edge resulted in electrical shorts between machined

regions. Mild gas injection (<< Ma~0.3) cannot exert effective momentum to expel a supersonically expanding plasma plume induced by a strong single shot ns laser pulse (rather than displacing the surrounding gas medium only and so only light gas molecules such as helium are effective for reducing plasma interaction via collision with gas molecules). However, a significant improvement of machining quality by mild injection of compressed air implies a somewhat different mechanism of the plasma generated at current laser conditions. One way to minimize this is to use assist gas to blow away any molten material from the pool. Therefore, cutting was performed under inert gas jets of nitrogen and compressed air. The inert gas assists in the cutting process by protecting the cutting front of the material from oxygen and acts to sweep potential recast material out of the material removal area. In most cases, a marked improvement was observed by using inert gasses.

The temperature on the surface for a single pulse is shown in Fig 4-18. The temperature begins to increase rapidly during the pulse period and begins to cool rapidly after that. Since the model does not take into account the phase changes, the actual temperature is not lower. Fig 4-19 shows the temperature distribution at different times.

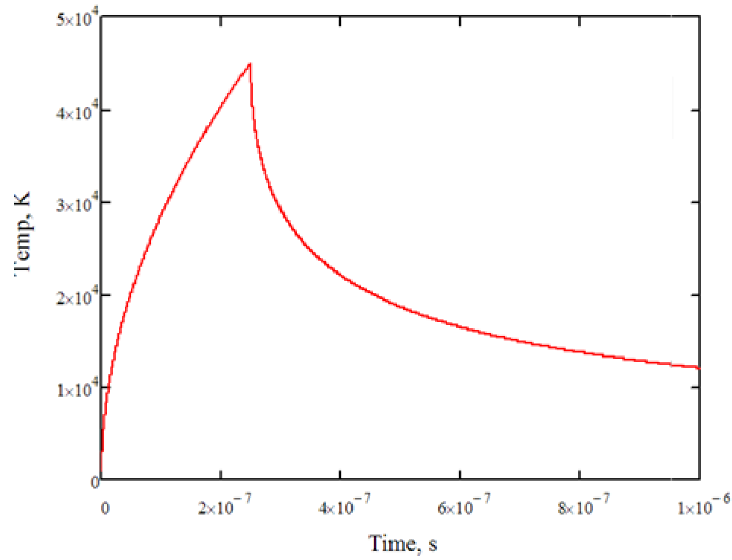

Fig. 4-18 Surface temperature distribution for a single-pulse on copper substrate

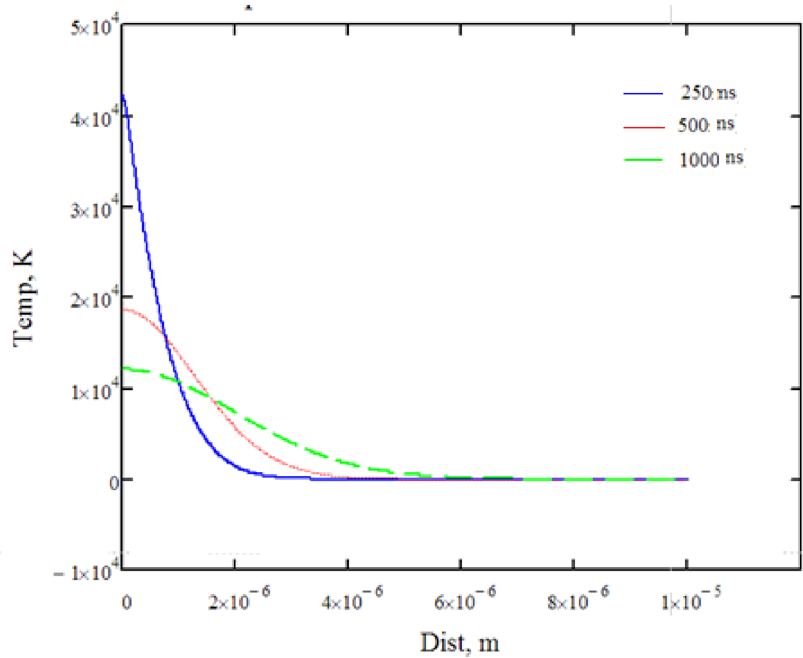

Fig. 4-19 Temperature distribution at different times

Nanosecond laser absorption consists of the instantaneous heating of the electronic system (10^{-15} s) and the rapid transfer of this energy to the lattice system (10^{-12} s). As a result, it is characterized by normal heating, melting, and vaporization. It is a temperature dependent process, so problems like micro-cracks are commonly observed at heat-affected zones. Plasma formation

characterizes ablation in metals due to high free electron density [116-118]. Several studies have been performed looking at the ablation of metals like copper and steel. Laser ablation results in a cascade of tightly coupled processes, which depend on the laser parameters, the material properties of the sample as well as on the ambient environment. In the early stages after the impact of the laser pulse, the energy is absorbed by material and phase transitions begin to occur. Vaporized material is also ejected. Plasma formation begins in the early nanosecond time scale as well as liquid sample ejection. Plasma expansion with shockwave formation during laser ablation of materials in back-ground gasses is a complex process. The incoming laser radiation is absorbed by inverse bremsstrahlung absorption process. The effect of plasma shielding is not an issue for intensities lower than 10^8 W/cm^2 because vaporization is still very limited, leading to a very short and rather cool vapor plume (temperature approx. 800 K), consisting only of neutral Cu^0 atoms (hence, no ionization takes place) [111]. If the laser is still incident on the surface, plasma shielding and further heating of the plasma will occur. In the microsecond time scale, thermal radiation, convection, and conduction come into play. Plasma expansion and plume condensation also occur on this timescale.

4.5 Summary

In this chapter, experimental results from laser patterning of thermal spray coatings were presented. The optimization of laser parameters is important for successful electrical isolation needed in thermal spray device manufacturing and for high-quality machining. Short-pulse laser processing has the potential for very precise and low damage processing. Three different nanosecond lasers system are compared in which the laser power, laser wavelength, type of focusing lens, processing speed, repetition rate, and pressure and flow of purge gas were varied. The optimum

laser parameters were those that minimize the heat-affected zone and resulted in the fastest processing times. The resulting laser patterns were characterized using both optical and scanning electron microscopy, and by verifying electrical isolation between patterned regions. It was found that faster processing speeds at higher power results in improved cut qualities. The most important parameters in this work are the processing speeds. The characterization of the sample after laser processing did not find any significant change in the use of a background gas for machining copper.

Chapter 5

Additive-Subtractive Manufacturing of a Thermoelectric Generator

In this chapter, a TEG module has been fabricated for the first time using thermal spray technology and laser micromachining. The TEGs are fabricated directly onto engineering component surfaces. First, current fabrication techniques of TEGs are presented. Next, the steps required to fabricate a thermal spray-based TEG module, including the formation of the metallic interconnect layers, and the thermoelectric legs are presented. Technique for bridging the air gap between two adjacent thermoelectric elements for the top layer using a sacrificial filler material is also demonstrated. A flat 50.8 mm × 50.8 mm TEG module is fabricated using this method and its performance is experimentally characterized and found to be in agreement with expected values of open-circuit voltage based on the materials used.

5.1 Thermal-Spray-Based Thermoelectric Device Fabrication

All thermal spray work was done on-site at the Center for Thermal Spray Research (CSTR) at Stony Brook University. Atmospheric plasma spray (APS) was chosen for this work since it was found to provide the best feature quality. The powders used had a minimum of >99% purity and particle size of <60 μm. An F4-MB (Sulzer Metco, Switzerland) and SG100 plasma torch (Praxair Surface Technologies, USA) were used for spraying.

The laser used was the GM-30 Nd:YLF pulsed laser (Photonics Industries, USA) which was found to be most suitable for the micromachining conditions required. Linear motion control for the sample was achieved using three linear translation stages (Coherent LabMotion, USA) mounted on a rigid post. Each stage has a resolution of 0.5 μm and a range of 50 mm. The stages are oriented mutually perpendicular to each other along the x, y, and z-axes. The motion control system can be programmed to control the laser beam delivery and execute a pre-programmed motion profile

Metal alloy powders were chosen to demonstrate the feasibility of this manufacturing method in this work. Although the resulting ZT is lower than that for other TE materials, metal alloys are inexpensive, straightforward to spray, and have been studied and characterized extensively. The powders consisted of 38% Ni and 62% Cu for the n-type material and 80% Ni and 20% Cr for the p-type material supplied from Sulzer Metco (Westbury, USA). These alloys were chosen because they were readily available and are also similar to those used in a commercial E-type thermocouple (*chromel-constantan*), which has one of the largest Seebeck coefficients (~68 μV/°C), thus maximizing power output [119]. The powder compositions were chosen based on availability. Therefore, the exact Seebeck coefficient for these alloy compositions is not known.

5.1.1 Device Design and Fabrication Process

One of the main requirements in the design of a thermoelectric module is to determine the optimum module geometry, based upon available thermoelectric material and manufacturing methods [76]. It also includes the choice of substrate and conducting material. The basic requirement for these junctions is that they must conduct electricity and heat with as little impedance as possible to reduce losses while remaining functional. As a result, thin layers for the ceramic and

metal interconnects are preferred, and thick layers are preferred for the active TE materials. Since the conducting layers will have a large area and considerably less thickness than the TE legs, making the requirement for the bulk conductivity less stringent in the choice of materials. Therefore, any metal or alloy with high electrical conductance (Cu, Ag, etc.) can easily meet this requirement. Because thermal gradients, thermal cycling, and vibration can impose significant stress during application, adhesion between the different layers is very important for long-term, reliable TEG performance. The ability to withstand thermal shock and temperature cycling is connected with the relative coefficient of thermal expansion (CTE) of the various components in the module. Ideally, the CTEs should match or be very close. CTE mismatch can lead to residual stresses that develop at the joints reducing interfacial bonding [120]. The diffusion layer between the two adjacent materials should be at least a few microns thick to ensure good contact and be stable when exposed to hot-side temperatures over time [121]. Other desirable properties include good mechanical stress, the ability to withstand thermal shock and cycling, long life without serious deterioration and the absence of harmful interactions – chemical reactions – with the thermoelectric materials. Finally, laser processing parameters and their effect on the device fabrication process must be considered. The conducting layers must be thick enough to pass the electrical current, but thin enough to ensure good adhesion and reduce the time for laser micromachining. Good contact adhesion also aids heat transfer during laser micromachining. Poor adhesion between the conducting copper layer and the substrate can cause film peeling and delamination upon heating. The proposed design of the flat TE legs is shown in Fig. 5-1. The insulating and conducting layers are made from yttria-stabilized zirconia (YSZ), and copper, respectively. A thin layer of thermally sprayed 7% yttria-stabilized-zirconia (YSZ) is an industry-standard insulating thermal

barrier coating designed to have a low thermal conductivity of about 1.2 W/m·K. The properties of the materials used are shown on Table 5-1.

Table 5-1 Transport Properties of Materials Used [122-124]

Property of material	**YSZ**	**Copper**	**$Ni_{80}Cr_{20}$ (*p*-type)**	**$Cu_{62}Ni_{38}$ (*n*-type)**
Electrical Conductivity (1/Ω·m)	0.1	9.8×10^{-8}	2.5×10^{5}	6.0×10^{5}
Thermal Conductivity (W/m·K)	1.2	50	6	6
Seebeck Coefficient (V/K)	–	–	0.041	0.068
CTE (x 10^{-6})	10.8	16.6	12.8	14
Density, (kg/m^3)	6100	8960	8500	8900

The power output and conversion efficiency are important parameters that can be used to evaluate the performance of TEG. It can be shown that the optimal leg thickness is greater than 1 mm[76]. This is well suited for the thermal spraying process where coatings of thickness up to 2 mm are routinely sprayed. The final design based on $N = 40$ is shown in Fig. 5-1.

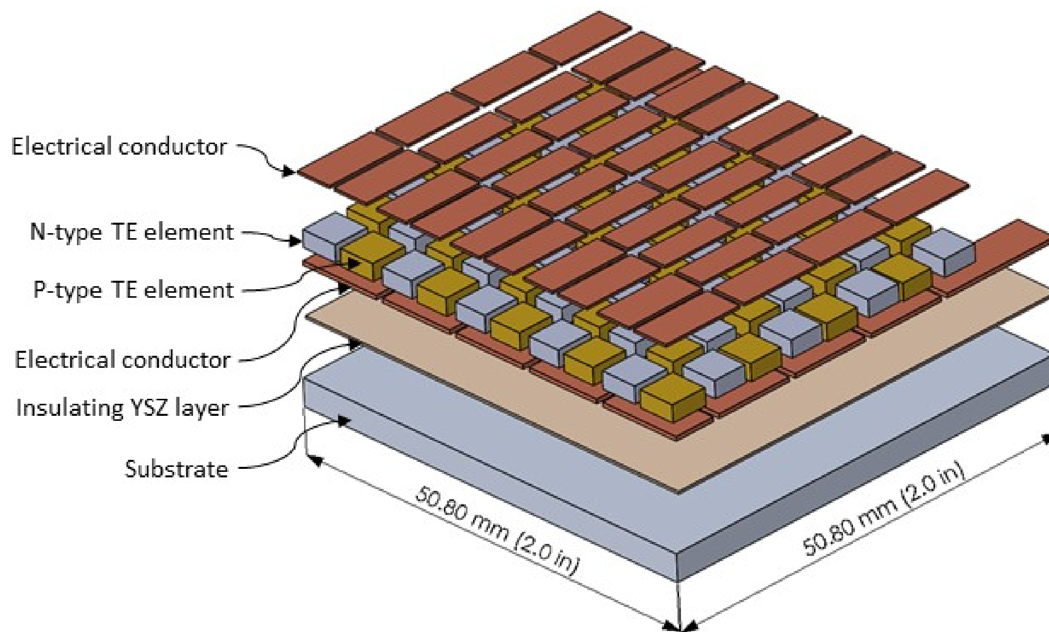

Fig. 5-1 Module design and configuration

5.1.2 Overall Device Fabrication Steps

The fabrication of the device involves three steps: (i) deposition and patterning of the bottom layers, (ii) deposition of both *p*- and *n*-type thermoelectric legs, and (iii) deposition and patterning of the top conducting layer. The steps are shown schematically in Fig. 5-2. In steps *b* and *d*, blanket layers of insulating and conducting materials are sprayed, after which laser machining is performed. The *n*- and *p*-materials are deposited sequentially using masks in step *c*.

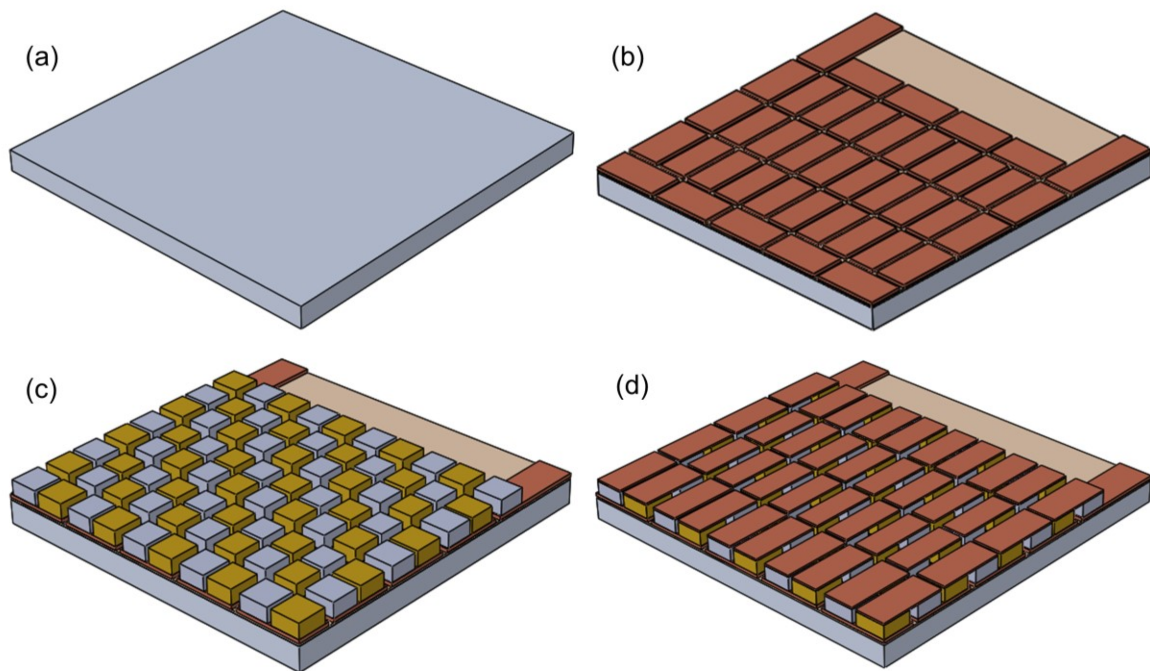

Fig. 5-2 Process steps to fabricate a TEG module (a) metal substrate, (b) apply bottom electrode and pattern, (c) deposit *n*- and *p*-type TE legs, (d) deposit top electrode layer

5.1.2.1 Fabrication of Bottom Layer

The bottom layer of the TEG device is fabricated by spraying a blanket layer of an insulator followed by a layer of conducting material on a substrate. Steel and aluminum representing common engineering component materials were tested as substrates. Flat coupons of aluminum (50.8mm x 50.8mm x ~3 mm thick) and steel (50.8 mm x 50.8 mm x ~1 mm thick) and a round cylinder

of aluminum (76.2 mm ∅ and ~ 3 mm thick) were prepared for spraying by grit blasting the surfaces. The top layer sprayed from YSZ + copper will provide the electrical pathway for the TE elements to be connected in series. The range of thicknesses tested for the YSZ and the copper layer range from 0.5-1.0 mm.

The GM-30 laser is used to test different machining parameters on the YSZ + copper layer sprayed on the bottom substrate. The laser machines the copper layer exposing the YSZ layer. The substrate is mounted on a motion stage and the position of the sample with respect to the beam spot as well as the rate of ablation are precisely controlled by adjusting the stage position and speed. The laser power density and the number of passes determine the depth of the machining into the substrate. Machining into the insulating layer is not an issue as long as the laser does not penetrate the substrate. Finally, in order to optimize the process, four different types of assist gasses are tested – Helium, Nitrogen and Argon from standard high-pressure cylinders, and compressed air. The gas pressure is regulated and supplied at 40 psi (2.757 bar) through a (0.03 in) nozzle directed at the beam spot to remove debris during machining. At this relatively low pressure, it has no effect on the ablation dynamics and machining quality. Laser parameters for the efficient removal of material are empirically obtained.

The next step is to spray the *p*-type and *n*-type TE legs on the target zone patterned on the bottom layer as shown in Fig. 5-2c. Various masking techniques have been developed to protect component areas next to the target zone from impact by overspray particles including metal "shadow" or "contact" masks, high-temperature tapes and paint on masking compounds [34]. Metal masks can be placed on top of the substrate offset from it and work equally well on flat and round surfaces. A slight taper is included in the mask cutouts to provide a narrow feathered edge rather

than a sharply defined edge. This reduces the stress developed at the edge of the coating minimizing opportunities for delamination. The order of the TE material sprayed is not important but it is preferable to deposit one type of TE leg immediately after the other. The mask for the second spray needs to be modified so that it can accommodate the already spayed *p*-type legs. Any excess TE material that is sprayed into the patterned grooves can be removed with the laser.

The top conducting is fabricated by spraying a blanket layer of copper over the TE element legs. It provides metallization for the two adjacent *p*- and *n*- type legs. To complete the circuit, the top layer must be laser processed to form the TE couples connected in series. Finally, after the top copper layer has been deposited and processed, a heat sink can be integrated on the top layer. A dielectric is needed in between the heat sink and the top layer to prevent shorting the TE legs. This can also be thermally sprayed or integrated into the heat sink. The steps outlined above complete a functional TEG. The manufacturing method is amenable to automation and also compatible with cascading or multi-staging.

5.2 Results and Discussion

5.2.1 Fabrication of Bottom Layer

Both steel and aluminum substrates were atmospheric plasma-sprayed with copper + YSZ layers used after grit blasting. After several trials, the best spray conditions obtained with APS were used to successfully spray ~0.3 mm of YSZ followed by a ~0.5 mm of copper on a flat substrate. The copper + YSZ layer resulted in good adhesion and was uniformly spread on the substrate. The top copper layer roughness is also good for laser processing and subsequent spraying of the TE legs, without the need for grit blasting. The top view and an SEM cross section of the sprayed layers

are shown in Fig 5-3. As shown in the image, the interdiffusion length between the substrate and the insulator is (~10 μm) and between the insulator and the copper (~50 μm).

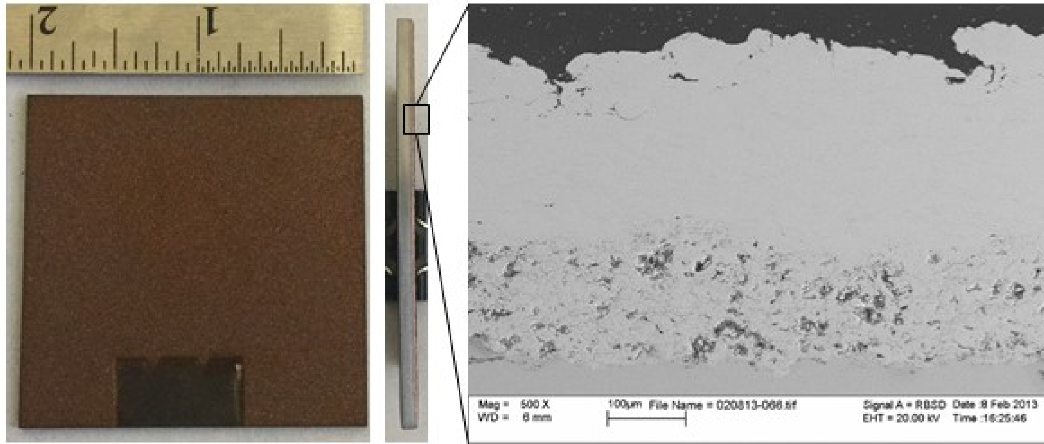

Fig. 5-3 Results from APS spraying of bottom electrode layer on flat substrate

The sprayed copper layer is laser patterned to finalize the bottom electrode. The optimal processing parameters used are listed in Table 5-2. Details of the selection of these parameters are described in Chapter 4. The grooves are ~0.7 mm wide and made with multiple passes of the optimized laser parameters. The result after micromachining the top copper layer is shown in Fig. 5-5.

Table 5-2 Optimal Laser Cutting Parameters

Parameter	Flat Substrate
Focal Length	50 mm
Laser Power	13 Watts
Scan Speed	8 mm/sec
Scan Spacing	65 μm
Spot Diameter	~50 μm
Scan Length	50 μm
Number of Passes	8
Assist Gas	Compressed Air

Fig. 5-4 Patterned bottom copper electrode on a flat substrate

5.2.2 Deposition of both *p*-type and *n*-type thermoelectric materials

Metal contact masks can be placed on the substrate with a slight taper to spray high aspect ratio features. The mask is manufactured from 3.2 mm thick aluminum on a CNC machine using a DSLS 3000 CNC milling machine (*Taig Tools, Chandler, AZ,* USA). The *p*-type and *n*-type TE legs are sprayed one after another to complete the active TE legs using APS. The average TE leg thickness after spraying was 1.6 mm for the *p*-type legs and 1.4 mm for the *n*-type legs, with the height being limited by the mask thickness. The masks used with the corresponding sprayed TE legs sprayed are shown in Fig. 5-5.

Fig. 5-5 Thermal Spray of *p*-type and *n*-type legs on flat coupon & masks used

Some TE material overspray was deposited into the grooves that electrically separate each TE junction. The laser was used to remove this material to avoid electrical shorting. A long depth-of-focus lens was used, and the laser power was set to just below the ablation

threshold to heat the debris until it had sufficient energy to detach from the surface. The cleaning operation was repeated until all of the over-sprayed material was removed. Electrical isolation between the processed regions was verified by measuring the resistance with a digital multimeter and confirming that the meter reads an open circuit (>10^6 Ω).

5.2.3 Fabrication of top conducting layer

After spraying, the top surface of the TE legs was polished to achieve a uniform thickness of 1.4 mm. For the temporary filler, an 80-20 % weight mixture of fine sand and polyvinyl alcohol (white glue) was found to work well as described in Chapter 3. The sand provides support and high-temperature tolerance for the thermal spray process while the PVA acts as a binder that can be removed by moderate heating. Just enough glue is used to hold the sand in place when dry. Referring to Fig. 5-6, the mixture is squeegeed into the grooves and allowed to dry for 24 hours. After drying, a ~0.5-mm blanket layer of copper is sprayed on top. The sample is then placed in an oven at 350 °C for 15 minutes to burn out the glue, after which the sand is removed by gently tapping the sample on its side. The final step is to laser process the top coating to electrically separate the TE junctions and complete the device. The optimal parameters for patterning the top coating are listed in Table 5-3. The right image in Fig. 8 shows the final TEG with isolated electrical regions on the top copper layer.

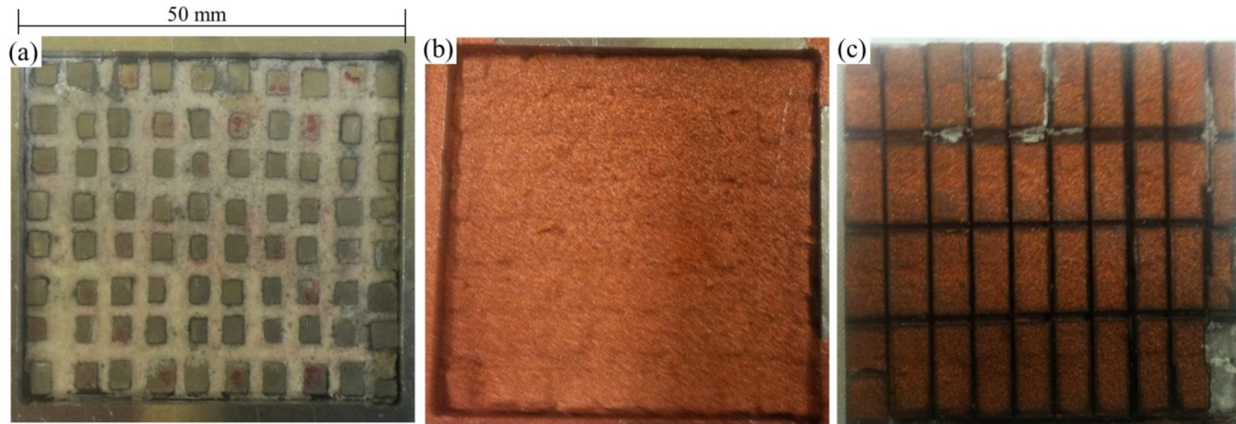

Fig. 5-6 (a) Temporary filler material applied to the legs and (b) blanket coating of copper sprayed and (c) final device after micromachining top layer

Table 5-3 Laser Cutting Parameters for Top Coating

Parameter	Optimum Value
Focal Length	50 mm
Laser Power	8 Watts
Scan Speed	6.5 mm/sec
Scan Spacing	65 µm
Spot Diameter	~50 µm
Number of Passes	8
Total Width	0.7 mm
Time	~ 8 min
Assist Gas Used	None

5.2.4 Testing and Characterization

The measured internal resistance of the device was 90.1 Ω. Only 26 of the 40 TE couples were functioning due to delamination from the surface of the bottom conductor during the fabrication process. This delamination from the bottom substrate may have occurred because of cracks that developed in the ceramic layer due to thermally induced stresses during the spraying of the TE legs. Close inspection of the samples after spraying revealed that cracks had developed on the interface between the insulating layer and the bottom metal substrate, which resulted in the separation of several TE junctions from the metal substrate. Ceramic paste (Aremco Products, Cottage, NY, USA) was used to re-attach these junctions to the substrate.

The completed thermoelectric device was tested for its performance on a TE test rig. The heater section of the test rig consists of a copper block with four embedded 100 W cartridge heaters. The TE module under test sits on top of a temperature-controlled copper block as shown in Fig. 5-7. The temperature of the copper block is controlled using a thermocouple inserted near the top of the block for feedback, and a fan is used to cool the top of the TEG. The entire assembly is housed in a high-temperature box made from 2.5 mm thick ceramic board insulation (Cotronics Corp.). The probes are connected to an electronic load (BK Precision 8500) to measure the output voltage when a temperature difference is applied across the TEG device.

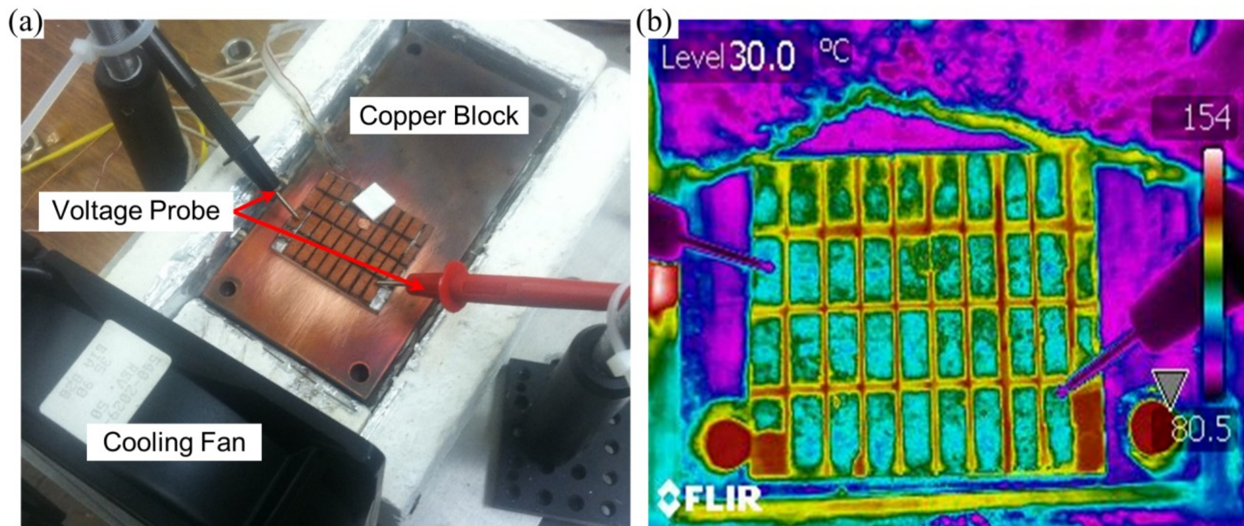

Fig. 5-7 (a) Test stand to characterize TEG and (b) measurement of topside temperature with an infrared camera

Accurate measurement of the hot and cold side temperature is critical to characterize the performance of the module. The hot side temperature is measured using a thermocouple and an infrared camera to obtain an accurate temperature estimate. In order to determine the temperature difference across the TE materials, a simple thermal resistance model is used. According to an analysis of the thermal resistors in Fig. 5-8, the temperature difference across the TE element

(ΔT_{TM}) can be calculated with equation 5-1, from the measured values T_H and T_C. The contact resistances across the interfaces of the different materials are neglected. The thermal resistance of each element is based on the material properties listed on Table 5-3.

$$\Delta T_{TM} = \frac{0.5R_{TE}}{2R_{Cu} + R_{YSZ} + R_{Al} + 0.5R_{TE}}(T_H - T_C) \qquad \text{(Eq. 5-1)}$$

For a temperature difference ΔT applied to a TM element, an external load is connected in series. The power generated by the TM is estimated from the voltage across the external load and the current in the circuit. This temperature difference across the TE element and is compared with the measured voltages and power output to estimate the performance of the device. The results are shown in Fig. 5-9.

Table 5-4 Thermal resistances of various elements across the TEG

	R_{Al}	R_{YSZ}	R_{Cu}	R_{TE}
L (mm)	3.00	0.30	0.50	1.40
κ (W/m·K)	68.3	2.5	160.4	6.5
R (K/W)	4.39×10^{-5}	2.80×10^{-4}	4.36×10^{-6}	2.15×10^{-4}

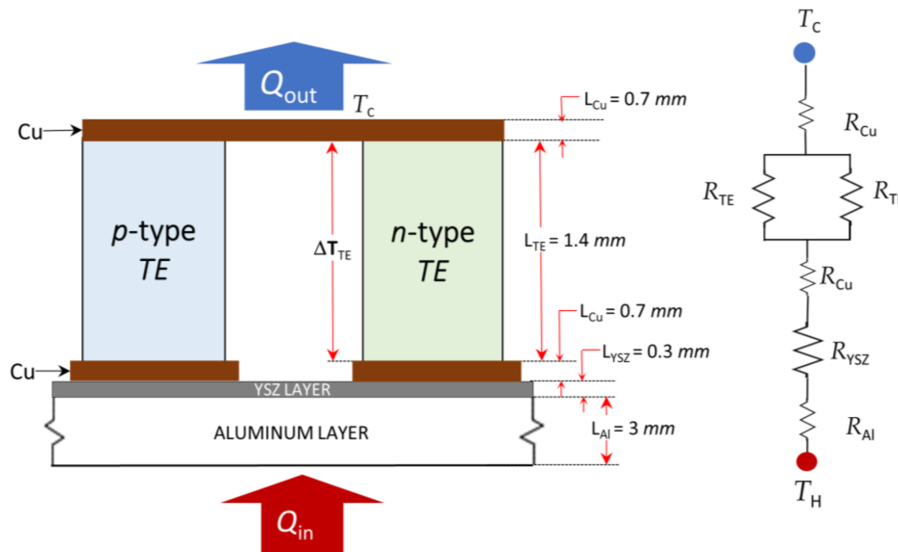

Fig. 5-8 Thermal resistor model of TE pair

Figure 5-9 shows the measured open-circuit voltage as a function of the temperature difference ΔT applied across the TE device (data points). The line represents the estimated open voltage as a function of temperature difference. The measured output shows the same trend as the prediction; although the actual values are 10-40% lower than the predicted values. The reason for the discrepancy may include the fact that the contact resistance between the elements was not included in the resistance network shown in Fig. 5-8, which would tend to reduce the overall heat flow through the device for a given applied temperature difference.

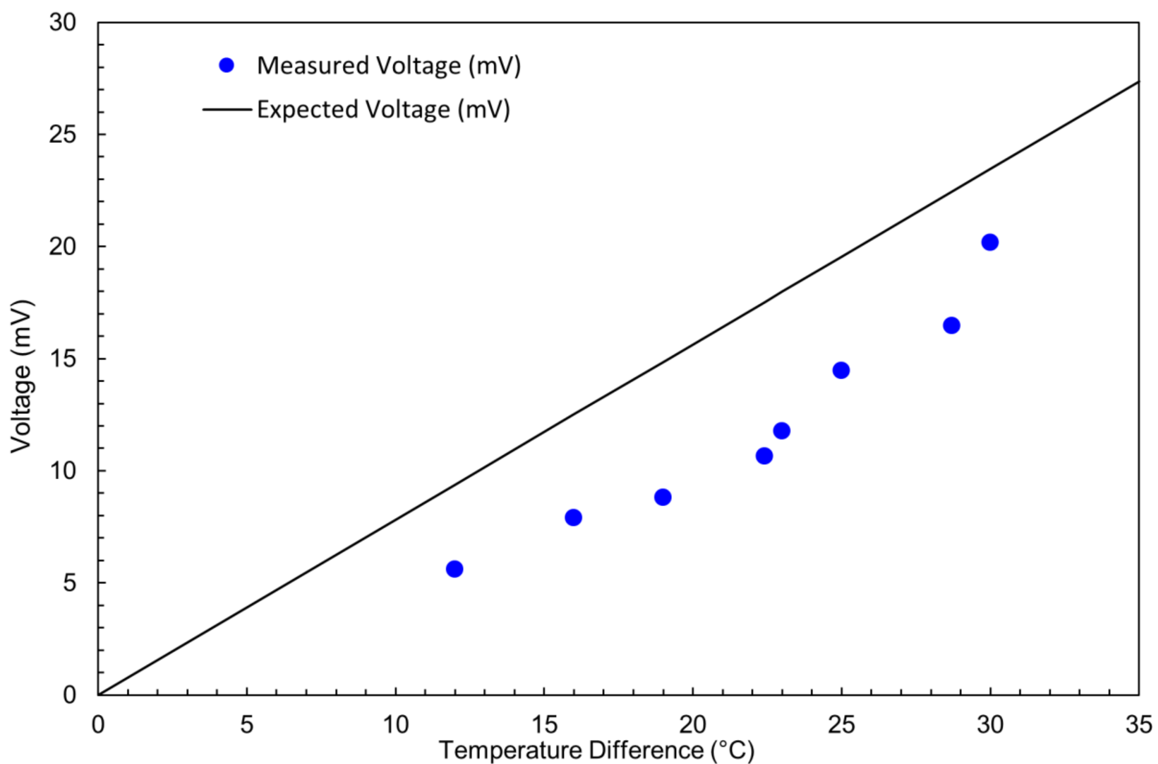

Fig. 5-9 Open-circuit voltage measured as function of temperature difference across the TE legs (ΔT_{TE})

One of the benefits of thermal spray is for the design of high-temperature devices that require electrode and brazing materials that can withstand evaporation, oxidation, interdiffusion, and maintain the adhesion strengths of the interfaces between the electrodes and thermoelectric

materials. For automobile systems, unlike stationary power-generating devices, repeated thermal cycling, and continuous vibration affect the reliability of the device. In this case, mechanical properties and the adhesion strength of the interfaces between the thermoelectrics and electrodes of the system very important.

5.3 Summary

This chapter presents the feasibility of using thermal spray and laser micromachining as a manufacturing method to fabricate thermoelectric generators directly onto engineering components. The manufacturing technology of the TEG module has been established. The steps required to fabricate a thermoelectric device are presented, including the formation of the bottom and top metallic layers and the thermoelectric legs using thermal spray and laser micromachining. The results from the characterization of a flat (50.8 mm ×50.8 mm) TEG module fabricated with this method is presented. The performance was found to be equivalent to the expected values based on material properties. In addition, it is found that the thermal spray manufacturing method with good interlayer contact reduces the contact resistance issues faced with commercial devices.

Chapter 6

Application of Ink-Dispenser Printing for Thermoelectric Devices

The application of thermal spray for the fabrication of TE devices was demonstrated in the previous chapter. One major drawback of the thermal spray process is spraying high-quality starting powders for the TE legs. In this chapter, the feasibility of ink dispenser printing to overcome this challenge is investigated. Dispenser printing is an ink-based direct-write technology that allows for on-demand printing of materials under ambient conditions. Inks include suspensions, slurries, and solutions of a variety of materials, including metals, ceramics, and organics. After deposition, these inks solidify due to evaporation, gelation, solvent-driven reactions, thermal curing or light curing to leave a deposit of the desired properties. This includes evaluating the materials and device requirements. The ink requirements vary depending on the printing technology employed, but the components of the inks typically consist of powders dispersed in liquid inks. Selection and characterization of conducting and thermoelectric materials is also important. The optimal parameters needed for a dispenser system are also determined. Additional advantages include minimizing waste, facilitating automation and allowing complex shapes to be created. Finally, the performance of printed TE materials is examined.

6.1 Materials for Ink-Dispenser Printing

Various types of functional printing ink types are available for different applications, including colloidal inks, nanoparticle-filled inks, fugitive organic inks, polyelectrolyte inks and sol–gel inks. Applications include electrically conductive adhesives (ECAs) [125, 126] used for printed electronics and thermal interface materials (TIMs) [127, 128] used for reducing interfacial thermal resistance. Developing printing techniques for TEG device fabrication including the functional TE legs and conducting layers presents a unique challenge. First is the selection of the appropriate formulation to develop functional inks from insoluble organic or inorganic materials dispersed in ink. Second, these materials must be developed from abundant, low-cost, high-performance and non-toxic materials. The thermophysical and transport properties of the cured inks should be as close as possible to the bulk properties of the starting materials. Finally, the ink has to have the requisite rheological properties to streamline the printing process. This determines the geometrical aspect of transferred inks such as thickness and aspect ratio.

Typical printable inks consist of active filler materials dispersed in a thermoset polymer binder as shown in Fig. 6-1. A thermosetting polymer consists of cross-linked polymer chains held together with strong chemical bonds that form a three-dimensional network that becomes rigid and stiff when cured [129]. Curing involves an irreversible chemical reaction process induced by heat or radiation. Thermosetting epoxy resins are typically used in commercial ECAs [130]. Fast curing inks and/or curing methodologies are needed to expedite the printing process. In this work, a Bisphenol-F epoxy resin and an anhydride-based hardener catalyzed with an imidazole derivative are used as ink. The typical ink formulation, curing times and curing profiles are well established. These resins have an isothermal curing temperature of 150°C [131].

Active thermoelectric inks can be formulated from high-performance Bi_2Te_3-based alloys. Conducting materials can be developed from metal filler particles such as silver or copper powders. There is an inverse relationship between the addition of powders to improve printability and the resulting functionality of the printed inks compared to the bulk material. Adding too much powder affects the viscosity of the ink and the properties of the final part. Several researchers have investigated this issue and developed ink formulations combinations that optimize printability and functionality [132]. The shape of the filler particles is also important. Flake geometries are preferred to spherical geometries since packing density is higher.

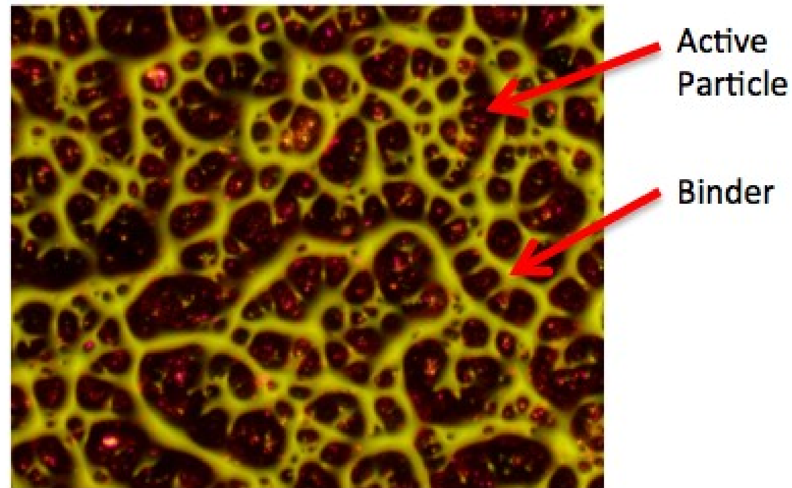

Fig. 6-1 Copper powders dispersed in polymer matrix

6.1.1 Printed Material Properties

The final printed materials consist of two distinct components, and the effective material properties will be a function of the constitutive elements. A well-known model used to describe the physical properties of two-component models called the Effective Medium Theory (EMT). This model is used for materials with a completely random distribution of the components [133]. It can be used to describe the resulting properties of printed composites [134]. The thermoelectric properties of the printed inks depend on the electrical conductivity, thermal conductivity, and Seebeck coefficient.

The electrical conductivity of the composite depends on the connectivity between the particles. If the percolation threshold is not met, the resistance of the printed materials will be very high [134]. The electrical conduction between the particles can also be limited by the presence of an oxide coating or limited contact area between the particles. The effective thermal conductivity is also similar to the electrical conductivity of composites. The thermally insulating characteristics of the polymer result in reduced thermal conductivity of the components. Introducing nano-inclusions is expected to lower the lattice thermal conductivity by intensifying the phonon scattering effect, thus enhancing their TE figure of merit ZT [135]. The addition of nanoparticles can improve the electrical and thermal properties. Both the electrical and thermal conductivities of the polymer composites containing nanoparticles could be greatly affected by the contacts of micro-sized particles and interfaces that involve nanoparticles along the conduction paths [130].

6.1.2 Curing and Sintering

The establishment of the functional properties results primarily from intimate contact between the active particles, caused by the curing shrinkage of the polymer matrix [136]. Thermal curing of inks also removes the solvents in the printed structures. However, thermal curing alone cannot achieve the optimal properties of the bulk materials. Sintering of the particles, which normally takes place at higher temperature ranges, is required for further improvement of the properties of the printed inks. Laser sintering is a unique solution for rapid consolidation of the suspended powders due to high local thermal gradients. In addition to the evaporation of the solvent, lasers can induce the removal of dispersants and binder materials by thermal decomposition and sintering through neck formation and grain growth [137, 138]. Therefore, the feasibility of laser sintering as a way to cure inks rapidly is studied. Based on the thickness of the deposited layers, laser selection must allow for sufficient thermal penetration for uniform sintering. Continuous wave lasers are the ideal

choice for thick deposits. On the other hand, pulsed lasers – high-frequency nanosecond lasers in particular – can be used be used for thermal penetration via the "heat accumulation" effect. They can be used to precision-tune laser-sintered features (e.g., sharpness and/or flatness of sintered patterns), to facilitate subsequent layer deposition/integration, and to improve overall device performance.

6.2 Device Challenges of Ink-Dispenser Printing

Ink-dispenser printing to fabricate TE devices uses inks that are deposited on a surface that contain materials that become the desired structure. Relative motion of the substrate in synchronization with on-off control of a dispenser can enable arbitrarily designated patterns to be deposited. In this way, patterning on cylindrical (non-flat) surfaces is similar to flat surfaces. Important factors considered for designing a dispenser system are the nozzle design, motion system, and control system. The nozzle type determines the size and shape of the deposit and the types of inks used (ink viscosity and fillers type). The motion system determines the accuracy and repeatability of the deposits, the maximum size of the deposit which can be made, and the speed at which deposition can occur. The control system design determines the rate, accuracy, and repeatability of dispensing as well as the speed at which deposition can occur. The distance between the dispenser tip and the substrate surface is important. The dispensing of high-viscosity ink (typically compatible with 10,000 cP or higher) is beneficial to achieve thick (or high-aspect ratio) thermoelectric layers, which are required to sustain a significant temperature gradient. High-viscosity inks also require a high-pressure dispensing system.

The synthesized inks are thoroughly mixed to form flowing solutions and then are printed. Usually, a solvent or 'vehicle', which later can be evaporated from the film, is used to tailor the

viscosity of the ink. High powder loadings are needed to ensure high part densities. For small nozzle diameters, particles sizes and agglomerates limit the loadings; lower powder loadings may be needed to operate at slightly lower viscosities. Significant effort is necessary to achieve homogeneous inks, and rigorous mixing sequences utilizing a combination of mechanical shaking and ultrasonication are needed.

Two printing strategies can be used to print various kinds of features: droplet-based and line based printing. Droplet-based features employ small droplets required for fine features, and final features are obtained by overlapping the droplets as shown in Fig. 6-2a. Line based printing strategies require thin line thicknesses to obtain fine features which can be varied by needle size and dispensing speed. Final features are obtained similarly by overlapping the lines as shown in Fig. 6-2b

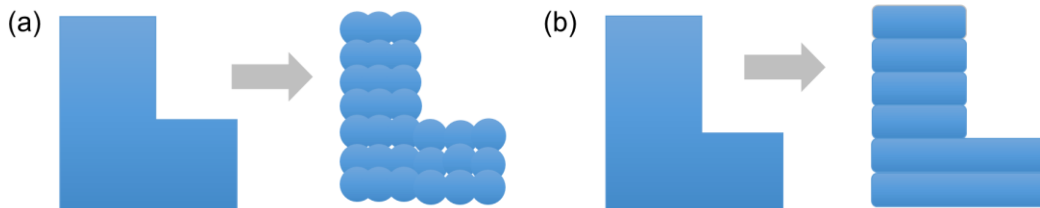

Fig. 6-2 Schematic representation of (a) droplet-based and (b) line-based printing strategies

6.3 Experimental Setup

6.3.1 Material Preparation

The conducting materials are made from copper powder (*Sigma-Aldrich*, US) with an average particle size of 12 mm dispersed in epoxy resin. The printable thermoelectric material was formulated from *n*- and *p*-type Bi_2Te_3 bismuth telluride powders (*Hi-Z Technology, Inc.*, US) dispersed in epoxy resin. The powders are vacuum hot-pressed and have an average particle size of

45 μm (325 mesh). The thermoelectric properties reported by the supplier are shown in Table 3-1. Silver nano-powders (*Sigma-Aldrich*, US), which were 150 nm and (>99.99%) are also used.

The epoxy resin used was EPON862 (*Hexion Inc.*, US), which is based on digly-cidyl ether of bisphenol-F (DGEBF). The hardener used was MHHPA (*Broadview Technologies, Inc.*, US), which is an anhydride based hardener. The thinner used was Heloxy 61 (*Hexion Inc.*, US), which is based on butyl-glycidyl ether, and the catalyst was AC-8 (*Broadview Technologies, Inc*, US.), which is a phosphate-based accelerator.

Table 6-1 As-Received thermoelectric properties for bulk Bi_2TE_3 powders

Property	*n*-Bi_2Te_3	*p*-Bi_2Te_3
Density [g/cm^3]	7.75	6.72
Seebeck Coefficient [μV/K]	-180	198
Electrical Conductivity [1/Ω·cm]	620	10^3
Thermal Conductivity[W/mK]	1.1	1.4

The inks are prepared in two steps:

1) *Formulation of Resins*: The resins for the printable inks were formulated based on the following procedure:
    a) a curing agent was mixed with the epoxy resin (the equivalent ratio of anhydride to epoxide was kept at 1:0.85);
    b) the mixture was stirred until a homogeneous solution was formed;
    c) after mixing, AC-8 (catalyst level was 0.2 parts per hundred parts of total resin) and the thinner (thinner concentration was ten parts per hundred parts of total resin) were added and mixed thoroughly.
2) *Formulation of Inks*: Copper and thermoelectric powders were added to the-the resin formulated above. The filler concentration of all inks was kept at 80% by weight. Ag nano-powders

in the ratio of 0.1% and 0.2% were also added to the inks, as needed. The mixture was premixed using a vortex shaker and then placed in an ultrasonic bath until a uniform paste was formed.

The thermoelectric inks were then printed from the same batch and cured at 250°C, 300°C 350°C and 400°C in a convection oven for 1-2 hours. Previous studies have described the effects of processing and optimization of these thermoelectric composite inks

6.3.2 Material Characterization

The changes in the physical properties of inks as a function of increasing temperature are measured using a Q500 thermogravimetric analysis (TGA) instrument (*TA Instruments*, US). The decomposition temperatures of the resin and the inks were determined. The curing behavior of the inks was determined using a differential scanning calorimeter (DSC) from TA Instruments, Model 2970. Dynamic scans were made on 10 mg samples at a heating rate of 5 °C /min, from 25–300°C. The samples were placed in hermetic aluminum DSC pans and scanned in a nitrogen purge gas. The temperature-dependent thermopower of the samples was measured on an SB-100 Seebeck measurement system (*MMR Technologies Inc*., US) under a vacuum environment (Appendix B). The temperature-dependent electrical resistivity was measured by the four-point probe method using a custom-built probe holder and an RM3000 test unit (*Jandel Engineering Ltd.*, UK). The temperature-dependent thermal conductivity of the bulk samples was measured by the laser flash thermal diffusivity (LFTD) method using DLF-900 (*TA Instruments*, US) in nitrogen purge gas. The equipment description is provided in Appendix A. The optimal curing conditions are determined from these measurements. Scanning electron microscope (SEM) images of dispenser printed thermoelectric materials cured at the optimum temperatures were also taken.

6.3.3 Dispenser Printing System

A dispenser system is designed and built to study the key parameters required in the ink-dispensing system. The setup includes a 3-axis motion stage used to print the inks with various speeds as shown in Fig. 6-3. A dispensing syringe was connected to a Musashi ML-606GX pneumatic controller capable up to a 500 kPa dispensing pressure. An air compressor is used to provide the dispensing pressure. The needle can be replaced depending on the ink-dispensing rate. The dispenser also has vacuum pressures up to –0.4 kPa to prevent the overflow of epoxy. Available needles sizes vary from an inner diameter of 1.753 mm to 0.152 mm (*Jensen Global, Inc*., US). A side-view camera is used to image the printing process on a substrate. A combination of several parameters determines stable dispensing. These include factors such as shot pressure, dispensing time, needle size, ink viscosity, and shot height.

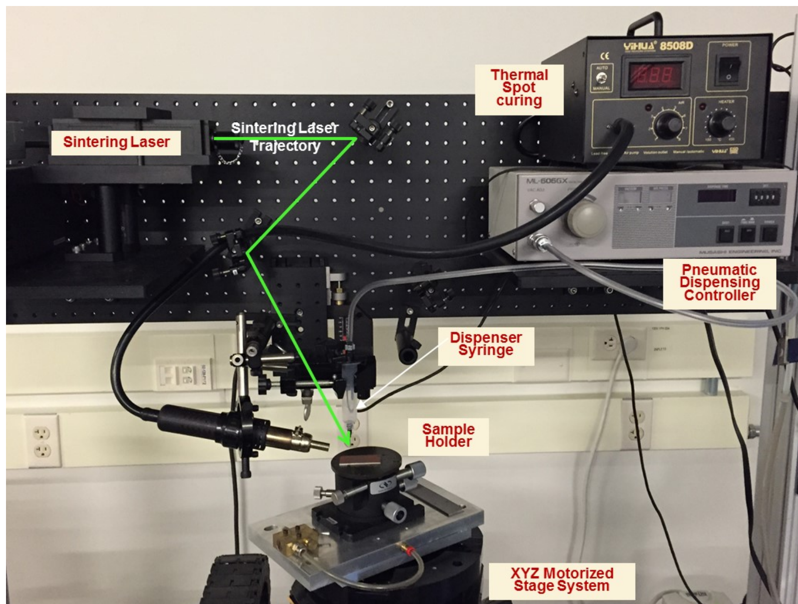

Fig. 6-3 Dispenser system setup

6.4 Results and Discussion

6.4.1 Phase Change and Microstructure

The changes in the physical properties of inks as a function of increasing temperature are measured using TGA. The results for the resin and as-received powders are shown in Figs. 6-4 thru 6-6. The decomposition temperature of the epoxy system was found to be 380 °C. This determines the maximum curing temperature of the epoxy with the removal of the binder. The maximum temperature of *n*- and *p*-type Bi_2Te_3 powders are 400°C and 450°C, respectively. The melting of Bi_2Te_3 is 586 °C, but Te-rich phases start to melt at 425°C. Therefore, the maximum temperature of a TE device fabricated with these powders is 400°C.

The curing profile for the epoxy resin measured by the DSC is shown in Fig 3-9. The epoxy resin is measured from 30-380°C based on the TGA measurements. An exothermic peak is observed at about 150°C indicating a catalyzed curing reaction for the epoxy resin. The DSC for the as-received Bi_2Te_3 powders is also shown in Fig 6-7. Endothermic peaks for the powders are observed at about 420°C.

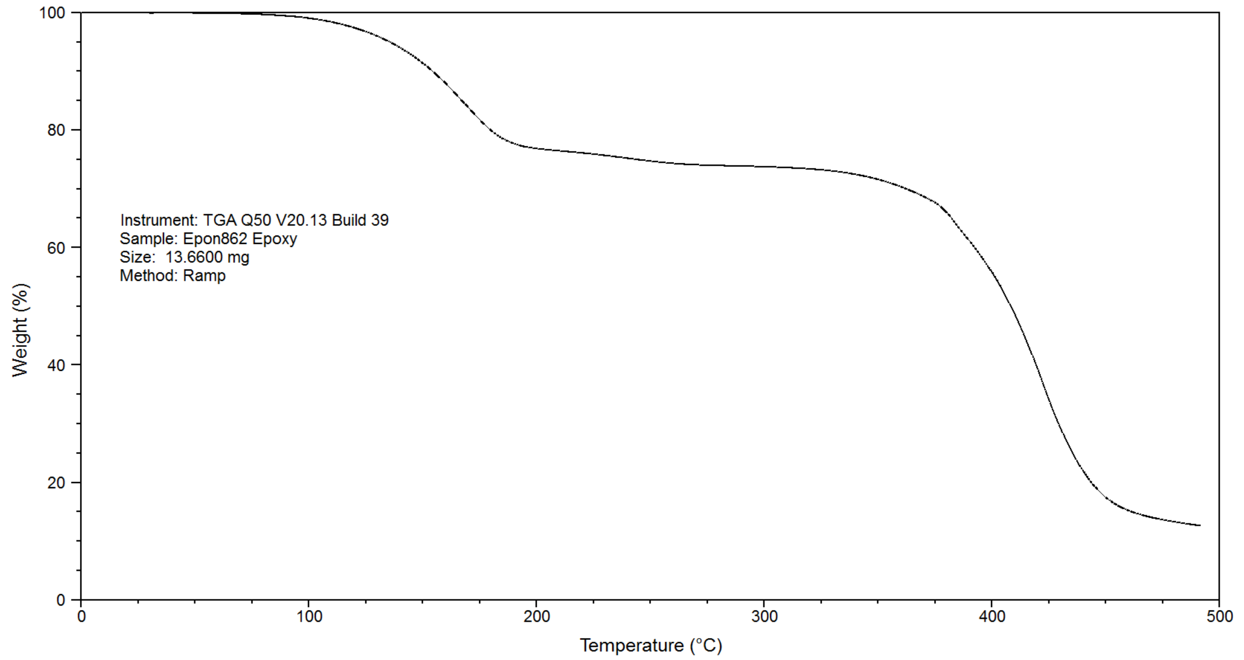

Fig. 6-4 TGA of epoxy resin.

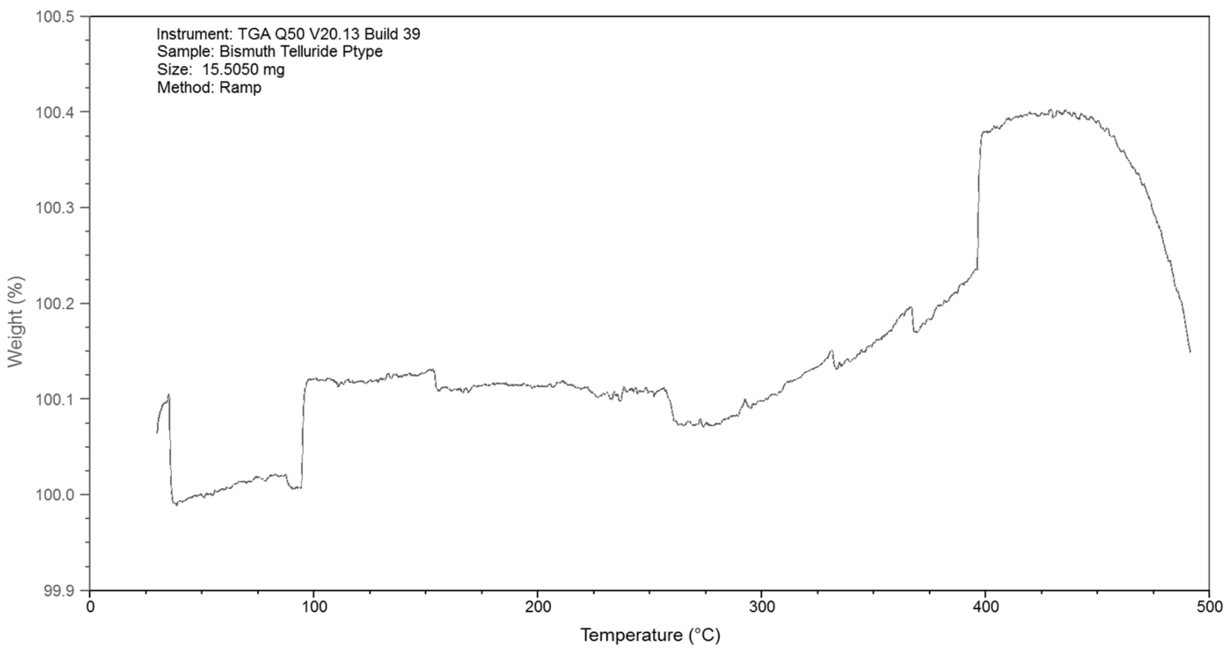

Fig. 6-5 TGA of p-type as received Bi_2Te_3 powder.

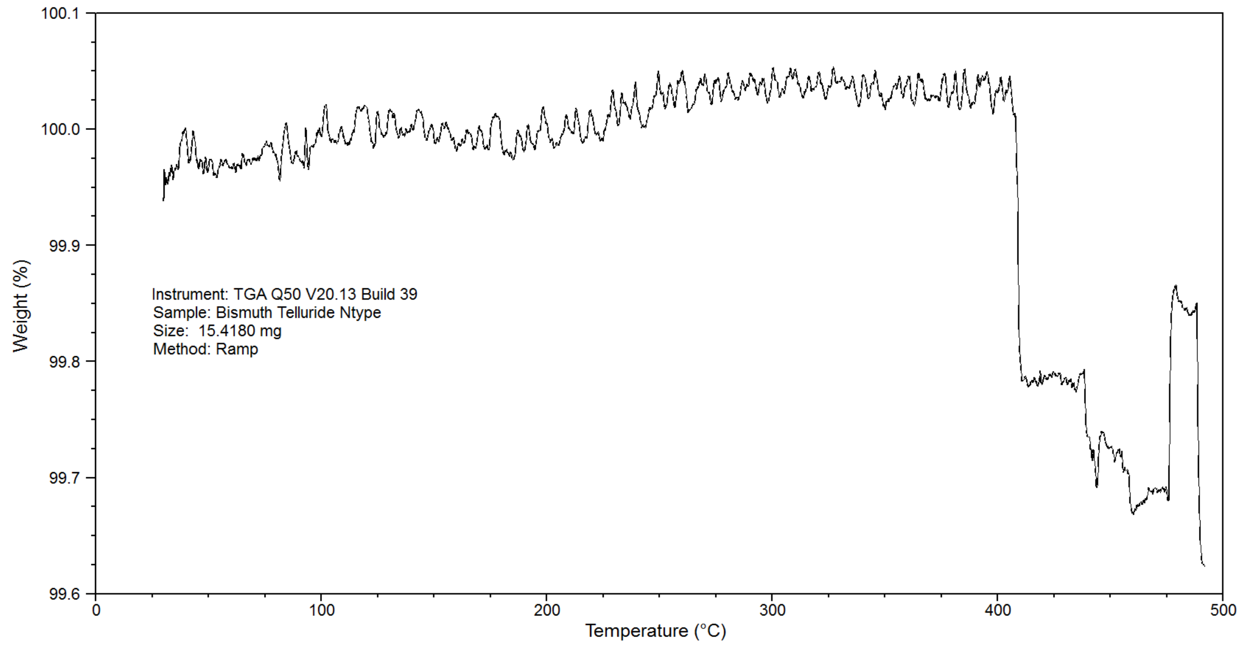

Fig. 6-6 TGA of n-type as received Bi2Te3 powder.

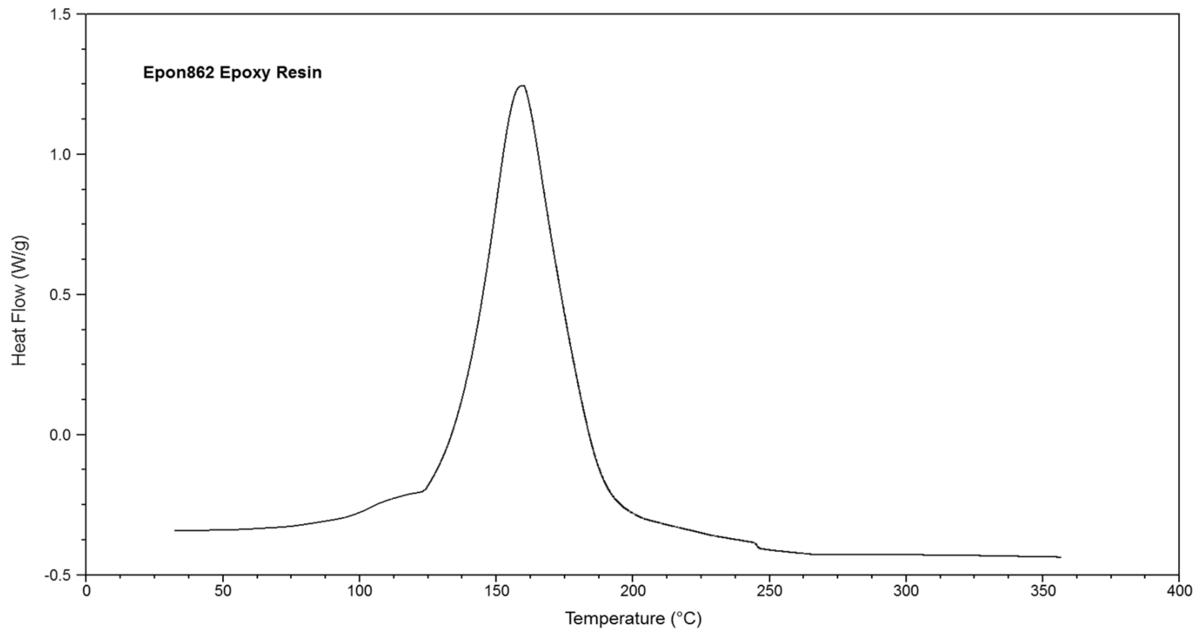

Fig. 6-7 DSC curves of epoxy resin

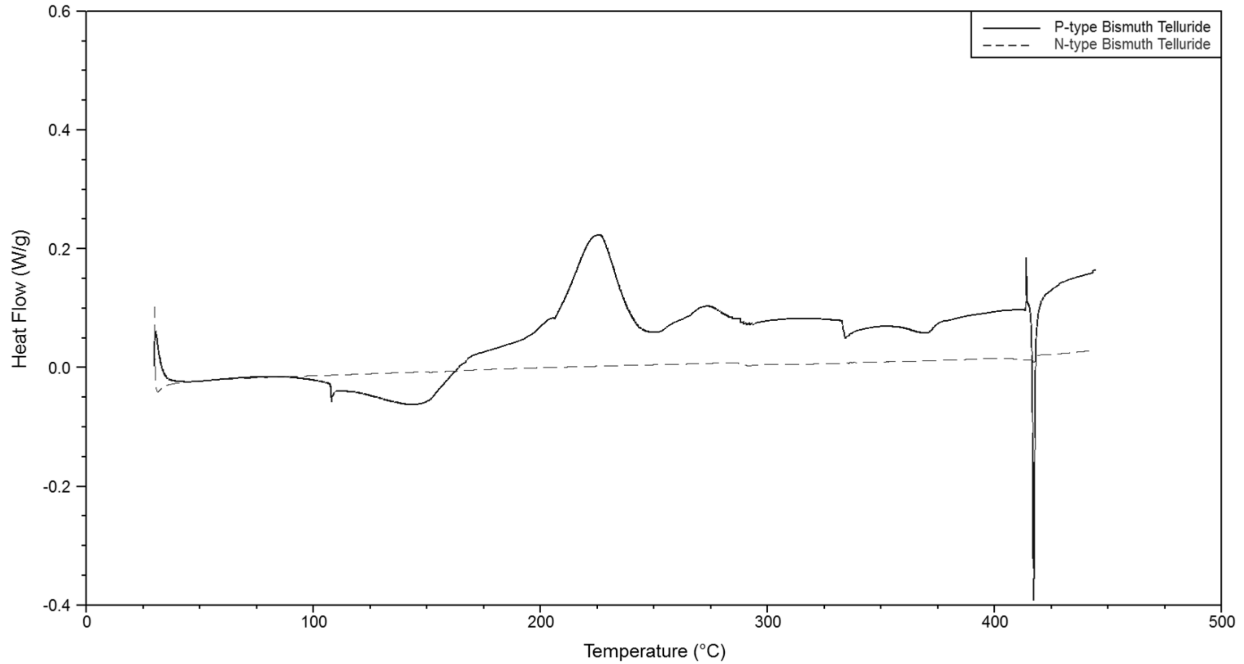

Fig. 6-8 DSC curves of epoxy resin

XRD studies using Cu Kα radiation were performed to characterize the sample crystal structures, scanned from $2\theta = 20^\circ$ to 80°. The XRD results of the *n*- and *p*-type Bi_2Te_3 powders as received are shown in Fig. 3-11. Comparing it to the ICDD powder diffraction file (PDF) for bismuth telluride (00-015-0863, Tellurobismuthite), a single crystalline phase can be identified indicating that the alloy sample was successfully synthesized.

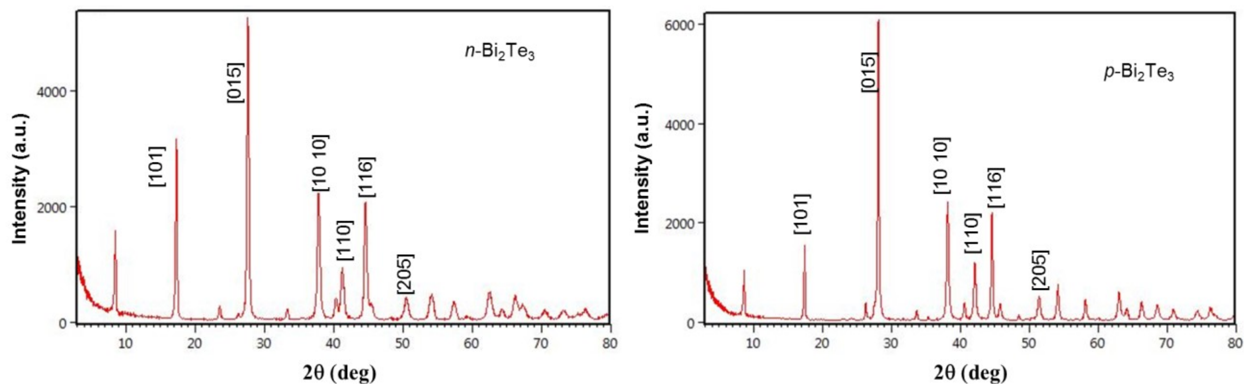

Fig. 6-9 X-ray powder diffractions (XRD) of the as-received thermoelectric powders.

6.4.2 Thermoelectric Properties

The temperature dependent thermal conductivities of *p*- and *n*-type Bi_2Te_3 cured at 200°C, 250°C, 300°C, 350°C and 400°C are shown in Fig. 6-10. The measurements were made using the laser flash technique. The thermal conductivities of composite systems are expected to be a function of all the properties of the individual material properties. The effect of curing results in the shrinkage of the epoxy resin tightly packing the particles. Sintering at higher temperatures promotes larger grain formation. The increasing trend of thermal conductivity with higher curing temperatures demonstrates this. The drop in thermal conductivity at 400°C results from the removal of the epoxy and the increased porosity of the material.

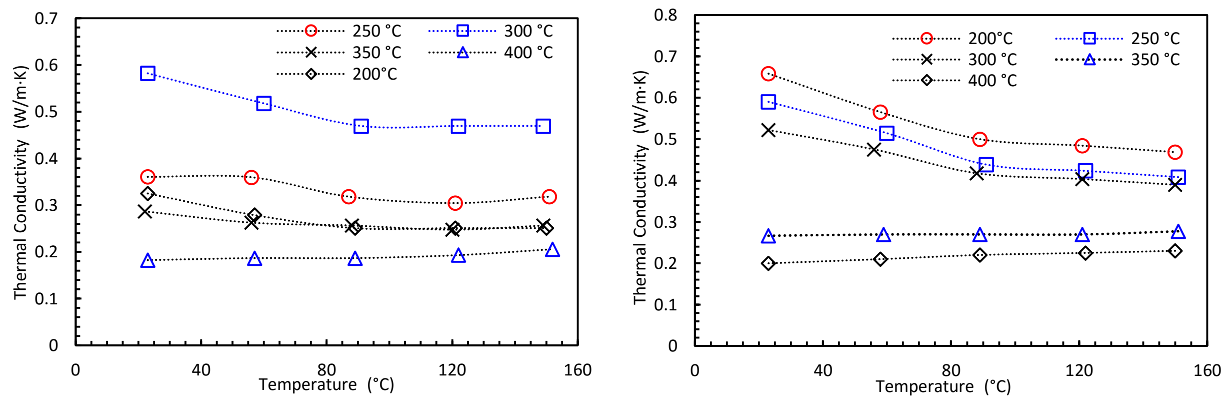

Fig. 6-10 Temperature dependence of through-thickness thermal conductivity measurements of n-type (left) and p-type (right) Bi_2Te_3 sintered at various temperatures.

The Seebeck coefficient (α) of printed *n*- and *p*-type Bi_2Te_3 materials cured at 250°C, 300°C, 350°C and 400°C are shown in Fig. 6-11. The peak value of the n-type materials was -300 μV/K when cured at 350 °C. This is higher than the bulk value of -180 μV/K the material reported by the supplier. Sintering of the *n*-type materials did not have a significant effect on the Seebeck coefficient except when sintered at 400°C. At this temperature, the polymer disintegrates reducing the Seebeck coefficient. The peak value of the *n*-type material was 220 μV/K when sintered at 250

°C, which is also higher than the bulk value of 198 μV/K. The increased Seebeck coefficient could be due to increased carrier concentration. The carrier concentrations and carrier mobility could be determined using Hall coefficient measurements, which was not performed in this work. Alternatively, it could be inferred from measurements of electrical conductivity. The electrical conductivity (σ) of printed *n*- and *p*-type Bi_2Te_3 materials cured at 250°C, 300°C, 350°C and 400°C is shown in Fig. 6-12. The electrical conductivities are less than the bulk sample due to the insulating characteristics of the polymer and increase with increasing sintering temperature. The high electrical conductivities and reduced Seebeck coefficients at a sintering temperature of 400°C indicate that high carrier concentrations are responsible.

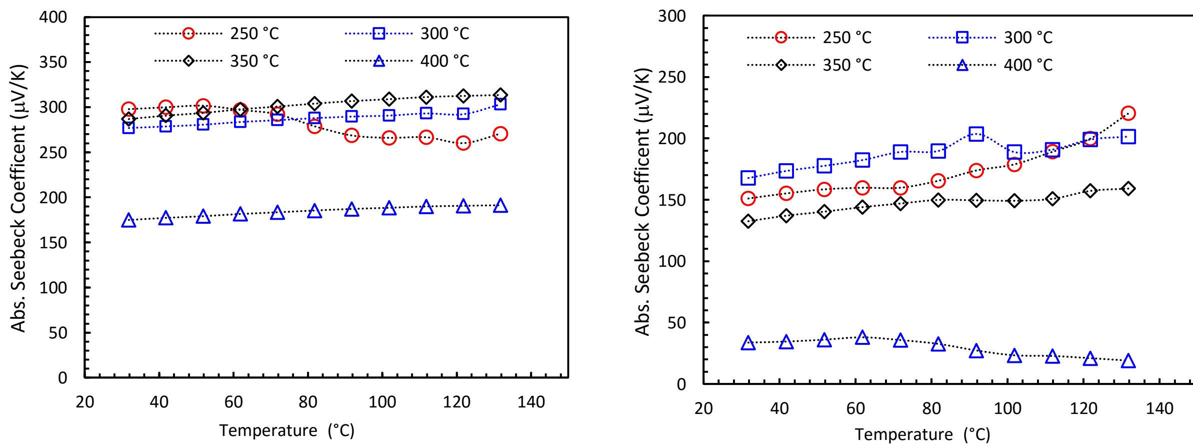

Fig. 6-11 Temperature dependence of Seebeck coefficient of n-type (left) and p-type (right) Bi_2Te_3 sintered at various temperatures.

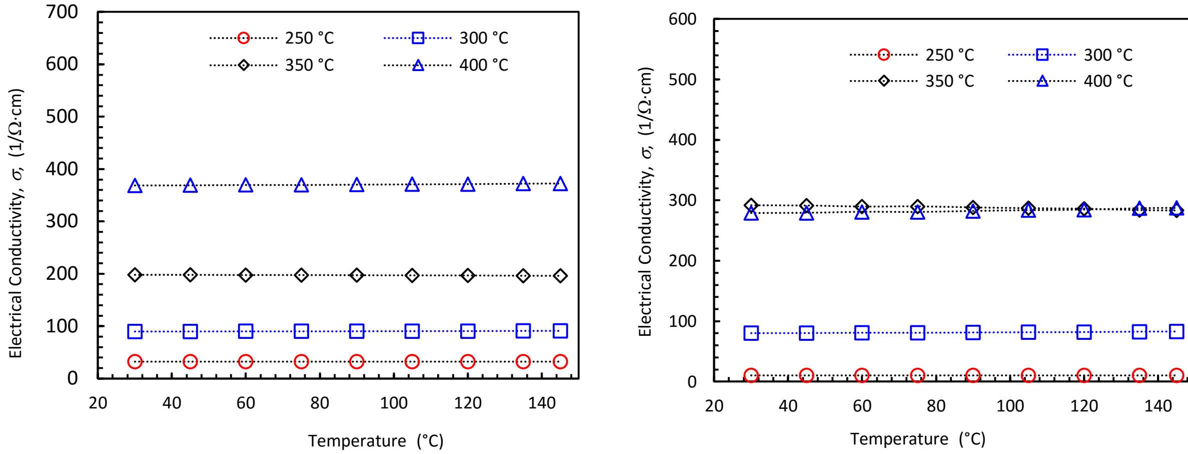

Fig. 6-12 Temperature dependence of electrical conductivity of n-type (left) and p-type (right) Bi_2Te_3 sintered at various temperatures.

Based on these measurements, a curing temperature of 350°C is found to be optimal. Fig. 6-13 shows the power factor and ZT of printed *n*-type and *p*-type Bi_2Te_3 samples cured at 350 °C. The maximum ZT values for the *n*-type and *p*-type material are 0.3 and 0.11, respectively. The SEM image of the *n*-type film cured at 350 °C is shown in Fig 3-16. The images suggest that the composite films are uniform and have low porosity.

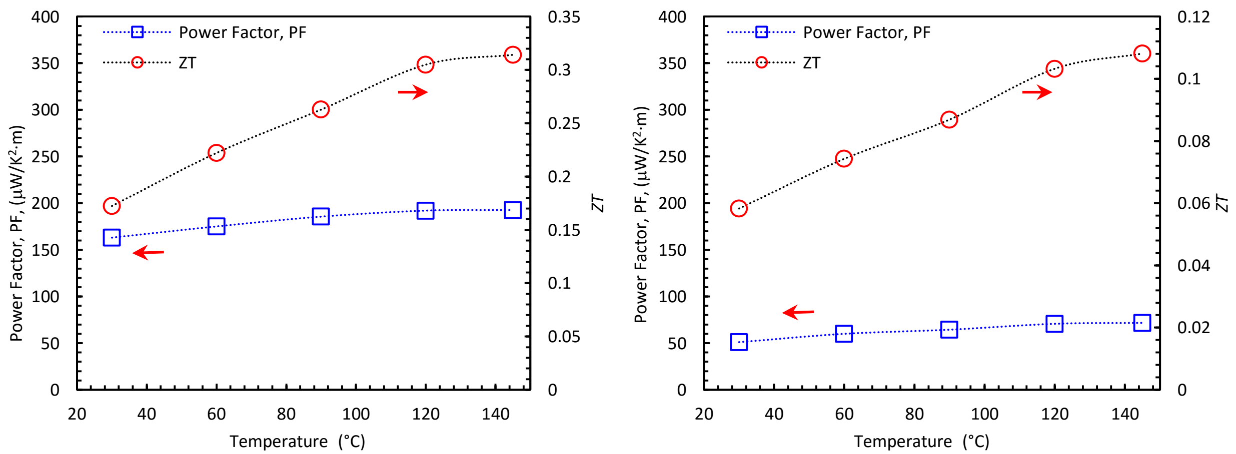

Fig. 6-13 Power factor and ZT of printed *n*-type (left) and *p*-type (right) Bi_2Te_3 sintered at various temperatures.

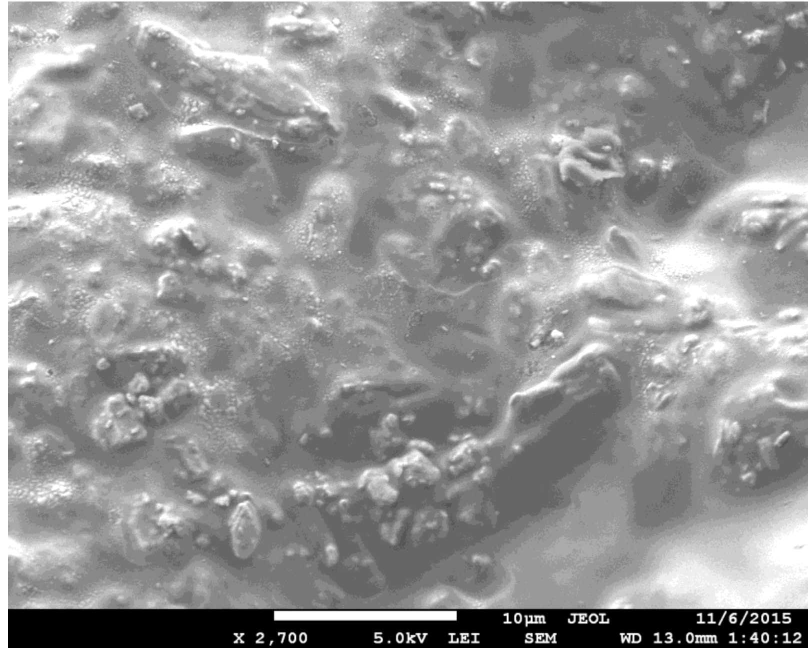

Fig. 6-14 SEM image of printed n-type Bi_2Te_3 cured at 350°C

6.4.3 Effect of nanoparticle addition

The thermoelectric properties of printed thermoelectric materials with the addition of Ag nanoparticles were also tested. The thermal conductivity, electrical conductivity and Seebeck coefficients measured as a function of temperature are shown in Fig. 6-15 thru 6-17. It can be seen that the effect of nanoparticles results in increased thermal conductivity. This is contrary to what is expected in the literature [135]. However, the addition of nanoparticles increases the electrical conductivity by a factor of two. The Seebeck coefficient is slightly decreased. The microstructure of the sample with the addition of Ag nanoparticles is shown in Fig 6-18.

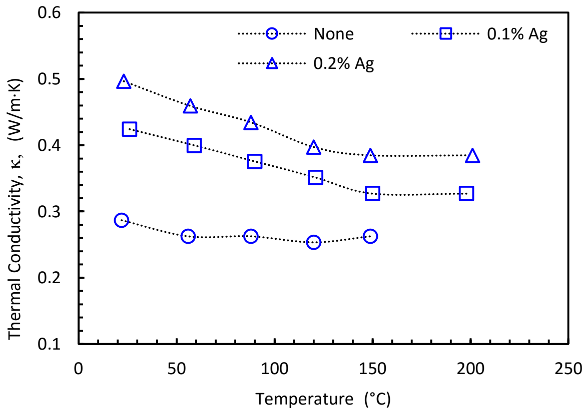

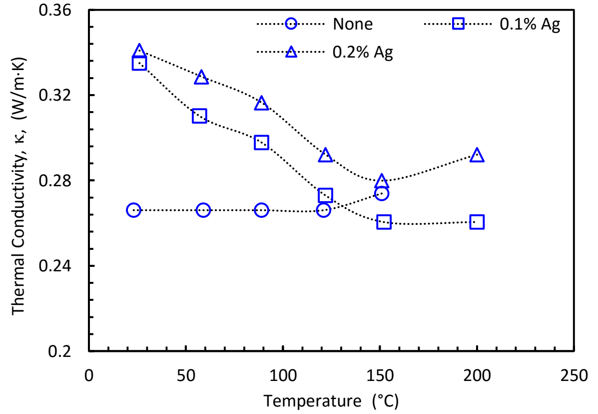

Fig. 6-15 Temperature dependence of in-plane thermal conductivity of *n*-type (left) and *p*-type (right) Bi_2Te_3 with 0.1% and 0.2% Ag nanoparticles sintered at 350 °C.

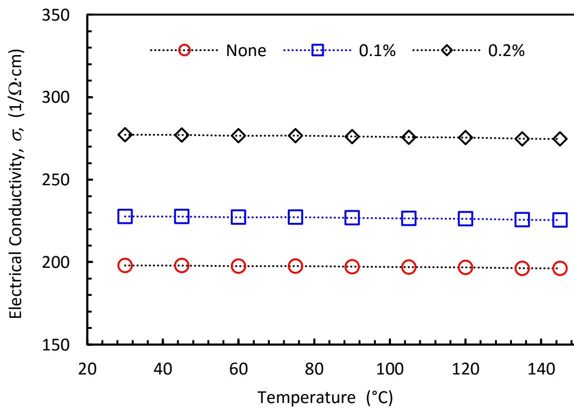

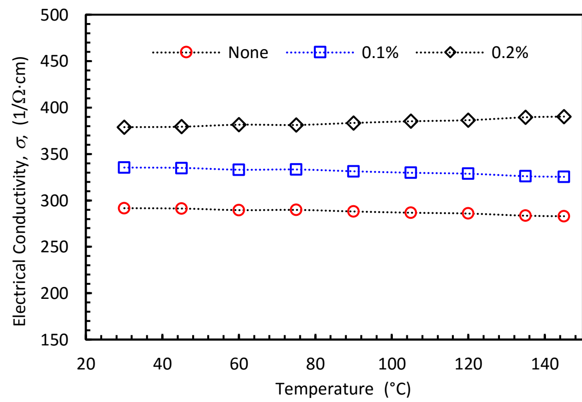

Fig. 6-16 Temperature dependence electrical conductivity of *n*-type (left) and *p*-type (right) Bi_2Te_3 with 0.1% and 0.2% Ag nanoparticles sintered at 350 °C.

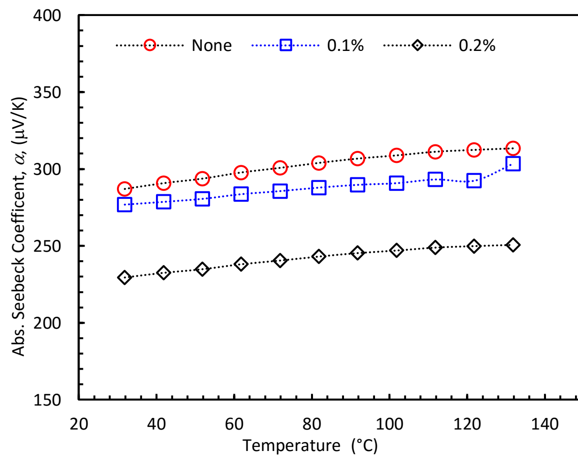

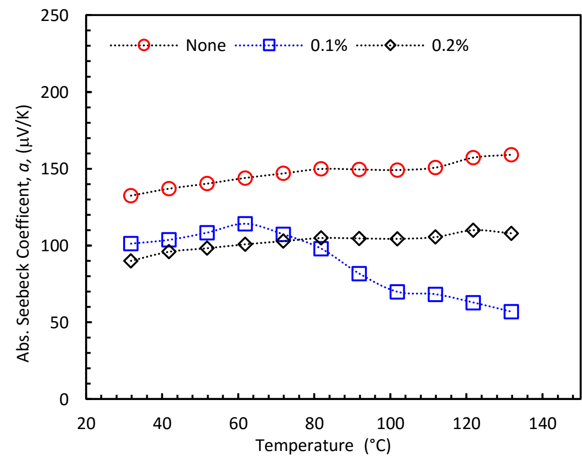

Fig. 6-17 Seebeck coefficient of *n*-type (left) and *p*-type (right) Bi_2Te_3 with 0.1% and 0.2% Ag nanoparticles sintered at 350 °C.

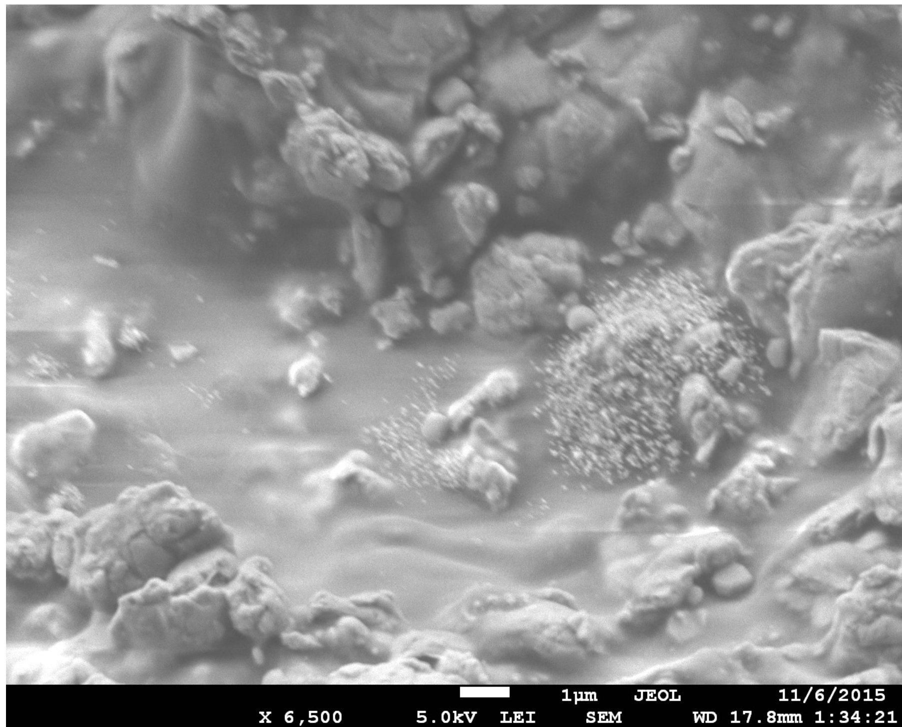

Fig. 6-18 SEM image of printed *n*-type Bi_2Te_3 with 0.2% Ag cured at 350°C

6.4.4 Ink Dispensing System

The pneumatic dispensing system was tested for three different needle sizes and different dispensing pressures as shown in Fig. 6-19. The needle gauge sizes were 22, 25 and 27, which correspond to inner diameters of 0.508 mm, 0.304 mm and 0.229 mm, respectively. The shot height, which is the distance between the needle tip and the surface of substrates, was 2.5 mm. Droplets of ink were printed as a function of dispensing pressure and visualized from the side with a camera. The printed droplet widths were measured after printing to determine the effect of the dispensing pressure. It can be seen that the droplet widths were much larger than the needle sizes. Various other parameters such as the shot height and dispensing time were also varied to obtain smaller droplet sizes. It was observed that the droplet widths were limited due to wetting of the inks on the substrate. Therefore, the droplet printing strategy was abandoned.

Line printing was also optimized in a similar fashion. Since the volume flow rate of ink from the needle to the substrate is constant at a specified pressure, the printing speed is the best parameter to control the line thickness. Fig. 6-20 shows the printed line thickness as a function of dispensing speed for the 27-gauge needle at 500 kPa. It can be seen that lines up to the same thickness as the needle can be printed at higher speeds. Line thickness smaller than the needle size cannot be printed due to a reduced flow rate. Fig. 6-21 shows the similar trend for 25-gauge needle size.

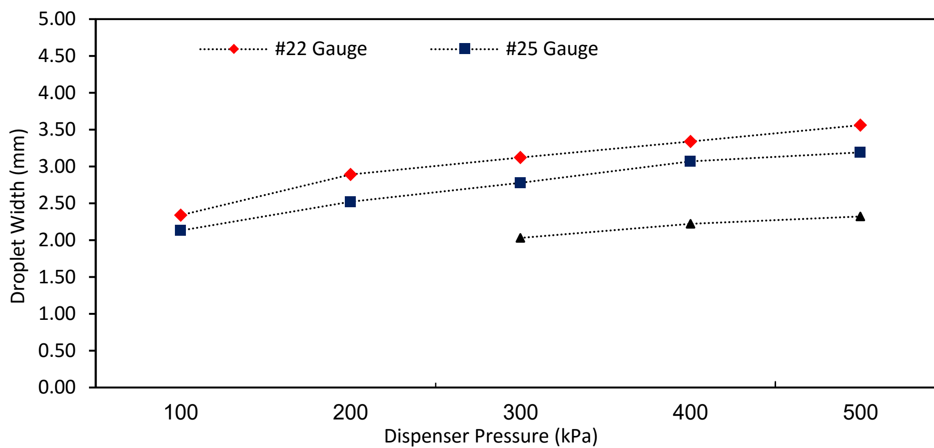

Fig. 6-19 Printed droplet width as a function of dispensing pressure

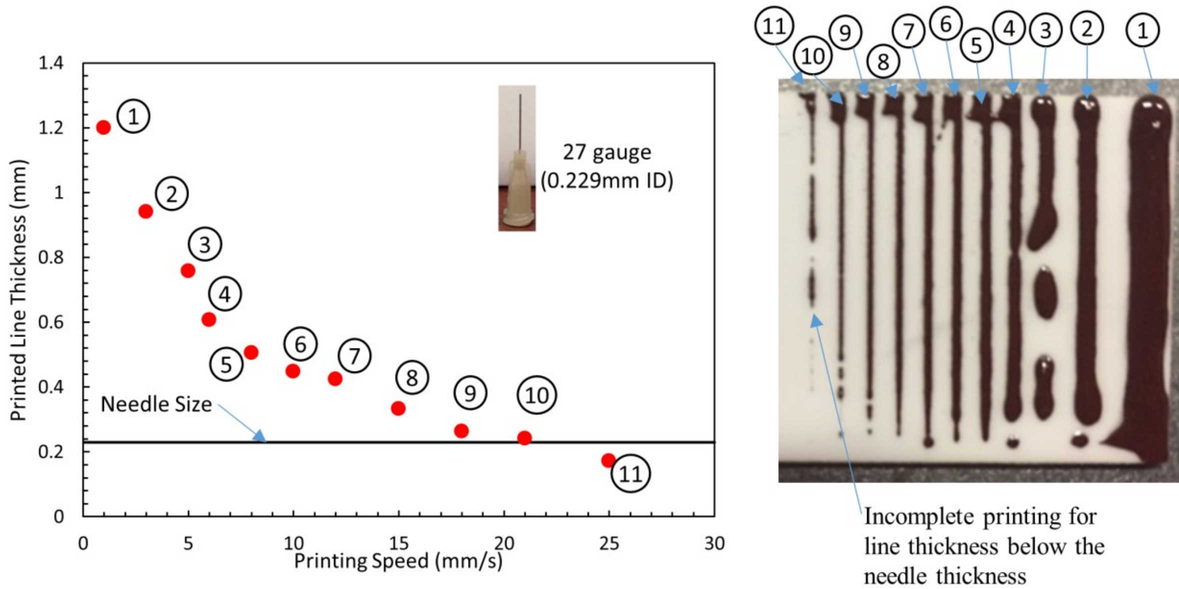

Fig. 6-20 Printed line thickness as a function of dispensing pressure for 27 gauge needle

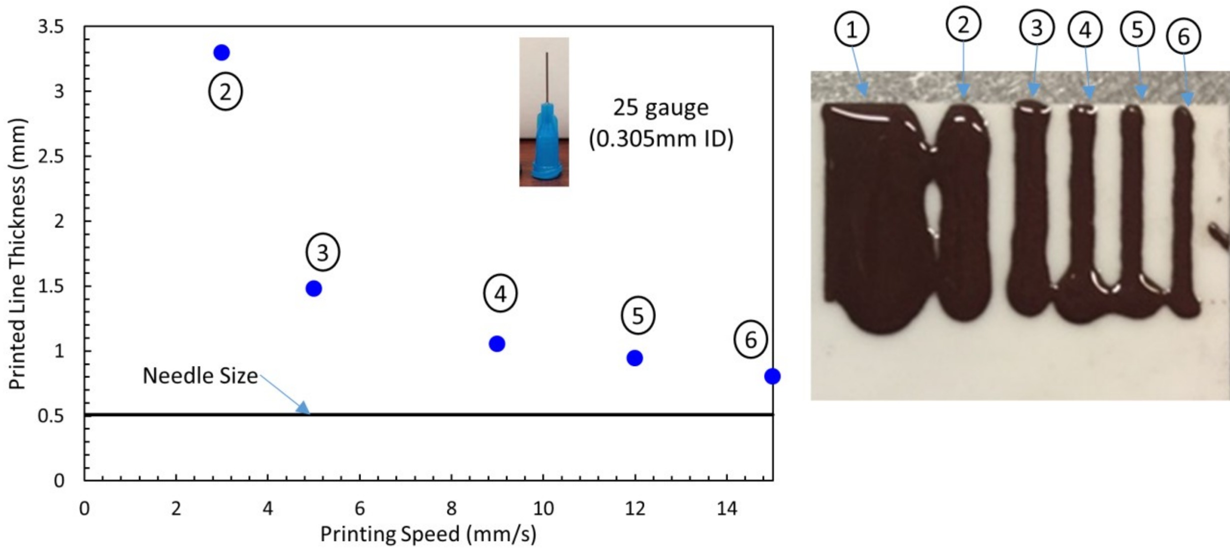

Fig. 6-21 Printed line thickness as a function of dispensing pressure for 25 gauge needle

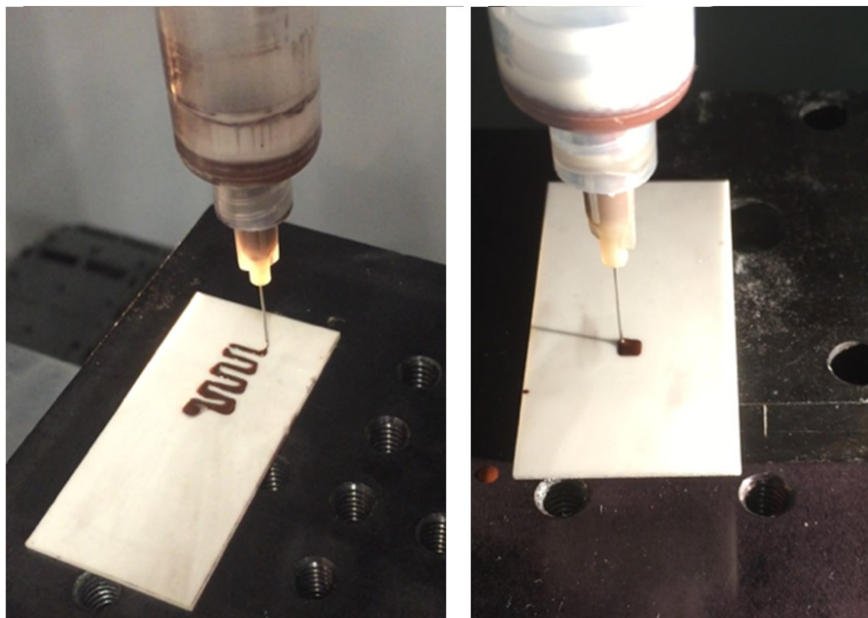

Fig. 6-22 Dispenser printing of features using line based printing strategy

Further experiments can be performed to understand other variables in dispenser printing including printing speed, accuracy, and sample sizes. While the experiments were performed for specifically controlled variables, the resulting trends can be interpreted for different material systems. One difficulty that was experienced with the dispenser printing process is the time it takes for the

solvent to evaporate and cure the epoxy. Laser sintering studies were done to provide rapid curing as a separate study but were not integrated into the printing system for in-situ testing. In addition, depending on the particle size of the powder, separation between epoxy and powder can occur resulting in clogging of the needle. This effect can be minimized by using smaller particle sizes, but cannot be eliminated.

6.5 Summary

In this chapter, the feasibility of dispenser printing as a technique for the fabrication of high-quality TE materials has been demonstrated. Printable thermoelectric materials were first synthesized in the form of inks, which consist of active powder materials dispersed in a suitable epoxy resin used as a binder. Thermophysical properties of the printed materials were measured as a function of curing temperature and were demonstrated to have high thermoelectric performance. The thermal conductivity of the printed materials was very low due to their composite nature. The Seebeck coefficients of the printed materials were found to be similar to that of bulk materials while the electrical conductivity was low. The addition of silver nanoparticles increased the electrical conductivities but reduced the Seebeck coefficients canceling out the overall improvement in ZT. Hall-effect measurements are needed to explain these results fully, but it can be inferred that the primary reason is increased carrier concentration due to the addition of metal nanoparticles. The maximum ZT values for the n-type and p-type material are 0.3 and 0.11, respectively. Dispenser printing strategies were also developed. The printed feature sizes depend on the needle size, which can range from 200 μm to 1 mm. The optimum printing variables such as ink, viscosity, pressure, shot height and shot spacing on feature sizes were determined.

Chapter 7

Waste-Heat Energy Harvesting Applications for TEGs

7.1 Overview

Waste-heat is an abundant source of energy (with *low exergy*) arising from thermodynamic limitations on energy conversion processes and equipment. Waste heat is ubiquitous in industrial, commercial and residential settings. Examples of waste-heat sources include combustion exhausts, process off-gases, cooling lines, conductive losses from equipment and heated products. Even recovering a small percentage of this energy can provide valuable power for many different applications. Thermoelectric generators are thus potentially useful for waste-heat energy harvesting applications.

TEGs can provide usable power for sensing and actuating applications, especially in harsh environments, e.g., nuclear power plants. Such an application is investigated using commercially available TEG modules. In this chapter, aspects of a TEG-based waste-heat recovery system for sensor applications in a Small Modular Reactors (SMR) are presented. Such a system typically consists of TEG modules mounted on a hot engineering component with an integrated heat removal mechanism to provide the required temperature difference. It also includes requisite electronics needed to condition the power output and a battery to store and save the power for later

use. The power produced depends on the temperature gradient, system design, integration method and available heat sink. A prototype TEG based sensor that attaches to a steam pipe is designed, and a prototype is manufactured as a demonstration.

The characterization of a TEG module is an important step in the design of a TEG-based waste-heat recovery system. It enables the proper design of the power management system and allows for the prediction the voltage and power generated for different temperature gradients, as well as, the internal electrical resistance of the TEG. The design can also be evaluated as the percentage of the total available power that is extracted with the converter. Results from the characterization of commercial TEG modules on a custom-built test stand are presented.

7.2 TEG-based Sensors for Small Modular Reactors

The application of the TEGs in waste heat energy harvesting of Small Modular Reactors (SMRs) has been demonstrated. The main emphasis of the work thus relies on the application of the design and manufacturing of the TEG system for a hot pipe component for different temperature ranges. This work aims to develop electrically autonomous sensing and actuation devices, to be used during normal and off-normal conditions on process piping and components for Small Modular Reactors (SMRs). The first principle behind this work is the use of thermoelectric generators (TEGs), placed on thermally radiating reactor components (pipes, pump housings, heat exchangers or reactor vessels), to capture waste heat and produce usable electrical power via the Seebeck effect. The power produced is used to power sensors and electronics that relay critical plant information to operators and emergency crews. Surplus power can also be stored in batteries or supercapacitors for emergency actuation of valves or other plant equipment.

Nuclear energy can play a significant long-term role for meeting the world's increasing energy demand, which is projected to grow at an annual rate of 2.5% through 2030 [139]. Nuclear power plants have advantages over fossil-fueled plants in most areas of environmental effects and the cost of electricity but have the potential for accidents with more severe public consequences. Nuclear power plant accidents can be initiated due to *internal* events (e.g., random failures of plant equipment, operator errors) or *external* events (e.g., earthquakes, fires) [140]. They can be devastating to the environment and human health, especially if initiated while the reactor is at full-power operation. Such accidents (Chernobyl, Three Mile Island, and Fukushima Daiichi) have been major obstacles to the growth and development of nuclear power.

A common feature of all major nuclear power plant disasters is the loss of offsite power. The offsite power supplied from the electric grid is the primary power source during normal operating conditions. When a plant loses offsite power source (because of weather, plant, grid, or switchyard-related events, etc.), emergency power generators provide backup, onsite, alternating current (AC) power to essential buses. From 1997 to 2004, a total of 42 separate power-out conditions have been recorded in the U.S [141]. Among these incidents, 24 caused critical operation conditions, and 18 resulted in a plant shutdown condition. Losing of both off-site and on-site emergency power results in a station blackout, a dangerous condition where there is a complete loss of AC electrical power to the essential and nonessential switchgear buses in a nuclear power plant. Because many safety systems required for decay heat removal from the reactor core are dependent on AC power, the consequences of a station blackout could be a severe core damage accident [142]. The Fukushima Daiichi resulted in a station blackout because the tsunami disabled both the offsite power and emergency backup diesel generators.

There is an enormous amount of waste heat available in a nuclear power plant. TEGs are a viable means of converting low-grade heat energy into usable electrical power to drive a sensor network for monitoring and low-power actuation in station blackout conditions. The concept is to integrate multiple TEGs with power management circuits, sensors, microcontrollers, wireless transmitters, batteries, and possibly even actuators and installing them on steam pipes or other high-temperature components. Fig. 7-1 shows an overview of the concept. During normal conditions, the TEG-based device will store electrical energy into batteries. During off-normal condition, they gather and deliver important parameters wirelessly.

This application targets SMRs that offer a simpler, standardized, and safer modular design. They are factory built and can be installed incrementally at the point of use where there are shorter construction times and a smaller initial capital investment. SMRs have many enhanced safety features. They are designed for underground installation with seismic isolators. The likelihood that a station blackout will progress to core damage or core melt is dependent on the reliability and capability of decay heat removal systems that are not dependent on AC power [142]. As a result, SMRs are designed with advanced passive safety response for various incidents such as passive heat removal systems that utilize natural convection and gravity-assisted cooling to ensure that the reactor remains safe even under severe accident conditions. Most small reactor designs can accommodate easy removal of reactor core decay heat using fully passive, natural convection air ventilation systems [143].

An important support system in nuclear power plants is the DC power supply needed for instrumentation and control. During a station blackout, unless special emergency systems are provided, the battery-charging capability is lost resulting in the complete loss of the plants standard

monitoring capability. Losing instrumentation and control can place significant constraints on the ability of operators and emergency crews to cope with a station blackout. Lack of quantitative information about critical plant parameters such as pressure, temperature, and radiation levels are essential to understanding the status of the reactor and the entire plant. Additionally, during a station blackout, there may be a need to operate some pneumatic valves, such as a steam dump valve. Because AC power is not available, the station air compressors will be lost [142]. In such a case, at the minimum, it is vital to maintain continuous monitoring of the plant at all times.

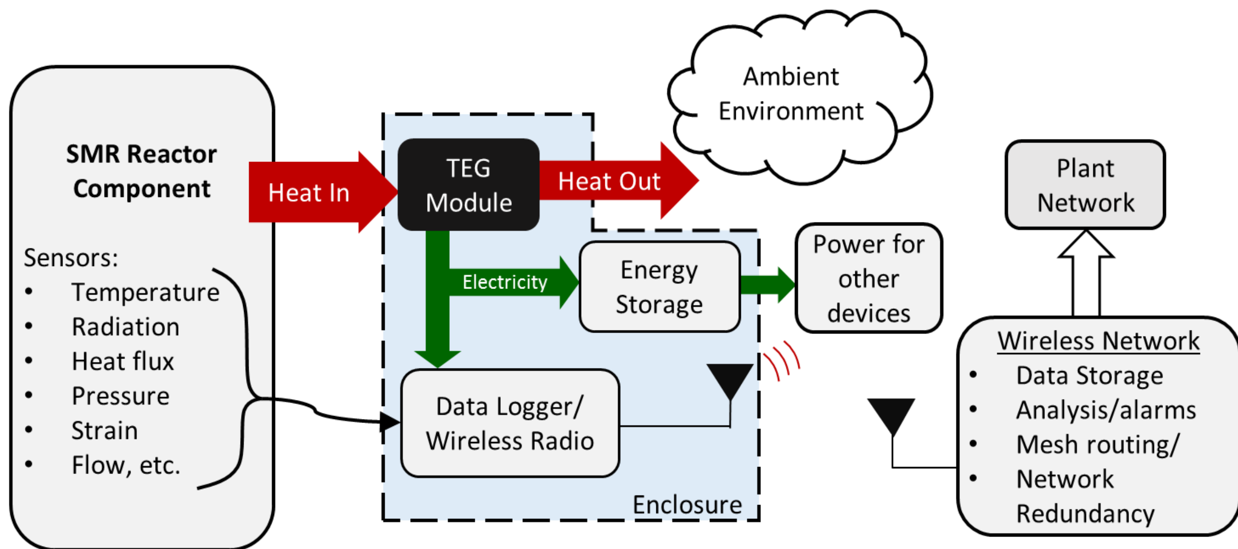

Fig. 7-1 TEG based sensing and actuation during normal and off-normal conditions

To determine the best location to deploy the TEG assembly, a comprehensive survey of possible heat sources, along with their temperatures, was conducted. We have reviewed all of the current SMR designs found in the Advanced Reactor Information System (ARIS) database, which is maintained by the International Atomic Energy Agency (IAEA) [144-146]. There are currently eight proven SMR designs ready for commercial deployment, and about twelve advanced SMRs designs have reached a stage where they could be implemented as prototype plants before 2020 [144].

There are three major groups of SMR designs depending on the cooling technology employed. The first and most common group of SMRs is based on the design concepts of proven and widely utilized Pressurized Water Reactors (PWRs). A representative example of the SMART (*Korea Atomic Energy Research Institute, South Korea*) SMR which is a 330MWt integral type PWR that can be used for cogeneration, district heating and seawater desalination as well as electricity generation [147]. Other notable PWRs include KLT-40S (*OKBM Afrikantov, Russia)* and mPower (*B&W and Bechtel Power Corp., U.S.*). The second group consists of liquid metal reactors (LMR) that are cooled by liquid metal or liquid salt. Examples include 4S (*Toshiba, Japan*) and PRISM (*General Electric-Hitachi, U.S.*).The third group of SMRs is gas-cooled reactors (GCR). Examples of GCR using Helium currently under development include HTR-PM (*Institute of Nuclear Energy and New Technology, China*) and Prismatic HTR (*General Atomics, U.S.*) [148].

Table 7-1 Core and steam generator inlet/outlet temperature in SMRs [146]

SMR Type	Reactor Name	Capacity [MWe]	Core Coolant Inlet/Outlet (°C)	Steam Gen. Inlet/Outlet (°C)
PWR	KLT -40S	35	280/316	170/290
	SMART	100	296/323	200/298
	mPower	125	297/321	163/300
LMR	4S	10	355/510	210/453
	PRISM	311	-/480	-/400
GCR	HTR-PM	211	250/750	260/566
	Prismatic HTR	350	322/750	193/541

Candidate locations of interest are the reactor vessel, reactor coolant inlet and outlet pipes, steam generator inlet and outlet pipes, heat exchangers and condensers. Table 7-1 provides the capacity, core coolant and steam generator inlet and outlet temperature for the different types of SMRs listed above. Commercially available TEGs are rated for use within certain temperature ranges, based on the type of thermoelectric material used and the layout of components (such as

interconnects and conducting wires). As a result, a temperature of 300 °C is considered as a minimum for the target location considered.

PWRs are designed with reactor coolant inlet and outlet pipe temperatures of between ~300-350 °C and steam generator inlet and outlet pipes temperatures between ~160-300 °C. These pipes represent nearly ideal installation locations for TEG-based sensor packages. In LMR and GCRs, inlet and outlet temperatures of the reactor core coolant pipes are much higher, between ~500 and 700°C. These temperatures are quite high. They would require heat exchangers to reduce them to acceptable values. The steam generator outlet pipes with temperatures around 500 °C are also possible locations for installation of a TEG assembly.

There were several important considerations taken into account during the design phase of this TEG-powered sensing system: the location and temperature of the available heat source, expected electrical loads, external ambient temperature, heat transfer losses, spatial constraints, and expected heat sink temperatures. A careful review of all pertinent parameters was used to design an integrated TEG-powered sensor. Selecting a location for the TEG system was subject to numerous design constraints. It was critically important to select a heat source within the feasible temperature range (> 300 °C) so that the temperature gradient could be designed to meet optimization requirements for the TEG arrays. Commercially available TEGs are rated for use within certain temperature ranges, due to the type of thermoelectric material used and the layout of components such as interconnects and conducting wires. The heat source must also be safely accessible for installation and must be in a location where the TEG system would not be harmfully invasive. Some sensitive locations, such as the reactor core, provide sufficient heat but preclude the use of TEG systems because the installation process itself may risk damage to the structure of the nuclear

reactor. Spatial constraints dictate that there must also be enough space available for bulky components such as the heat sink. The location must also be close enough to the main reactor to sense the running parameters of the reactor. These constraints collectively narrow down possible locations for the installation of TEG sensing systems.

The cumulative electrical load on the thermoelectric generators is comprised of the sensors, power manager, signal conditioner, microcontroller, and wireless transmitter. The power management circuit consists of an AC/DC converter, which is used to maintain power delivered by TEG at the digital system voltage (either 3.3 or 5 V). Any power surplus not used in sensing and data transmission can be stored in long-life energy storage devices, such as batteries or super-capacitors. Sensors (temperature, pressure, etc.) will measure the intended parameters from different power plant components and provide an analog electrical signal to an industry-standard microcontroller, where it will be processed and converted into digital form. The processed data will be sent to plant staff via wireless data transmitters, also based on commercially mature products. It is important to protect the electronics package from harsh environmental conditions, such as water, fire, shock, and high doses of nuclear radiation (*alpha*, *beta*, *gamma,* and *neutron*). Industry-standard chips can typically endure temperatures as high as 125°C, but offer no measure of protection against water or nuclear radiation. For this reason, it is necessary is to develop a robust enclosure to protect the system from damage. Damage from the environment, if not mitigated, may result in errors in microcomputer control programs or signal voltages, as well as long-term degradation of both the electronic systems and the TEGs themselves [149]. Suitable protective materials, along with properly designed thickness and structure, are necessary for a working design.

7.3 Characterization of Commercial TEGs

The obvious requirement for a good TE material to be considered for integration into a power-generation device is to possess a high average ZT over the projected temperature range. Additional requirements are the working temperature range, performance, scalability, reliability, and cost-effectiveness. Bi_2Te_3 is by far the most common thermoelectric material in bulk form used for cooling and power generation applications near ambient temperature. Other common commercially available TE materials include PbTe and SiGe, which have higher operating temperatures. Materials such as *n*-BiSb and *p*-TAGS and $CoSb_3$ are also used but are rare due to their poor mechanical strength and absence of homologous *n*-type or *p*-type material. Table 7-2 shows the common thermoelectric materials that are commercially available with their temperature range and typical ZT values.

Table 7-2 Temperature ranges and different usable materials[150]

Temperature (°C)	Type	TEG material	ZT (maximum)
<150	*p*	Bi_2Te_3	0.8
	n	Bi_2Te_3	0.8
150–500	*p*	Zn_4Sb_3	-
	p,n	PbTe	0.7, 0.8
	p	TeAgGeSb (TAGS)	1.2
500–700	*p*	$CeFe_4Sb_{12}$	1.1
	n	$CoSb_3$	0.8
700–900	*p, n*	SiGe	0.6-1.0
	n	LaTe	1.4

Bi_2Te_3-based TEG modules have a specified operating temperature range of (300–520 K) [151], which is lower than typical industrial waste-heat source temperatures. For example, vehicle exhaust pipes and diesel generator exhaust pipes nominally experience hot-side temperatures of 770–870 K [121] and 750–780 K [152], respectively. The temperature requirements necessitate

proper system design to ensure the modules are working at the specified temperature range for maximum conversion efficiency.

7.3.1 TE Module Properties

TEG modules from Hi-Z Technology, Inc. (*San Diego, CA*), Marlow Industries, Inc. (*Dallas, TX*), Custom Thermoelectric (*Bishopville, MD*) and TECTEG MFR (*Ontario, Canada*) are compared in Table 7-3 based on power generation, efficiency, and cost. The modules were also characterized on a custom-built TEG test stand. The results from the characterization of the HZ-2 module are presented here. The HZ-2 module was characterized for use in waste heat recovery applications. The HZ-2 module consists of 97 thermocouples arranged electrically in series and thermally in parallel (Fig. 7-2). The module is provided with ceramic wafers for the cold and hot side to provide greater durability against the effects of thermal cycling.

Table 7-3 Comparison of Similar TEGs from different Manufacturers

Manufacturer	Hi-Z	Marlow	Custom TE	TECTEG
Model No.	HZ-2	TG12-6-01	1261G-7L31	1263-4.3
Material	Bi_2Te_3	Bi_2Te_3	Bi_2Te_3	Bi_2Te_3
Size [cm]	2.9×2.9×0.50	4.0×4.4×0.4	3.0×3.0×0.47	3.0×3.0×0.5
Cold Side Temp [°C]	30	50	30	30
Hot Side Temp [°C]	230	230	300	300
Open Circuit Voltage (V)	6.53	9.51	4.8	10.7
Matched Load Power [W]	2.5	6.16	4.2	5.2
Efficiency [%]	4.5	5.03	N/A	N/A
AC Resistance (Ohms)	4.0	4.56	3.5	~2.7-3.6
Price/module (USD)	30.00	39.25	27.50	34

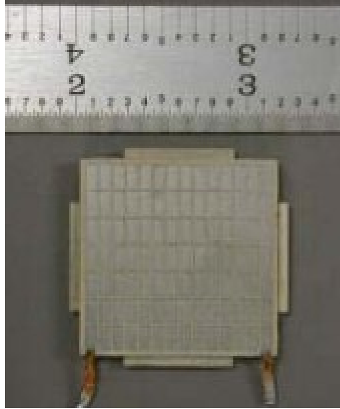

Fig. 7-2 Commercial HZ-2 Module

7.3.2 TEG Test Stand Design

The best method to characterize a TEG is to load it compressively between the heat source and a heat sink. A significant loss of efficiency in thermoelectric systems occurs due to thermal bypass, which is defined as thermal energy that passes from the hot side to the cold side without passing through the thermoelectric material. For the HZ-2, about 2% of the thermal energy passing through the module bypasses the thermoelectric material by passing through the module structure. A much larger portion of the thermal energy can bypass the module by passing through the metal support structure outside of the module and through the air gap between the hot and cold sides. Therefore, careful design is needed to ensure that heat will not pass from the heat source to the cold side through the mounting rods. These losses can be minimized by making the mounting rods as small as possible, choosing low thermal conductivity materials and by increasing the thermal path length.

A TEG test stand is designed to characterize the commercial TEGs for performance at different operating conditions. The test stand consists of a temperature-controlled heat source and heat sinks as shown in Fig. 7-3. The heater is fabricated from a block of copper (15.24 cm × 7.62 cm × 1.27 cm) with four 200 W cartridge heaters inserted into it. The heater is insulated on the bottom and the sides to minimize the heat loss and to provide 400 W of heat on the top surface.

The insulation is made from high-temperature insulation with an air gap to reduce conductive losses. The heating block is supported by ceramic rods to a base plate. Aluminum foil is placed between the heating block and insulating material that surrounds the heating block to reduce radiative losses. The temperature of the top surface and insulation performance were verified using a thermal imaging camera. The top surface was confirmed to be uniform with a maximum temperature difference along the surface of less than 2 °C. Also, there is minimal heat leakage through the insulator, with a temperature difference of 1.2 °C from the ambient.

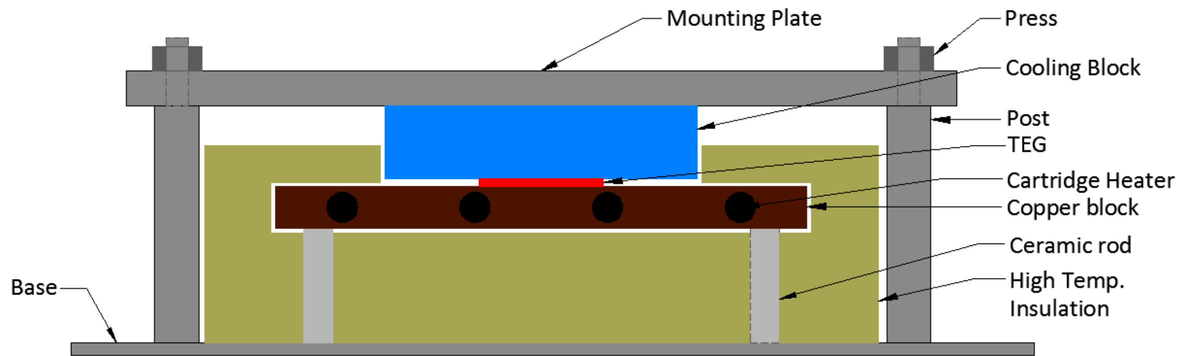

Fig. 7-3 TEG test stand configuration

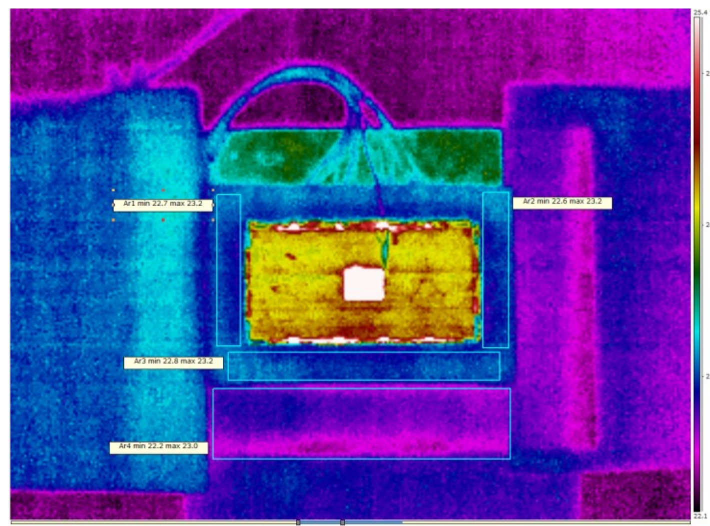

Fig. 7-4 Top copper surface thermal image

The heat sink consists of a water-cooled block with a thermal resistance of 0.011 °C/W mounted on top of the TEG. The water blocks are cooled with chilled water. The entire assembly is held together using screws and belleville washers. The TEGs are placed between the water block and heater with pressure applied to improve the thermal contact. The copper block and the water block are also polished to reduce surface roughness. Even when using advanced polishing methods, rugged areas remain on the surface of the TE modules and contact surfaces (Fig. 7-5). Thermal grease with a thermal conductivity of 2.8 W/m·K is used to increase the transfer of heat at the interface by replacing the air gaps, which have a thermal resistance of 0.0317 W/m-K.

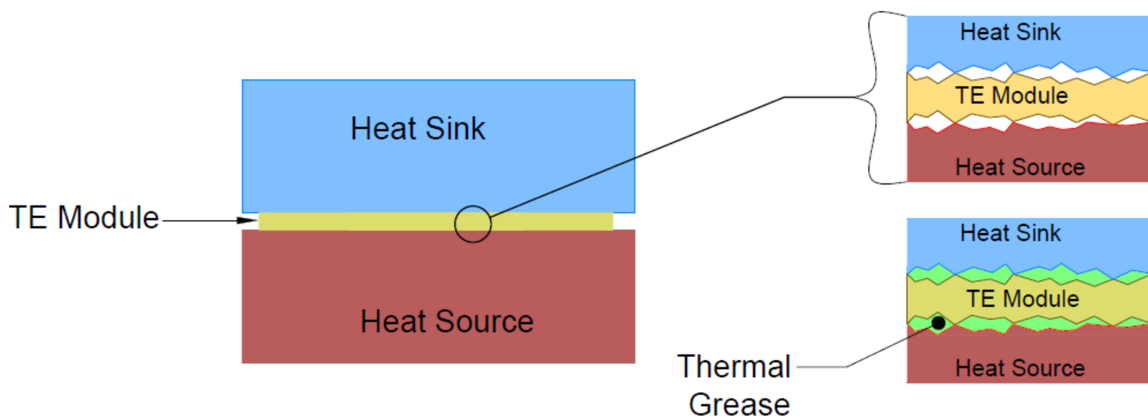

Fig. 7-5 Illustration of the effect of thermal flexible graphite sheet inserted at the boundary between the heat source and TE modules and heatsink.

7.3.3 Measurements

Measurements of the output voltage as a function of temperature difference were performed. The power output and efficiency at the matched load of the module were also measured at the maximum temperature difference attainable. Confirming this data allows the selection of an appropriate TEG module for the waste-heat recovery application. To determine these values, the temperature difference, the heat flux and the power generated by the TEG must be measured. The temperature

and heat flux are measured as shown in Fig. 7-6. A resistance temperature detectors (RTD) is used the measure the temperature difference between the water inlet and outlet.

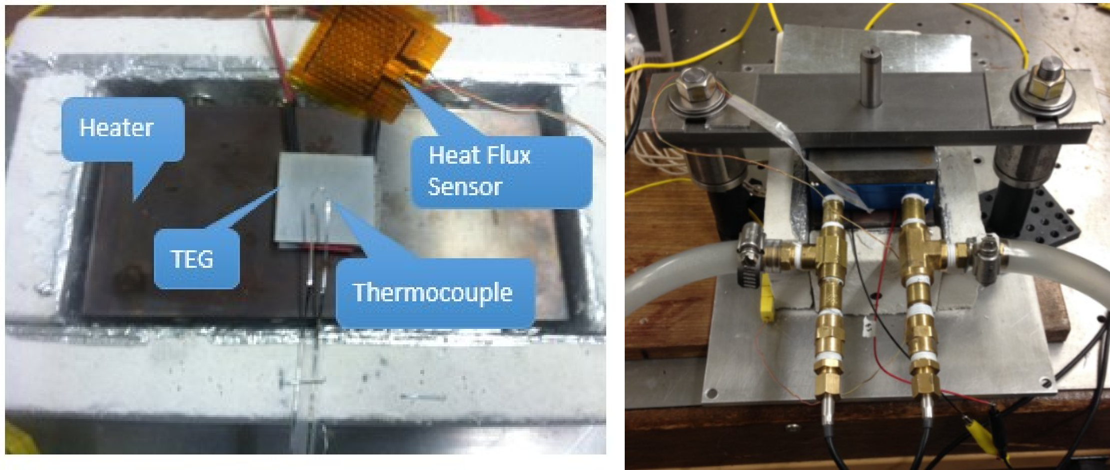

Fig. 7-6 Measurement setup of temperature and heat flux (left) and RTD probes for water inlet and outlets (right)

The data acquisition (DAQ) system is shown in Fig. 7-7. Thermal measurements from the test stand are made using a Keithley 2000 digital multi-meter (DMM) and the electrical output from the TEG is measured using an electronic load (*BK Precision* 8500). The data is collected automatically through the DAQ system and loaded into Microsoft Excel© directly for analysis.

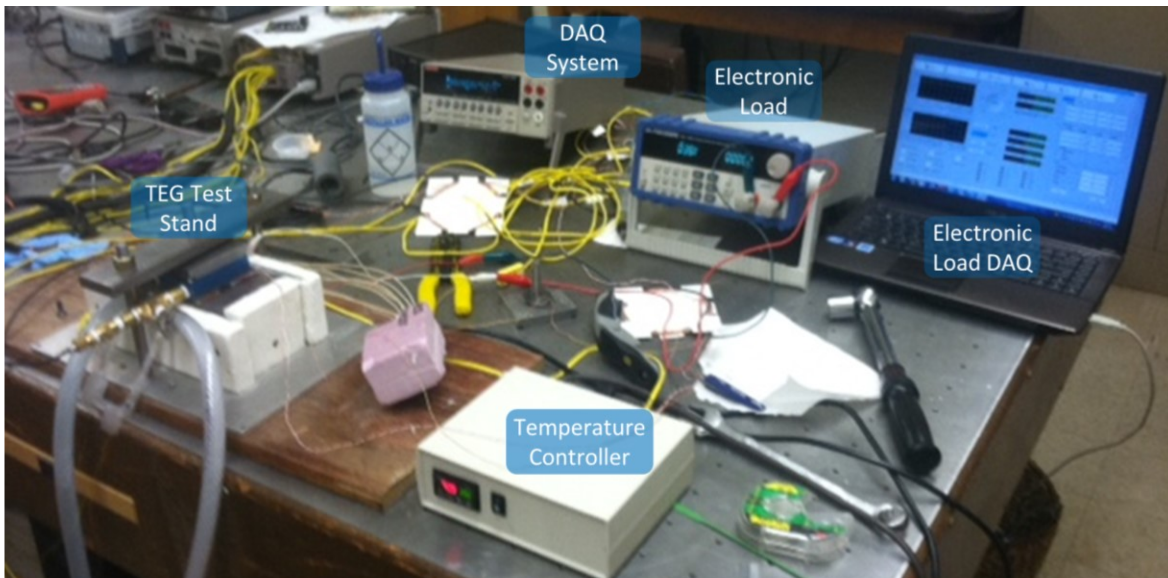

Fig. 7-7 DAQ system for TEG test stand

7.4 Design and Fabrication of TEG-based Sensor Prototype

To verify proof-of-concept of the system, a laboratory-scale prototype is developed for testing. Since testing at an actual nuclear facility is impractical, field tests are performed locally at Calpine's cogeneration facility located at Stony Brook University. A Schedule-40 vertical steam header pipe 0.324 m (12.75 in) diameter was chosen for prototype installation following a thorough survey of the cogeneration facility. The pipe has a wall temperature of ~350°C during normal operation and is insulated with 50.8 mm (2 in) fiberglass.

A schematic of the design and mounting configuration of the TEG system on the steam pipe is shown in Fig. 7-8. A commercial TEG module rated at 2.0 W (HZ-2, *Hi-Z Technology Inc.,* US) was selected. The pipe coupler is manufactured from Aluminum 6061 (19.1 m thick and an included angle of 70°). Heat is extracted from the pipe with the aid of a coupler plate matching the curvature of the pipe. There are different attachment options provided in the literature [153]. The assembly consists of three parts that are bolted to form the entire assembly. Thermal grease is used between each part to reduce thermal resistance at the interface between the mating surfaces. For this prototype design, heavy-duty stainless-steel strap clamps are used. Deformable graphite foil serves as a high-temperature thermal interface material between the coupler and the pipe to improve heat transfer. A heat conductor rod connects the coupler to a plate where the TEGs are mounted. The heat sink and the electronic package containing the wireless transceiver, data storage, and power management are located outside the pipe insulation.

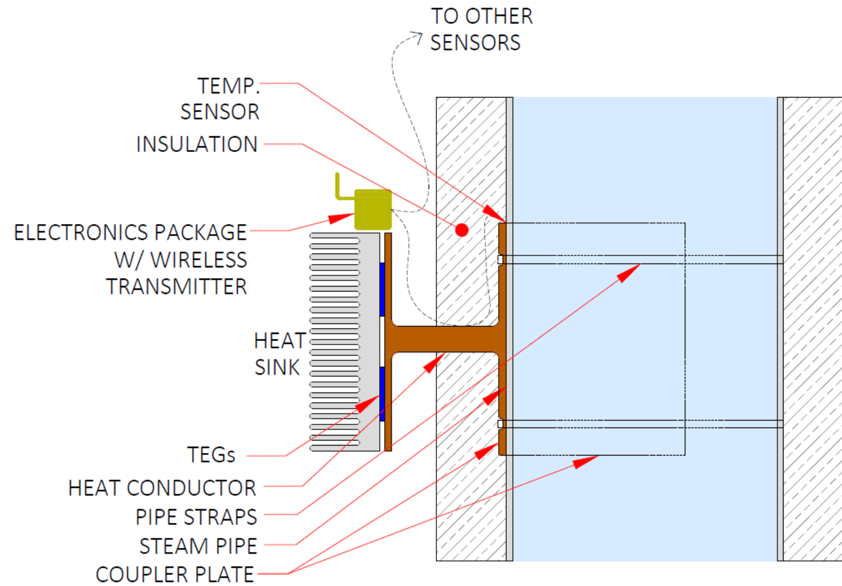

Fig. 7-8 A cross section of prototype of TEG-based sensor package attached to a hot pipe

Critical design parameters to be determined include the dimension and weight of the attachment and the size of the heatsink. Thermal analysis is performed to obtain the required design parameters such as the area of the coupling plate, the size of the conducting rod, the materials to be used, and the size of the heatsink. The assembly must be able to provide 200 °C required at the hot side of TEG and the ambient temperature inside the power plant is assumed to be 30 °C. Thermal analysis is performed in COMSOL Multiphysics® software.

Proper mounting of TEGs was very important in this experiment. Mounting without enough compression force reduces the power output. Excessive or unequal compression force can damage TEGs. The TEG mounting method was based on the installation guide from Custom Thermoelectric [35]. The screws are equipped with belleville washers and positioned 12.7 mm from the side of the TEGs.

7.5 Results and Discussion

7.5.1 Results for HZ2 Module

The first measurement that was performed was the open circuit voltage as a function of the temperature difference. This data is used to confirm that the experimental conditions are close to the ideal case. The data also helps in determining the appropriate amount of compressive load needed and temperature stability of the TEG. The results for the HZ-2 module and are given in Fig. 7-9. The data points represent the measured data while the lines show the manufacturer data supplied from HZ-2 for comparison. The results show that the device is operating as expected. The difference from the curve at a higher temperature difference is due to the change in the Seebeck coefficient at higher temperatures. The maximum hot side temperature and cold side temperature for the module were 232°C and 76°C, respectively.

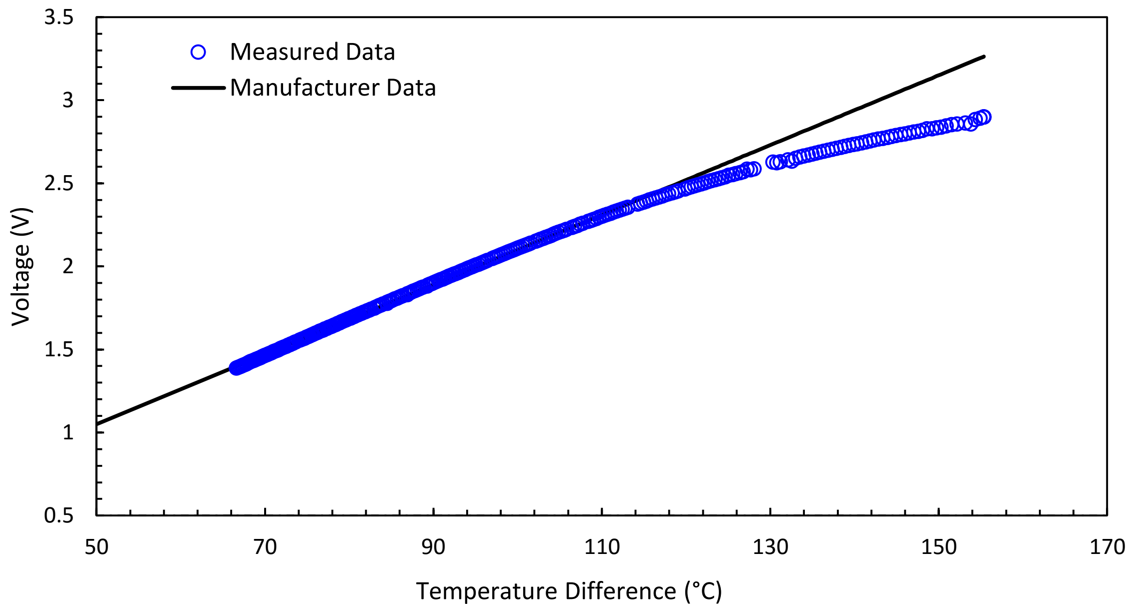

Fig. 7-9 Open Circuit Voltage vs. temperature difference for HZ-2 module

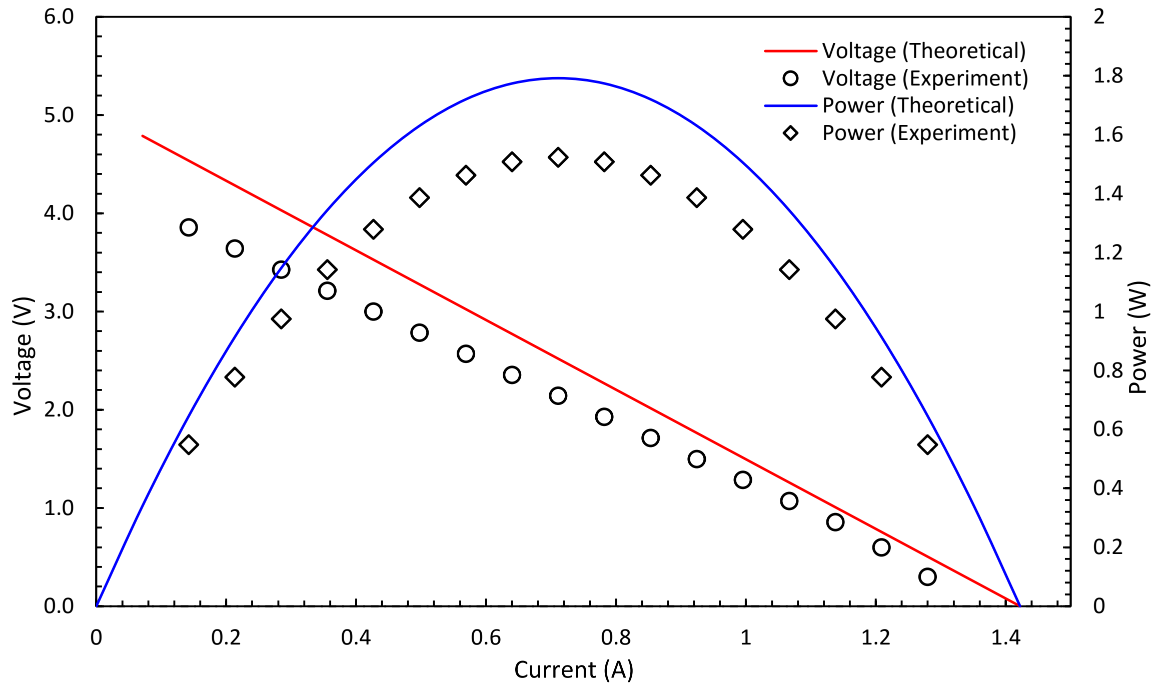

Fig. 7-10 HZ-2 Characteristic Curve

The power output from the TEG as a function of load resistance and the efficiency were also measured. The results are compared with the data sheet shown in Fig. 7-10. The measured data falls within 80% of HZ-2 performance listed in the technical data sheet. Errors in the data are most likely due to thermal losses, unstable temperature differentials, or internal resistances in the test set up. As mentioned earlier, the interface between the module and the heat sink are very critical to the performance of a thermoelectric system. The module needs to be compressively loaded between the heat source and the heatsink, even with the application thermal grease. The compressive load must be uniform across the TEG for optimum power performance. Insufficient compression leads to poor thermal contact and reduced performance.

The heat flow through the TEG was also collected and used to determine the efficiency of the TEG. One reason it is not possible to obtain the rated power from the module is that it is not operating at the temperatures that were measured. When measuring the temperatures of the hot

and cold sides, it is important to position the thermocouples as close to the module as possible. It is ideal to drill a thermocouple well into the thermal spreader plate and the cold side heat sink and position the thermocouple in the thermocouple well.

7.5.2 Final prototype design

Once a single TEG is characterized, the next step was to select an appropriate number of TEGs to be used in the prototype. This was selected based on the power output expected. The selection is based on the temperatures on the pipe determined from simulation results. It was found that four HZ-2 modules connected in series can provide the required power. The results from the thermal analysis of the TEG assembly is shown in Fig. 7-11. The size of the heat sink is determined based on a thermal resistance of 0.25 K/W, which results in a temperature difference of 100°C when dissipating ~250W to the ambient. A commercial heat sink from HS Marston (96CN-03000-A-200) is used. A temperature of 54°C is obtained on the surface of the heat sink using natural convection to the ambient.

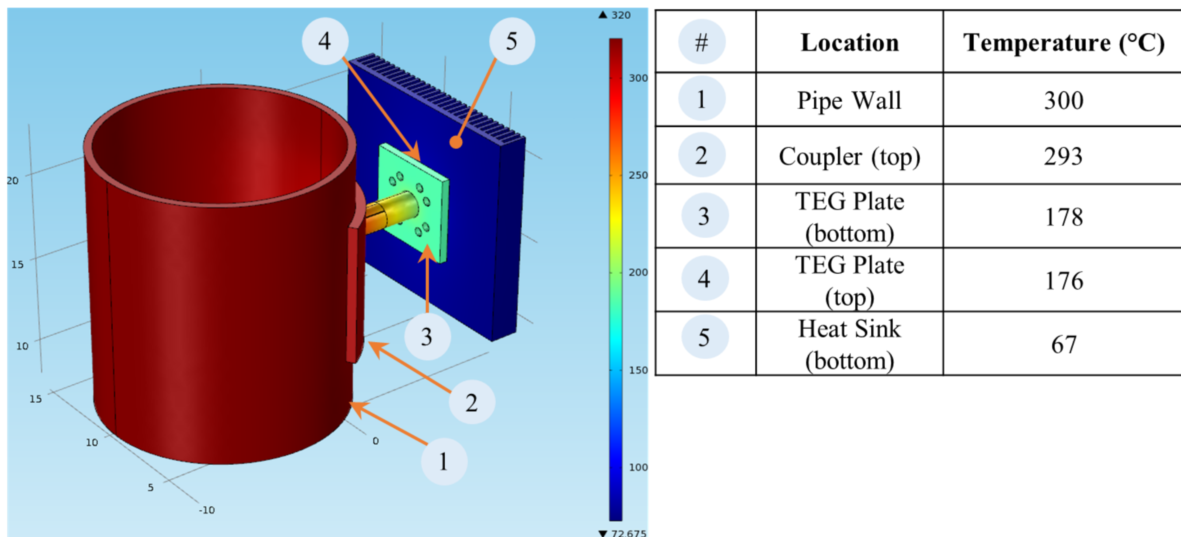

#	Location	Temperature (°C)
1	Pipe Wall	300
2	Coupler (top)	293
3	TEG Plate (bottom)	178
4	TEG Plate (top)	176
5	Heat Sink (bottom)	67

Fig. 7-11 Thermal analysis of designed prototype and temperatures at key locations

The prototype was verified in the laboratory using two 700 W infrared heaters as the heat source. The temperature of the pipe wall was set at 280 °C with the radiant ceramic heaters set at 492 °C. The heaters were placed in a section of a schedule-40 pipe, and the adapter was placed on the outside. A construction of a prototype unit derived from the analysis is shown in Fig 7-12. During the lab tests, the pipe temperature reached 280°C and the temperature at the heatsink was 48°C. The open circuit voltage through the four HZ-2 thermoelectric modules was around 5.0V and the total power produced was 1.0 W. Four HZ-2 modules were mounted on the TEG plate as shown in Fig 7-12c. The temperature at the pipe wall was fixed by the temperature controller at 280°C. The open circuit voltage under the actual conditions is around 90% of the rated performance of the HZ-2 module.

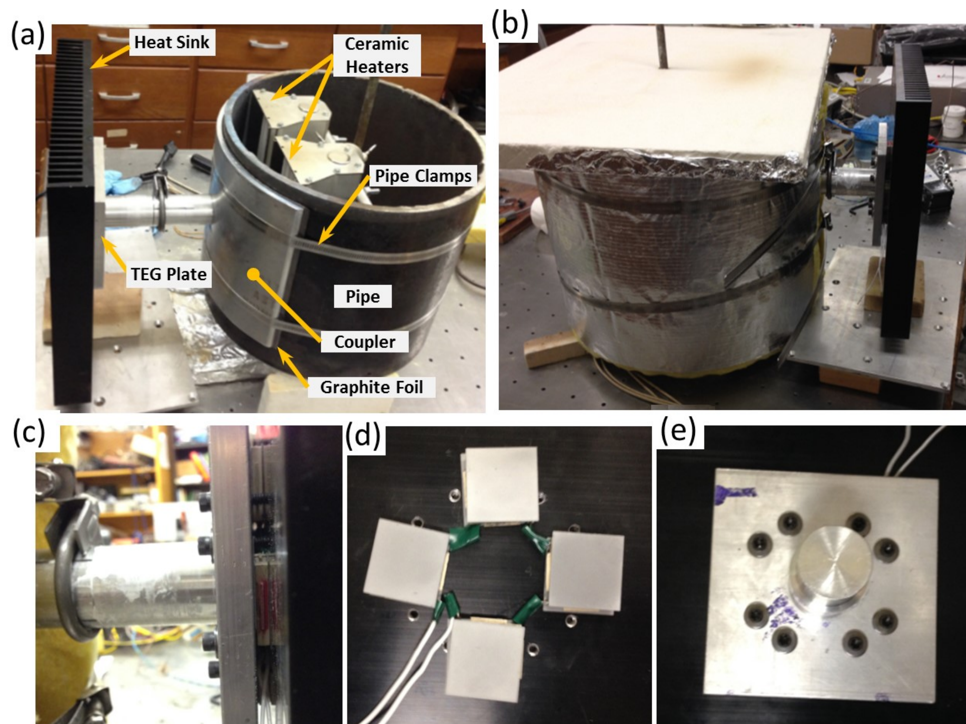

Fig. 7-12 (a) Lab test setup without insulation layer (b) and insulation layer (c) mounted TEGs (d) TEG mounting arrangement (e) mounting

The installed prototype is shown in Fig 7-13. The prototype was installed in a section of vertical steam header pipe at Stony Brook University's power facility. The data that was measured included the temperature of the pipe and the ambient temperature. This is shown in Fig 7-14.

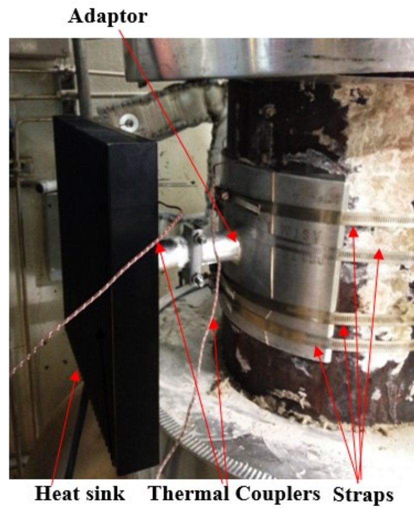

Fig. 7-13 Entire design installed on the steam pipe

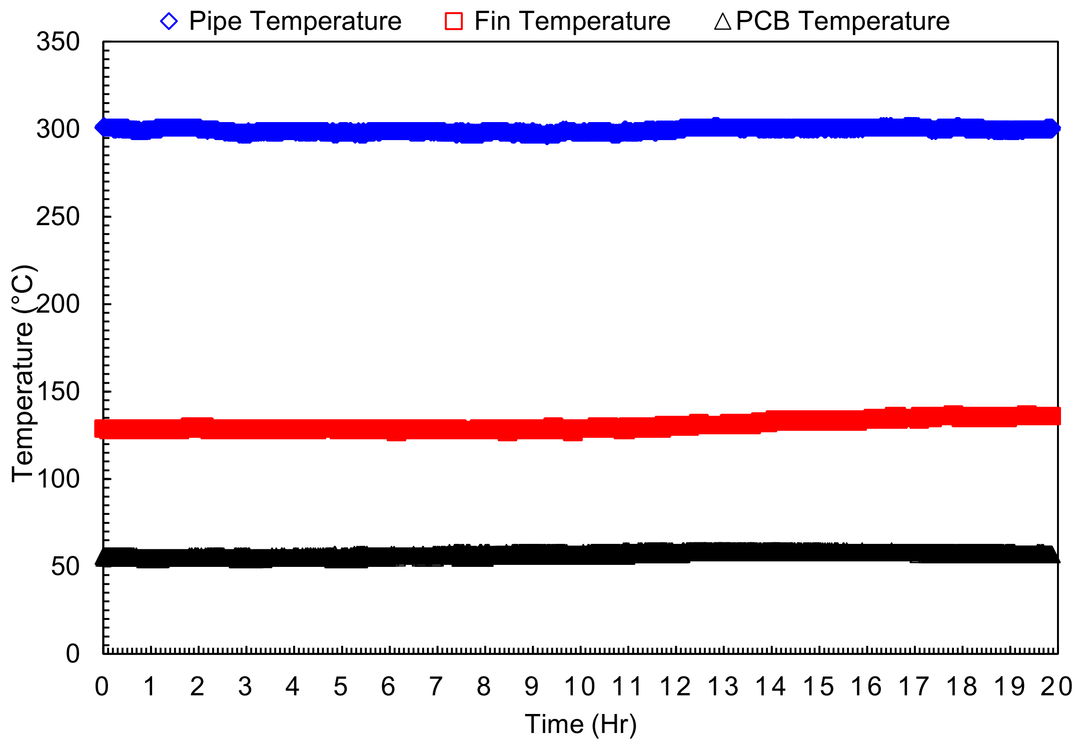

Fig. 7-14 Temperature data collected from TEG sensor for a 20-hour period

7.6 Summary

In this chapter, the application of thermoelectric generators in waste-heat energy harvesting are explored. A prototype assembly of a sensor package has been designed for use in a local power plant to simulate operation in a nuclear power plant. All design aspects and issues have been investigated utilizing a commercial TEG and a custom designed connection assembly using a commercial heat sink. The TEGs are well suited to the harsh conditions of a nuclear plant and can provide electricity for sensing and even actuation. The temperatures at target locations are around 300 °C, which is higher than commercial TEGs maximum temperature tolerance.

Chapter 8

Conclusions, Enabled Research Topics, and Future Directions

The fabrication of thermoelectric devices using additive and subtractive manufacturing techniques are investigated in this dissertation. Manufacturing methods for TEGs are a severe bottleneck for their widespread use in waste heat harvesting applications. Novel routes of additive and subtractive manufacturing technologies are well suited to overcome these bottlenecks by eliminating the need for subassembly requirements and allowing for an integrated fabrication process. As a result, these manufacturing techniques are evaluated as new and integrated manufacturing routes for thermoelectric devices. The feasibility of thermal spray, ink-dispenser printing, and laser micromachining are investigated and used to fabricate a thermoelectric generator directly onto exhaust heat sources.

In Chapter 2, thermoelectric operating theory, materials, and devices are introduced. Thermoelectricity is an important field for the development of environmentally friendly thermal systems and research into novel thermoelectric materials with high ZT, and appropriate manufacturing technology could result in a breakthrough in the wide scale application of TEGs.

In Chapter 3, the feasibility of thermal spray as a means of fabrication for TE materials and devices has been investigated. Thermally sprayed materials are well suited for fabricating the insulating and conducting layers of a TEG, but have poor thermoelectric performance. In this work,

progress towards developing an integrated, one-step process to fabricate thermoelectric materials, bonding materials, and electrical contacts using ink-dispenser printing and laser sintering is presented. It is anticipated that this approach will largely resolve the interface, durability, and heat transfer issues prevalent with the conventional approach of integrating pre-fabricated TE modules onto exhaust components. This fabrication method eliminates the need for soldering, gluing/epoxying, and mechanical pressure joining which significantly simplifies the device fabrication process while reducing cost and improving reliability. Further work is required to optimize the process, explore additional potential filling materials, and obtain high-quality coatings. Thermally sprayed materials are well suited for fabricating the insulating and conducting layers of a TEG, but have poor thermoelectric performance.

The thermal spray process presents a challenging material science problem. It was very difficult to find high-quality powders with the proper spray characteristics, and the thermal spray process itself can significantly alter the delicate stoichiometry required to provide usable thermoelectric properties. While providing high-throughput and high-quality mechanical properties, the electrical properties of the thermal sprayed thermoelectric materials are poor at this time. Possible materials that could be explored in the future for spraying include oxide materials such as zinc oxide (ZnO) and titanium oxide (TiO_2). Finally, the powder-to-device transfer efficiency is low. For high-cost powders, this represents a significant loss, or at least requires complicated and expensive powder recycling technology. The conclusion is that thermal spray is unfeasible for producing reliable, high-quality thermoelectric materials. However, the feasibility of using the thermal spray as a manufacturing technique has been demonstrated.

In Chapter 4, SM methods for thermoelectric device fabrication were evaluated. Based on this evaluation, laser micromachining has been determined to be the best procedure for TE applications. The experimental results from laser patterning of thermal spray samples of different materials and thickness have been presented. The optimization of laser parameters is important for successful electrical isolation needed in thermal spray device manufacturing and machining high-quality features is discussed. In this study, results are presented for several short-pulse lasers (nanosecond) in which laser power, laser wavelength, focusing lens, processing speed, repetition rate, and pressure and flow of purge gas were varied. The optimum laser parameters were those that minimize the heat-affected zone and resulted in the fastest processing times. The resulting laser patterns were characterized using both optical and scanning electron (SEM) microscopy, and by verifying electrical isolation between patterned regions using contact resistance measurements. It was found that faster processing speeds at higher power could result in improved cut qualities. Future work will include further optimizing the laser parameters and explore other laser systems as they become available.

In Chapter 5, the use of additive-subtractive manufacturing techniques for the fabrication of a working TEG is presented. The feasibility of using thermal spray and laser micromachining to fabricate thermoelectric generators directly onto engineering components was explored. The target applications include automotive exhaust systems and high-volume waste heat sources. The steps required to fabricate a thermoelectric device are presented, including the formation of the bottom and top metallic layers and the thermoelectric elements. Technique for bridging the air gap between adjacent thermoelectric elements for the top layer based on a sacrificial filler material was also demonstrated. The results from the characterization of a flat (50.8 × 50.8 mm) TEG module

fabricated with this method are presented. The performance was found to be comparable to the expected values based on material properties. The process developed is summarized in Fig. 8-1.

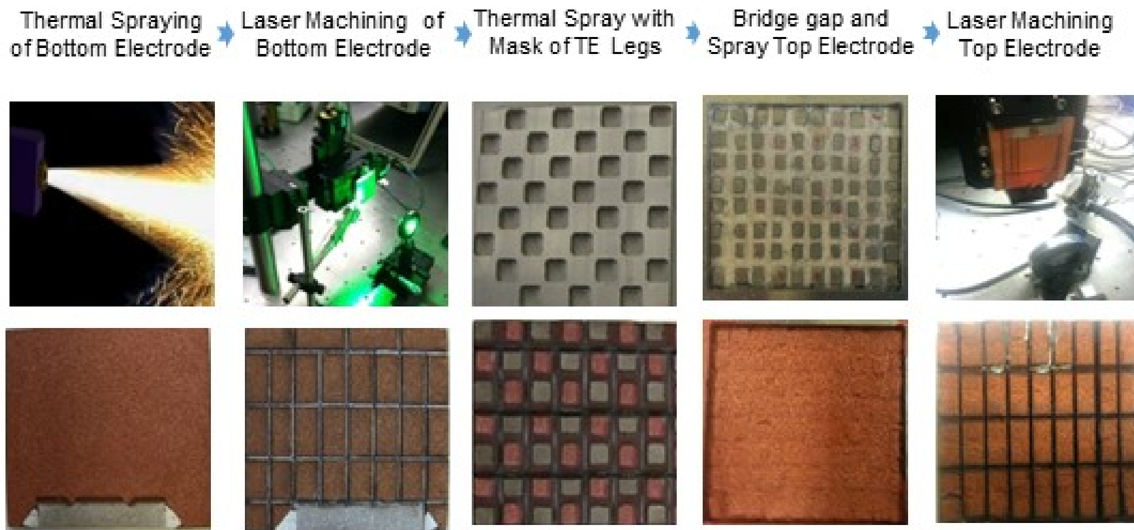

Fig. 8-1 Additive & Subtractive TEG Manufacturing using Thermal Spray (Additive) and Laser Machining (Subtractive)

In Chapter 6, the feasibility off dispenser printing as a technique for the fabrication of TE materials and devices was investigated. Printable thermoelectric materials were first synthesized in the form of inks, which consist of active materials dispersed in a polymer binder. A suitable epoxy resin was chosen and formulated. Thermophysical properties of the printed materials were measured as a function of curing temperature and were demonstrated to have high thermoelectric performance. The thermal conductivity of the printed materials was low due to their composite nature. The Seebeck coefficients of the printed materials were found to be similar to that of bulk materials while the electrical conductivity was low. The addition of silver nanoparticles increased the electrical conductivities but reduced the Seebeck coefficients, canceling out the overall improvement in ZT. Hall-effect measurements are needed to explain these results fully, but it can be inferred that the primary reason is increased carrier concentration due to the addition of metal

nanoparticles. The maximum *ZT* values for the n-type and p-type material are 0.3 and 0.11, respectively. Dispenser printing strategies were also developed. The printed feature sizes depend on the needle size. The optimum printing variables such as ink, viscosity, pressure, shot height and shot spacing on feature sizes were determined.

In Chapter 7, the application of thermoelectric generators in waste-heat energy harvesting is explored. These include vehicle waste heat, sensors for harsh environments and engineering components with complex shapes and devices. The design and fabrication of a TEG-based sensor for nuclear power plants are presented. The TEGs are well suited to the harsh conditions of a nuclear plant and can provide electricity for sensing and even actuation. The temperatures at target locations are around 300 °C, which is generally higher than commercial TEGs maximum temperature tolerance. A prototype assembly of a sensor package is designed for a conventional power plant to simulate operation in a nuclear power plant. The design aspects and issues have been investigated that utilize a commercial TEG and a custom designed connection assembly using a commercial heat sink.

Directions for future research will include investigation of novel AM techniques to allow for high-quality TE materials to improve the performance of the fabricated TEGs.

Bibliography

1. T.M. Tritt, and M.A. Subramanian, Thermoelectric Materials, Phenomena, and Applications: A Bird's Eye View, *MRS Bulletin*, 2006, **31**(p. pp 188-198

2. N/A, Thermoelectric Generators Market by End User, Market and Markets, 2015.

3. EIA, International Energy Outlook 2014, J. Conti Ed., U.S. Energy Information Administration, 2014.

4. D.M. Rowe, Thermoelectrics Handbook: Macro to Nano, CRC Press, 2005.

5. LLNL, Estimated Energy Use in 2013, Lawrence Livermore National Laboratory 2013.

6. S. LeBlanc, Thermoelectric generators: Linking material properties and systems engineering for waste heat recovery applications, *Sustainable Materials and Technologies*, 2014, **1–2**(0), p. 26-35

7. M. Yahatz, and J. Harper, Fabrication of thermoelectric modules and solder for such fabrication, Google Patents, 1998.

8. R. Joachim, and W. Heinz, Thermoelectric couple with soft solder electrically connecting semi-conductors and method of making same, Google Patents, 1969.

9. Ian Gibson, D.W. Rosen, and B. Stucker, Additive Manufacturing Technologies, Springer US, 2010.

10. L. Mortara, J. Hughes, P.S. Ramsundar, F. Livesey, and D.R. Probert, Proposed classification scheme for direct writing technologies, *Rapid Prototyping Journal*, 2009, **15**(4), p. 299-309

11. H. Zou, D.M. Rowe, and G. Min, Growth of p- and n-type bismuth telluride thin films by co-evaporation, *Journal of Crystal Growth*, 2001, **222**(1–2), p. 82-87

12. M. Takashiri, T. Shirakawa, K. Miyazaki, and H. Tsukamoto, Fabrication and characterization of Bi0.4Te3.0Sb1.6 thin films by flash evaporation method, *Journal of Alloys and Compounds*, 2007, **441**(1–2), p. 246-250

13. M. Takashiri, T. Shirakawa, K. Miyazaki, and H. Tsukamoto, Fabrication and characterization of bismuth–telluride-based alloy thin film thermoelectric generators by flash evaporation method, *Sensors and Actuators A: Physical*, 2007, **138**(2), p. 329-334

14. A. Yamamoto, H. Hagino, Y. Hashimoto, and K. Miyazaki, The Effects of Thermoelectric Film Thickness on Performance of In-Plane Thermoelectric Modules, *Journal of Electronic Materials*, 2012, **41**(6), p. 1799-1804, in English

15. P.H. Le, C.N. Liao, C.W. Luo, and J. Leu, Thermoelectric properties of nanostructured bismuth-telluride thin films grown using pulsed laser deposition, *Journal of Alloys and Compounds*, 2014, **615**(p. 546-552, in English

16. A. Bailini, F. Donati, M. Zamboni, V. Russo, M. Passoni, C.S. Casari, A.L. Bassi, and C.E. Bottani, Pulsed laser deposition of Bi2Te3 thermoelectric films, *Applied Surface Science*, 2007, **254**(4), p. 1249-1254, in English

17. H. Bottner, J. Nurnus, A. Gavrikov, G. Kuhner, M. Jagle, C. Kunzel, D. Eberhard, G. Plescher, A. Schubert, and K.H. Schlereth, New thermoelectric components using microsystem technologies, *Microelectromechanical Systems, Journal of*, 2004, **13**(3), p. 414-420

18. R. Shea, A. Gawarikar, and J. Talghader, Process Integration of Co-Sputtered Bismuth Telluride/Antimony Telluride Thermoelectric Junctions, *Journal of Microelectromechanical Systems*, 2014, **23**(3), p. 681-688, in English

19. H.O. Pierson, Handbook of Chemical Vapor Deposition, 2nd ed., Noyes Publications, 1999.

20. C.F. Powell, J.H. Oxley, and J. John M. Blocher, Vapor deposition, John Wiley & Sons, 1966.

21. M.L. Hitchman, and K.F. Jensen, Chemical vapor deposition: Principles and applications, Academic Press, 1993.

22. J. Kim, Y. Choi, D. Choi, and S. Choi, Study on the Thermoelectric Properties of CVD SiC Deposited with Inert Gases, *Journal of Electronic Materials*, 2011, **40**(5), p. 840-844, in English

23. J. Tsukamoto, A. Takahashi, T. Tani, and T. Ishiguro, Thermoelectric power of heat-treated CVD carbon fibers, *Carbon*, 1989, **27**(6), p. 919-923

24. Y. Kumashiro, T. Enomoto, K. Sato, Y. Abe, K. Hirata, and T. Yokoyama, Thermoelectric properties of photo- and thermal CVD boron and boron phosphide films, *Journal of Solid State Chemistry*, 2004, **177**(2), p. 529-532

25. G. Bendt, S. Schulz, S. Zastrow, and K. Nielsch, Single-Source Precursor-Based Deposition of Sb2Te3 Films by MOCVD, *Chem. Vapor Depos.*, 2013, **19**(7-9), p. 235-241, in English

26. S.W. Kang, K.M. Jeon, J.S. Shin, J.R. Chun, Y.H. Kim, S.J. Lee, and J.Y. Yun, MOCVD of C-oriented Bi2Te3 Films on SiO2 Substrates using Triethyl Bismuth and Di-tertiarybutyl Tellurium, *Chem. Vapor Depos.*, 2013, **19**(1-3), p. 61-67, in English

27. J.P. Fleurial, G.N. Snyder, J.A. Herman, P.H. Giauque, W.M. Phillips, M.A. Ryan, P. Shakkottai, E.A. Kolawa, and M.A. Nicolet, Thick-film thermoelectric microdevices, *Thermoelectrics, 1999. Eighteenth International Conference on*, 1999, p. 294-300.

28. F. Xiao, C. Hangarter, B. Yoo, Y. Rheem, K.-H. Lee, and N.V. Myung, Recent progress in electrodeposition of thermoelectric thin films and nanostructures, *Electrochimica Acta*, 2008, **53**(28), p. 8103-8117

29. B.Y. Yoo, C.K. Huang, J.R. Lim, J. Herman, M.A. Ryan, J.P. Fleurial, and N.V. Myung, Electrochemically deposited thermoelectric n-type Bi2Te3 thin films, *Electrochimica Acta*, 2005, **50**(22), p. 4371-4377

30. F. Li, and W. Wang, Electrodeposition of BixSb2−xTey thermoelectric thin films from nitric acid and hydrochloric acid systems, *Applied Surface Science*, 2009, **255**(7), p. 4225-4231

31. S.-K. Lim, M.-Y. Kim, and T.-S. Oh, Thermoelectric properties of the bismuth–antimony–telluride and the antimony–telluride films processed by electrodeposition for micro-device applications, *Thin Solid Films*, 2009, **517**(14), p. 4199-4203

32. Y. Miyazaki, and T. Kajitani, Preparation of Bi2Te3 films by electrodeposition, *Journal of Crystal Growth*, 2001, **229**(1–4), p. 542-546

33. S. Golia, M. Arora, R.K. Sharma, and A.C. Rastogi, Electrochemically deposited bismuth telluride thin films, *Current Applied Physics*, 2003, **3**(2–3), p. 195-197

34. J.R. Davis, Handbook of Thermal Spray Technology, ASM International, 2004.

35. H. Herman, S. Sampath, and R. McCune, Thermal Spray: Current Status and Future Trends, *MRS Bulletin*, 2000, **25**(07), p. 17-25, in English

36. G. Fu, L. Zuo, J. Longtin, C. Nie, and R. Gambino, Thermoelectric properties of magnesium silicide fabricated using vacuum plasma thermal spray, *Journal of Applied Physics*, 2013, **114**(14), p. 6

37. G. Fu, L. Zuo, J. Longtin, C. Nie, Y. Chen, M. Tewolde, and S. Sampath, Thermoelectric Properties of Magnesium Silicide Deposited by Use of an Atmospheric Plasma Thermal Spray, *Journal of Electronic Materials*, 2014, **43**(7), p. 2723-2730

38. M. Fukumoto, M. Itoh, Y. Tanaka, H. Yakabe, and K. Kikuchi, Preparation of Beta-Fesi2 Thermoelectric Coatings by Plasma Spraying of Mechanically-Alloyed Powders *J. Jpn. Inst. Metals*, 1998, **62**(5), p. p 449-456 (in Japanese)

39. Y. Tanaka, Y. Tokimoto, and M. Fukumoto, Fabrication and Improvement of Plasma Sprayed Si-Ge Thermoelectric Coating, *J. Jpn. Inst. Metals*, 1999, **63**(8), p. p 1029-1035 (in Japanese)

40. J. Majumdar, Thermal and Cold Spraying Technology in Manufacturing, *Handbook of Manufacturing Engineering and Technology*, A. Nee Ed., Springer London, 2014, p. 1-37.

41. S.J. Kim, J.H. We, J.S. Kim, G.S. Kim, and B.J. Cho, Thermoelectric properties of P-type Sb2Te3 thick film processed by a screen-printing technique and a subsequent annealing process, *Journal of Alloys and Compounds*, 2014, **582**(0), p. 177-180

42. H.B. Lee, J.H. We, H.J. Yang, K. Kim, K.C. Choi, and B.J. Cho, Thermoelectric properties of screen-printed ZnSb film, *Thin Solid Films*, 2011, **519**(16), p. 5441-5443

43. H.-B. Lee, H. Yang, J. We, K. Kim, K. Choi, and B. Cho, Thin-Film Thermoelectric Module for Power Generator Applications Using a Screen-Printing Method, *Journal of Electronic Materials*, 2011, **40**(5), p. 615-619, in English

44. C. Zhuo, E. Koukharenko, M.J. Tudor, R.N. Torah, and S.P. Beeby, Screen printed flexible Bi 2 Te 3 -Sb 2 Te 3 based thermoelectric generator, *Journal of Physics: Conference Series*, 2013, **476**(1), p. 012031

45. J.H. We, S.J. Kim, G.S. Kim, and B.J. Cho, Improvement of thermoelectric properties of screen-printed Bi2Te3 thick film by optimization of the annealing process, *Journal of Alloys and Compounds*, 2013, **552**(0), p. 107-110

46. C. Navone, M. Soulier, M. Plissonnier, and A.L. Seiler, Development of (Bi,Sb)2(Te,Se)3-Based Thermoelectric Modules by a Screen-Printing Process, *Journal of Electronic Materials*, 2010, **39**(9), p. 1755-1759, in English

47. C. Navone, M. Soulier, J. Testard, J. Simon, and T. Caroff, Optimization and Fabrication of a Thick Printed Thermoelectric Device, *Journal of Electronic Materials*, 2011, **40**(5), p. 789-793, in English

48. Z. Cao, E. Koukharenko, R.N. Torah, and S.P. Beeby, Exploring screen printing technology on thermoelectric energy harvesting with printing copper-nickel and bismuth-antimony thermocouples, *Solid-State Sensors, Actuators and Microsystems (TRANSDUCERS & EUROSENSORS XXVII), 2013 Transducers & Eurosensors XXVII: The 17th International Conference on*, 2013, p. 478-481.

49. A. Chen, D. Madan, P.K. Wright, and J.W. Evans, Dispenser-printed planar thick-film thermoelectric energy generators, *Journal of Micromechanics and Microengineering*, 2011, **21**(10), p. 104006

50. D. Madan, A. Chen, P.K. Wright, and J.W. Evans, Dispenser printed composite thermoelectric thick films for thermoelectric generator applications, *Journal of Applied Physics*, 2011, **109**(3), p. -

51. P. Calvert, Inkjet Printing for Materials and Devices, *Chemistry of Materials*, 2001, **13**(10), p. 3299-3305

52. A. Besganz, V. Zöllmer, R. Kun, E. Pál, L. Walder, and M. Busse, Inkjet Printing as a Flexible Technology for the Deposition of Thermoelectric Composite Structures, *Procedia Technology*, 2014, **15**(0), p. 99-106

53. H.S. Kim, J.S. Kang, J.S. Park, H.T. Hahn, H.C. Jung, and J.W. Joung, Inkjet printed electronics for multifunctional composite structure, *Composites Science and Technology*, 2009, **69**(7–8), p. 1256-1264

54. M. Zebarjadi, K. Esfarjani, M.S. Dresselhaus, Z.F. Ren, and G. Chen, Perspectives on thermoelectrics: from fundamentals to device applications, *Energy & Environmental Science*, 2012, **5**(1), p. 5147-5162

55. Y.C. Lan, D.Z. Wang, G. Chen, and Z.F. Ren, Diffusion of nickel and tin in p-type (Bi,Sb)2Te3 and n-type Bi2(Te,Se)3 thermoelectric materials, *Applied Physics Letters*, 2008, **92**(10), p. 101910

56. J. Weber, K. Potje-Kamloth, F. Haase, P. Detemple, F. Völklein, and T. Doll, Coin-size coiled-up polymer foil thermoelectric power generator for wearable electronics, *Sensors and Actuators A: Physical*, 2006, **132**(1), p. 325-330

57. Q. Zhang, Y. Sun, W. Xu, and D. Zhu, Organic Thermoelectric Materials: Emerging Green Energy Materials Converting Heat to Electricity Directly and Efficiently, *Advanced Materials*, 2014, **26**(40), p. 6829-6851

58. D.K.C. McDonald;, Thermoelectricity: An Introduction to the Principles, Wiley, 1962.

59. R.T. Delves, Thermomagnetic effects in semiconductors and semimetals, *Reports on Progress in Physics*, 1965, **28**(1), p. 249

60. D.P. Daniel, Thermoelectric Phenomena, *CRC Handbook of Thermoelectrics*, D.M. Rowe Ed., CRC Press, 1995.

61. H.B. Callen, Thermodynamics and an Introduction to Thermostatistics 2nd Ed. ed., John Wiley & Sons, 1985.

62. D.K. Kondepudi, and I. Prigogine, Modern Thermodynamics: From Heat Engines to Dissipative Structures, John Wiley & Sons, 1999.

63. L. Onsager, Reciprocal Relations in Irreversible Processes. I, *Physical Review*, 1931, **37**(4), p. 405-426

64. N.W.A.a.N.D. Mermin, Solid State Physics, Saunders College, 1976.

65. A. Shakouri, Recent Developments in Semiconductor Thermoelectric Physics and Materials, *Annual Review of Materials Research*, 2011, **41**(1), p. 399-431

66. E.S.T. G. J. Snyder, Complex thermoelectric materials, *Nature Publishing Group*, 2008,

67. C. Wood, Materials for thermoelectric energy conversion, *Reports on Progress in Physics*, 1988, **51**(4), p. 459

68. E. Altenkirch, Elektrothermische Kälteerzeugung und reversible elektrische Heizung, *Phys. Zeits*, 1911, **12**(p. 920-924

69. A.F. Ioffe, Semiconductor Thermoelements and Thermoelectric cooling, Infosearch, 1957.

70. A.F. Ioffe, The Revival of Thermoelectricity, *Scientific American*, 1958, **199**(p. 31-37

71. M.S. Dresselhaus, G. Chen, M.Y. Tang, R.G. Yang, H. Lee, D.Z. Wang, Z.F. Ren, J.P. Fleurial, and P. Gogna, New Directions for Low-Dimensional Thermoelectric Materials, *Advanced Materials*, 2007, **19**(8), p. 1043-1053

72. R. Venkatasubramanian, E. Siivola, T. Colpitts, and B. O'Quinn, Thin-film thermoelectric devices with high room-temperature figures of merit, *Nature*, 2001, **413**(6856), p. 597-602

73. J.W. Fergus, Oxide materials for high temperature thermoelectric energy conversion, *Journal of the European Ceramic Society*, 2012, **32**(3), p. 525-540

74. X.F. Zheng, C.X. Liu, Y.Y. Yan, and Q. Wang, A review of thermoelectrics research – Recent developments and potentials for sustainable and renewable energy applications, *Renewable and Sustainable Energy Reviews*, 2014, **32**(p. 486-503

75. G.S. Nolas, J. Sharp, and H.J. Goldsmid, Thermoelectrics: Basic Principles and New Materials Developments, Springer, 2001.

76. D.M. Rowe, and G. Min, Design theory of thermoelectric modules for electrical power generation, *IEE Proceedings - Science, Measurement and Technology*, 1996, p. 351-356.

77. H.J. Goldsmid, Conversion Efficiency and Figure-of-Merit, *CRC Handbook of Thermoelectrics*, D.M. Rowe Ed., CRC Press, 1995.

78. B. Sherman, R.R. Heikes, and J.R.W. Ure, Calculation of Efficiency of Thermoelectric Devices, *Journal of Applied Physics*, 1960, **31**(1), p. 1-16

79. R.E. Bentley, Handbook of Temperature Measurement, Springer, 1998.

80. J.C. Bass, and R.L. Farley, Examples of power from waste heat for gas fields, *Thermoelectrics, 1997. Proceedings ICT '97. XVI International Conference on*, 1997, p. 547-550.

81. A. Tsuyoshi, S. Kagawa, M. Sakamoto, and K. Matsuura, A study of commercial thermoelectric generation in a processing plant of combustible solid waste, *Thermoelectrics, 1997. Proceedings ICT '97. XVI International Conference on*, 1997, p. 555-558.

82. M. Tewolde, C.C. Lin, H. Tao, H. Chen, G. Fu, D. Liu, T. Zhang, D. Benjamin, L. Zuo, D. Hwang, and J. Longtin, Sensors for Small Modular Reactors Powered by Thermoelectric Generators, *ASME 2014 Small Modular Reactors Symposium.* , American Society of Mechanical Engineers, 2014.

83. D. Kraemer, K. McEnaney, M. Chiesa, and G. Chen, Modeling and optimization of solar thermoelectric generators for terrestrial applications, *Solar Energy*, 2012, **86**(5), p. 1338-1350

84. L. Pawlowski, The Science and Engineering of Thermal Spray Coatings, John Wiley & Sons, 2008.

85. I. Gibson, D.W. Rosen, and B. Stucker, Additive Manufacturing Technologies, *Rapid Prototyping to Direct Digital Manufacturing*, Springer, 2010.

86. T. Nakamura, G. Qian, and C.C. Berndt, Effects of Pores on Mechanical Properties of Plasma-Sprayed Ceramic Coatings, *Journal of the American Ceramic Society*, 2000, **83**(3), p. 578-584

87. Z. Wang, A. Kulkarni, S. Deshpande, T. Nakamura, and H. Herman, Effects of pores and interfaces on effective properties of plasma sprayed zirconia coatings, *Acta Materialia*, 2003, **51**(18), p. 5319-5334

88. Y. Tan, J.P. Longtin, and S. Sampath, Modeling thermal conductivity of thermal spray coatings: comparing predictions to experiments, *Journal of Thermal Spray Technology*, 2006, **15**(4), p. 545-552, in English

89. J.P. Longtin, E. Mari, Y. Tan, and S. Sampath, Using Thermal Spray and Laser Micromachining to Fabricate Sensors, *Journal of Thermal Spray Technology*, 2011, **20**(4), p. 958-966, in English

90. V. Goodship, and D. Jacobs, Polyvinyl alcohol: materials, processing and applications, Smithers Rapra Technology, 2009.

91. D. Dornfeld, S. Min, and Y. Takeuchi, Recent Advances in Mechanical Micromachining, *CIRP Annals - Manufacturing Technology*, 2006, **55**(2), p. 745-768

92. M.A. McGuire, A.-S. Malik, and F.J. DiSalvo, Effects of high-pressure high-temperature treatment on the thermoelectric properties of PbTe, *Journal of Alloys and Compounds*, 2008, **460**(1–2), p. 8-12

93. D.E. Wesolowski, R.S. Goeke, A.M. Morales, S.H. Goods, P.A. Sharma, M.P. Saavedra, K.R. Reyes-Gil, W.C.G. Neel, N.Y.C. Yang, and C.A. Apblett, Development of a Bi2Te3-based thermoelectric generator with high-aspect ratio, free-standing legs, *Journal of Materials Research*, 2012, **27**(08), p. 1149-1156

94. V.K. Jain, Advanced Machining Processes, Allied Publishers PVT Limited, 2004.

95. N. Keawprak, Z.M. Sun, H. Hashimoto, and M.W. Barsoum, Effect of sintering temperature on the thermoelectric properties of pulse discharge sintered (Bi0.24Sb0.76)2Te3 alloy, *Journal of Alloys and Compounds*, 2005, **397**(1–2), p. 236-244

96. M.-Z. Yang, C.-C. Wu, C.-L. Dai, and W.-J. Tsai, Energy Harvesting Thermoelectric Generators Manufactured Using the Complementary Metal Oxide Semiconductor Process, *Sensors (Basel, Switzerland)*, 2013, **13**(2), p. 2359-2367

97. Q. Wenmin, P. Matthias, and F. Wolf-Joachim, Microfabrication of thermoelectric generators on flexible foil substrates as a power source for autonomous microsystems, *Journal of Micromechanics and Microengineering*, 2001, **11**(2), p. 146

98. J.F. Ready, LIA Handbook of Laser Materials Processing, Laser Institute of America, 2001.

99. M.C. Gower, Industrial applications of laser micromachining, *Opt. Express*, 2000, **7**(2), p. 56-67

100. D. Diego-Vallejo, D. Ashkenasi, G. Illing, and H.J. Eichler, Plasma Monitoring during Laser Material Processing, *Physics Procedia*, 2011, **12, Part B**(0), p. 404-410

101. A.E. Siegman, Lasers, A. Kelly Ed., University Science Books, 1986.

102. A.H. Firester, M.E. Heller, and P. Sheng, Knife-edge scanning measurements of subwavelength focused light beams, *Appl. Opt.*, 1977, **16**(7), p. 1971-1974

103. J.M. Liu, Simple technique for measurements of pulsed Gaussian-beam spot sizes, *Opt. Lett.*, 1982, **7**(5), p. 196-198

104. D. Bäuerle, Laser Processing and Chemistry, Springer Berlin Heidelberg, 2011.

105. C.P. Grigoropoulos, Transport in Laser Microfabrication - Fundamentals and Applications, Cambridge University Press, 2009.

106. W. Steen, and J. Mazumder, Laser Material Processing, *Production & Process Engineering*, 4th ed. ed., Springer, 2010.

107. P.W. Milonni, and J.H. Eberly, Propagation of Laser Radiation, *Laser Physics*, John Wiley & Sons, Inc., 2010, p. 331-400.

108. M. Fox, Optical Properties of Solids, Oxford University Press, 2001.

109. O. Benavides, O. Lebedeva, and V. Golikov, Reflection of nanosecond Nd:YAG laser pulses in ablation of metals, *Opt. Express*, 2011, **19**(22), p. 21842-21848, in English

110. D. Marla, U.V. Bhandarkar, and S.S. Joshi, Models for predicting temperature dependence of material properties of aluminum, *J. Phys. D-Appl. Phys.*, 2014, **47**(10), p. 12, in English

111. A. Bogaerts, Z. Chen, R. Gijbels, and A. Vertes, Laser ablation for analytical sampling: what can we learn from modeling? , *Spectrochimica Acta Part B*, 2003, **58**(p. 1867–1893

112. G.R. Gathers, Thermophysical properties of liquid copper and aluminum, *Int J Thermophys*, 1983, **4**(3), p. 209-226, in English

113. J. Jandeleit, G. Urbasch, H.D. Hoffmann, H.G. Treusch, and E.W. Kreutz, Picosecond laser ablation of thin copper films, *Appl. Phys. A*, 1996, **63**(2), p. 117-121, in English

114. S. Nolte, C. Momma, H. Jacobs, A. Tünnermann, B.N. Chichkov, B. Wellegehausen, and H. Welling, Ablation of metals by ultrashort laser pulses, *J. Opt. Soc. Am. B*, 1997, **14**(10), p. 2716-2722

115. Y. Jee, M.F. Becker, and R.M. Walser, Laser-induced damage on single-crystal metal surfaces, *J. Opt. Soc. Am. B*, 1988, **5**(3), p. 648-659

116. M. Aghaei, S. Mehrabian, and S.H. Tavassoli, Simulation of nanosecond pulsed laser ablation of copper samples: A focus on laser induced plasma radiation, *Journal of Applied Physics*, 2008, **104**(5), p. 053303-053309

117. A. Bogaerts, Z. Chen, and D. Bleiner, Laser ablation of copper in different background gases: comparative study by numerical modeling and experiments, *Journal of Analytical Atomic Spectrometry*, 2006, **21**(4), p. 384-395

118. A. Bogaerts, and Z. Chen, Nanosecond laser ablation of Cu: modeling of the expansion in He background gas, and comparison with expansion in vacuum, *Journal of Analytical Atomic Spectrometry*, 2004, **19**(9), p. 1169-1176

119. R.S. Figliola, and D.E. Beasley, Theory and Design for Mechanical Measurements, 5th ed., John Wiley & Sons, Inc., 2015.

120. T. Clyne, and S. Gill, Residual Stresses in Thermal Spray Coatings and Their Effect on Interfacial Adhesion: A Review of Recent Work, *Journal of Thermal Spray Technology*, 1996, **5**(4), p. 401-418

121. J. Yang, and F. Stabler, Automotive Applications of Thermoelectric Materials, *Journal of Electronic Materials*, 2009, **38**(7), p. 1245-1251

122. J.R. Davis, ASM Specialty Handbook - Copper and Copper Alloys, ASM International, 2001.

123. R. Brandt, L. Pawlowski, G. Neuer, and P. Fauchais, Specific heat and thermal conductivity of plasma stabilized yttria-stabilized zirconia and NiAl, NiCrAl, NiCrAlY, NiCoCrAlY coatings, *High Temp. High Press*, 1986, **18**(65–67)

124. S. Sampath, Thermal Spray Applications in Electronics and Sensors: Past, Present, and Future, *Journal of Thermal Spray Technology*, 2010, **19**(5), p. 921-949

125. G. Rajesh, and L.M. Kashmiri, Electrically Conductive Adhesives, IDC Publishers, 2008.

126. L. Daoqiang, and C.P. Wong, A study of contact resistance of conductive adhesives based on anhydride-cured epoxy systems, *Components and Packaging Technologies, IEEE Transactions on*, 2000, **23**(3), p. 440-446

127. S. Farhad, D.C. Whalley, and P.P. Conway, Thermal Interface Materials - A Review of the State of the Art, *Electronics Systemintegration Technology Conference, 2006. 1st*, 2006, p. 1292-1302.

128. R. Prasher, Thermal Interface Materials: Historical Perspective, Status, and Future Directions, *Proceedings of the IEEE*, 2006, **94**(8), p. 1571-1586

129. J.-P. Pascault, and R.J.J. Williams, Thermosetting Polymers, *Handbook of Polymer Synthesis, Characterization, and Processing*, John Wiley & Sons, Inc., 2013, p. 519-533.

130. F. Lianhua, S. Bin, J. Qu, and C.P. Wong, Effects of nano-sized particles on electrical and thermal conductivities of polymer composites, *Advanced Packaging Materials: Processes, Properties and Interfaces, 2004. Proceedings. 9th International Symposium on*, 2004, p. 193-199.

131. Y. Li, and C.P. Wong, Recent advances of conductive adhesives as a lead-free alternative in electronic packaging: Materials, processing, reliability and applications, *Materials Science and Engineering: R: Reports*, 2006, **51**(1–3), p. 1-35

132. D. Madan, A. Chen, P. Wright, and J. Evans, Printed Se-Doped MA n-Type Bi2Te3 Thick-Film Thermoelectric Generators, *Journal of Electronic Materials*, 2012, **41**(6), p. 1481-1486, in English

133. M. Wang, and N. Pan, Predictions of effective physical properties of complex multiphase materials, *Materials Science and Engineering: R: Reports*, 2008, **63**(1), p. 1-30

134. T.K. Xia, and X.C. Zeng, The effective-medium approximation for the thermoelectric power of polycrystals: application to a model for La 2-x M x CuO 4, *Journal of Physics C: Solid State Physics*, 1987, **20**(32), p. L907

135. K.-H. Lee, H.-S. Kim, S.-I. Kim, E.-S. Lee, S.-M. Lee, J.-S. Rhyee, J.-Y. Jung, I.-H. Kim, Y. Wang, and K. Koumoto, Enhancement of Thermoelectric Figure of Merit for $Bi_{0.5}Sb_{1.5}Te_3$ by Metal Nanoparticle Decoration, *Journal of Electronic Materials*, 2012, **41**(6), p. 1165-1169, in English

136. D. Lu, and C.P. Wong, Effects of shrinkage on conductivity of isotropic conductive adhesives, *International Journal of Adhesion and Adhesives*, 2000, **20**(3), p. 189-193

137. Z. Michael, E. Oleg, S. Amir, and K. Zvi, Laser sintering of copper nanoparticles, *Journal of Physics D: Applied Physics*, 2014, **47**(2), p. 025501

138. J. Yu, K.-T. Kang, J. Hwang, S.-H. Lee, and H. Kang, Rapid sintering of copper nano ink using a laser in air, *Int. J. Precis. Eng. Manuf.*, 2014, **15**(6), p. 1051-1054, in English

139. International Energy Agency, World Energy Outlook 2015.

140. US Nuclear Regulatory Commission, Reactor safety study: An assessment of accident risks in US commercial nuclear power plants.

141. E. S.A., C.D. Gentillon, T.E. Wierman, and D.M. Rasmuson, Reevaluation of Station Blackout Risk at Nuclear Power Plants – Analysis of Station Blackout Risk, Idaho National Laboratory.

142. P.W. Baranowsky, Evaluation of Station Blackout Accidents at Nuclear Power Plants, U.S. Nuclear Regulatory Commission

143. D.T. Ingersoll, Deliberately small reactors and the second nuclear era, *Progress in Nuclear Energy*, 2009, **51**(4–5), p. 589-603

144. V. Kustenov, Current Status, Technical Feasibility and Economics of Small Nuclear Reactors *Nuclear Development*, Nuclear Energy Agency (NEA), 2011, p. 177.

145. N.A, Status of Small and Medium Sized Reactor Designs, *Advanced Reactors Information System (ARIS)*, International Atomic Energy Agency (IAEA), 2012.

146. IAEA, Advanced Reactor Information System (ARIS) International Atomic Energy Agency, 2013.

147. S.-H.K. Kim, Keung Koo; Yeo, Ji Won; Chang, Moon Hee; Zee, Sung Quun, Design verification program of SMART, *International conference on global environment and advanced nuclear power plants*, 2003.

148. J. Vujić, R.M. Bergmann, R. Škoda, and M. Miletić, Small modular reactors: Simpler, safer, cheaper? , *Energy*, 2012, **45**(1), p. 288-295

149. H. Spieler, Introduction to radiation-resistant semiconductor devices and circuits, *AIP Conference Proceeding*, A. Lumpkin and C.E. Eyeberger Eds., 1997, p. 23-49.

150. S.F. Tie, and C.W. Tan, A review of energy sources and energy management system in electric vehicles, *Renewable and Sustainable Energy Reviews*, 2013, **20**(0), p. 82-102

151. D.A. Wright, Thermoelectric Properties of Bismuth Telluride and its Alloys, *Nature*, 1958, **181**(4612), p. 834-834

152. T. Hendricks, N. Karri, T. Hogan, and C. Cauchy, New Perspectives in Thermoelectric Energy Recovery System Design Optimization, *Journal of Electronic Materials*, 2013, **42**(7), p. 1725-1736, in English

153. N. Hiller, Quick attaching thermoelectric device, USPTO Ed., 2005, p. 4.

Appendix A

Thermoelectric Material Testing and Characterization Tools

A.1 Seebeck Coefficient

The temperature-dependent Seebeck measurements were made over a temperature range from 70 K to 730 K. The system includes two pairs of thermocouples – one pair is formed of junctions of copper and a reference material with known Seebeck coefficient and the other pair is formed of junctions of copper and the material whose Seebeck coefficient is to be determined.

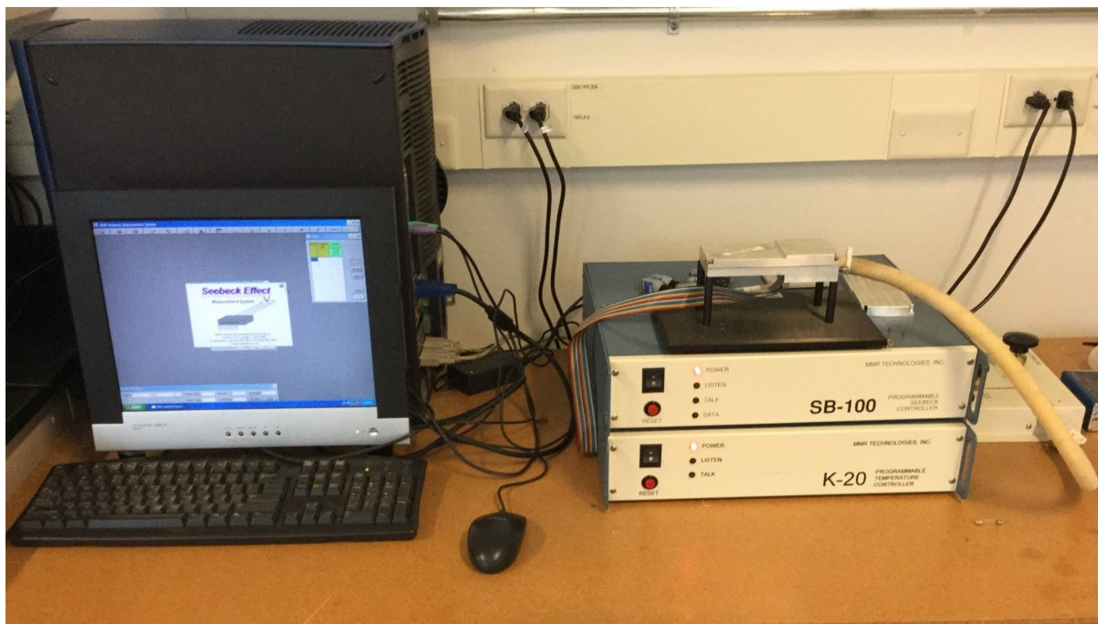

MMR's Seebeck Measurement System

System Specifications

- Maximum Operating Temperature: 70K to 730K
- Stand-alone Seebeck Experiments at ambient temperature
- Power available to heat the sample: 0.1 mW - 1 Watt

Sample Requirements

- Simple sample mounting permitting rapid interchange of samples.
- Sample Length: >2 mm and <10 mm
- Sample Width: >1.5 mm

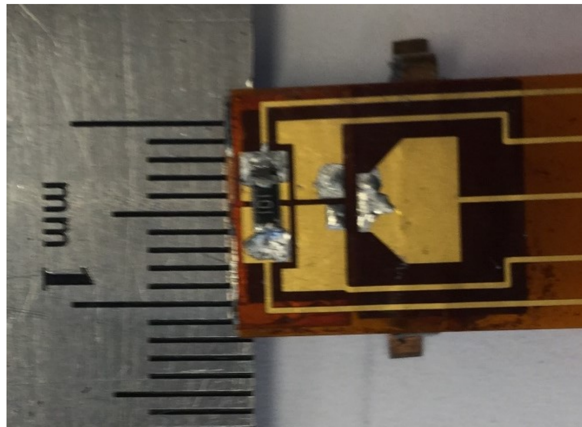

Sample Mounting & Size Requirements

A.2 Thermal Properties

The thermal conductivity measurements were made with a LFTD machine, which can measure values up to 1200°C with the flash method. It also allows for the measurement of specific heat capacity and thermal conductivity of materials with a wide range of thermal properties.

TA Instrument’s Flash Diffusivity Measurement System and Sample Mount

Sample Requirements

- Includes multiple specimen testing (up to 4 specimens)
- Sample Diameter: 12.7 mm [0.5 in]
- Sample Thickness: > 0.1 mm

A.3 Electrical Properties

The electrical resistivity is measured using an RM3000 four-point probe measurement system from Jandel Engineering. The units are combined constant current sources with inbuilt digital voltmeters so only a single unit is required to make four point probe measurements.

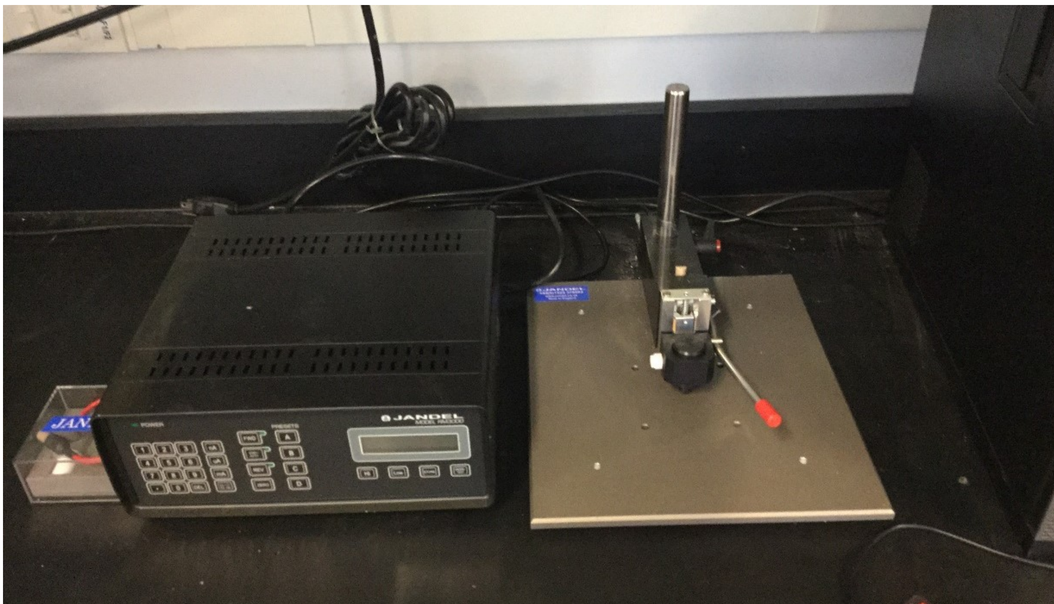

Jandel's Four Point Probe Resistivity Measurements System

Sample Requirements

- Probe spacing: 1.591mm (needle to needle)
- Sample Length: > 8 mm
- Sample Width: > 2 mm